Ferroelectric Materials with Interfaces: First Principles Calculations

Von der Fakultät für Mathematik, Informatik und Naturwissenschaften der RWTH Aachen University zur Erlangung des akademischen Grades eines Doktors der Naturwissenschaften genehmigte Dissertation

vorgelegt von

Master of Science

Kourosh Rahmanizadeh
aus Ahvaz (Iran)

Berichter: Universitätsprofessor Dr. Stefan Blügel
Universitätsprofessor Dr. Uwe Klemradt

Tag der mündlichen Prüfung: 02.02.2011

Abstract

Ferroelectric Materials with Interfaces: First Principles Calculations

Ferroelectric materials are characterized by a reversible spontaneous electric polarization in the absence of an electric field. This polarization arises from a non-centrosymmetric arrangement of the ions in the unit cell that produces an electric dipole moment. Ferroelectric materials have been extensively studied in recent years because of their promising properties for a wide range of applications, ranging from three-dimensional trenched capacitors for dynamic random access memories and ultrafast switching to cheap room-temperature magnetic-field detectors, piezoelectric nanotubes for microfluidic systems and electrocaloric coolers for computers.

Experimental studies have shown that defects, stacking faults and domain boundaries play an important role in ferroelectric materials. In this thesis the polarization of thin films of the perovskite $A\mathrm{TiO}_3$ compounds PbTiO_3 and BaTiO_3 is investigated. The investigations take advantage of the density functional theory (DFT), a modern theory which permits the treatment of the many electrons problem in real solids. The actual calculations are carried out with the full-potential linearized augmented planewave method (FLAPW) method as implemented in the Jülich DFT code (FLEUR). The applicability of different exchange-correlation potentials is studied. Both AO-terminated and TiO_2-terminated surfaces with the polarization in the film plane and perpendicular to the surface are considered. The influence of the surface and stacking faults on the polarization near to the surface have been studied. Without an electric field that compensates the depolarization field a polarization perpendicular to the surface is not stable, but I can stabilize an out-of-plane polarization with different types of defects at the surface.

Two different types of domain walls, transversal and longitudinal, in PbTiO_3 are considered. I simulated [110]-oriented 180° transversal domain boundaries and [100]-oriented 180° longitudinal domain walls. The latter type of walls is not stable in a stoichiometric material. When such domain walls with bulk polarization are formed, the electric charges accumulated at the interface make the domain walls metallic and unfavorable due to electrostatic energy. I stabilized the longitudinal domain walls by creating defects on the interface. The lateral extension of these domain walls is studied and compared to experimental results.

Contents

1 Introduction

Crystal structures can be divided into 32 classes, or point groups, according to the number of rotational axes and reflection planes that leave the crystal structure unchanged. Twenty-one of the 32 crystal classes lack a center of inversion symmetry, and of 20 these are piezoelectric. Of these 20 piezoelectric crystal classes, 10 are pyroelectric (polar). Ferroelectrics are pyroelectrics that possess a spontaneous polarization, which can be reversed by applying a suitable electric field. The process is known as switching and is accompanied by a hysteresis in the field versus polarization curve. The value of the spontaneous polarization is easily determined from the switching loop. In recent years, ferroelectric materials with the perovskite structure ABO_3 (A, B=cations) have attracted attention owing to their prospective technological applications, e.g. non-volatile and high-density memories, thin-film capacitors and pyroelectric devices. As these applications are realized in complex components or thin-film geometries, whose size is now reaching extremely small dimensions down to several nanometers, knowledge of the bulk-properties alone is no longer sufficient. Structures are studied, where the effect of surface, interfaces, staking faults and domain boundaries can be critical.

1.1 History of the ferroelectricity

Pyroelectricity has been know since ancient time because of the ability of these materials to attract objects when they are heated. During the eighteenth century, many experiments where carried out in an attempt to characterize the pyroelectric effect in a quantitative manner for instance by Gaugain [1] in 1856.

As is well known, the word “ferroelectric” (more exactly, “ferroelektrisch”) was invented by Schrödinger in 1912 in a paper, in which he discussed the possibility for the dielectric instability to occur and found that a phenomenon similar to ferromagnetism could occur under some circumstances [2, 3]. The ferroelectric effect was first observed by Valasek [4] in 1920, in the Rochelle salt, with molecular formula $KNaC_4H_4O_6{\cdot}4H_2O$, who observed that the polarization of $KNaC_4H_4O_6{\cdot}4H_2O$ can be reversed by the application of an external field. In 1935, the second ferroelectric material potassium di-hydrogen phosphate KH_2PO_4 was discovered [5].

From 1920 until about 1943, ferroelectrics were academic curiosities, of little application or theoretical interest, mostly water-soluble and fragile. They were all hydrogen bonded and this property was thought to be essential for ferroelectricity. During the war years, this changed upon the discovery of the ferroelectric properties of

barium titanate ($BaTiO_3$), that were found incidentally, when searching for new dielectric to replace mica [6, 7]. Rapidly, it became by far the most extensively studied ferroelectric material. Also an "electronic ceramics" industry was established. Upon on cooling, $BaTiO_3$ undergoes a sequence of three successive structural transitions from a paraelectric cubic phase to ferroelectric structures of tetragonal, orthorhombic and rhombohedral symmetry. It was the first ferroelectric without hydrogen bonds, the first with a non-polar paraelectric phase, the first with more than one ferroelectric state. In addition, its prototype crystal structure is a cubic perovskite with only five atoms per unit cell. It was, therefore, offering physicists an opportunity to study the onset of ferroelectricity from a very simple structure.

The sudden interest for $BaTiO_3$ broadened gradually to different oxides of the ABO_3 family. A ferroelectric activity was discovered in $KNbO_3$ presenting the same sequence of phase transitions than $BaTiO_3$ [8], or $PbTiO_3$ that remains stable at low temperature in tetragonal symmetry. Also simultaneously, antiferroelectricity was discovered in $PbZrO_3$ [9], which shifted attention to the theoretical description of ferroelectric and antiferroelectric phenomena in a manner much more amenable to a microscopic investigation.

Mason and Matthias (1950) proposed a simple microscopic model to describe the ferroelectricity in $BaTiO_3$, in which the small Ti^{4+} ion, surrounded by six oxygen ions, is depicted as being in an off-center sixfold potential-well minimum, giving rise to a unit dipole. It is capable of undergoing order-disorder transitions under the influence of both thermal energy and the electrostatic energy of the effective local field in which the cooperative influence of all other neighboring unit dipoles predominates. This model was then strongly criticized by Jaynes [10], using arguments apparently plausible but, not too well founded and it was used latter as starting point for improved statistical models. Independently, in 1950 Slater [11] pointed out that the ferroelectric behavior of $BaTiO_3$ could be caused by long-range dipolar forces (via the Lorentz local effective field) competing with local short-range forces. Later, this provided the basic framework to describe the phase transition in displacive type ferroelectrics. Mueller(1940) [12–14], and later Ginzburg (1945,1949) [15,16] and Devonshire (1949, 1951, 1954) [17–19] were the first to propose macroscopic, thermodynamical theories of ferroelectricity. Devonshire's theory [20], which described in detail the successive phase transitions in $BaTiO_3$, (from cubic to tetragonal, from tetragonal to orthorhombic and from orthorhombic to rhombohedral) became the paradigm of a phenomenological theory for ferroelectricity, and has remained so through several decades. In 1960 Anderson and Cochran [21] recasted the microscopic theory in terms of crystal lattice dynamics, and predicted successfully the existence of "soft-modes", later observed by neutron, infrared and Raman scattering.

Before 1970, the most exciting challenge in ferroelectrics was modeling ferroelectric phase transitions and discovering new ones. There are now 700 ferroelectric materials, many of which are neither hydrogen bonded nor oxides, such as GeTe, $SrAlF_5$, or SbSi. These are very successful used for actuators and piezoelectric transducers as well as for pyroelectric detectors. The application for sound navigating sonars was

particularly well funded. The focus changed after 1984, when thin-film ferroelectrics were developed and for the first time integrated into semiconductor chips [22]. In 1994, a ferroelectric bypass capacitor for 2.3-GHz operation in mobile digital telephones won the Japan Electronic Industry "Product of the Year" award, with 6 million chips per month in production. The polarization of a typical ferroelectric is reversed at a critical "coercive" field E $\approx$ 50 kV/cm. In a 1-mm bulk device, this is a 5-kV voltage unsuitable for a mobile telephone; however, for submicrometer films it is less than 5 V, permitting integration into most silicon chips. It is in the form of "integrated ferroelectrics" that the renaissance of ferromaterials occurred.

Nowadays, there are several directions for ferroelectrics research: substrate-film interfaces and high-strain states, finite size effects, nanotubes and nanowires, electrocaloric devices, ferroelectric random access memories (FeRAMs), dynamic random access memory (DRAM) capacitors, electron emitters, weak-magnetic field sensors, magnetoelectrics, and self-assembly. Ferroelectric liquid crystals (smectic thin films) probably have a more mature commercial product line as spatial light modulators and video camera view-finders [23].

1.2 A first-principles approach

The first-principles density-functional-theory (DFT) is a powerful method for addressing many questions concerning the ferroelectric material e.g. origin of ferroelectricity in perovskite oxides. Earliest DFT calculations on ABO_3 compounds were reported by Weyrich [24] during the eighties. In 1992, Cohen calculated the ground-state structures and electronic-structure of $BaTiO_3$ and $PbTiO_3$ [25], and later extended the investigations to many other ferroelectric perovskites [26].

The modern theory of polarization proposed by Resta [27], King-Smith and Vanderbilt [28, 29] was an important step in order to obtain a correct definition of the bulk electric polarization. Without this theory, the macroscopic electronic polarization was not indeed uniquely determined and not accessible by electronics structure methods which make use of infinite periodic systems with continuous electronic distributions. Now, the electronic contribution to the polarization can be conveniently obtained from a Berry phase of the electronic wavefunctions and is easily computed in the framework of DFT.

As computational power and algorithmic efficiency have improved, it has become possible to study increasingly complex systems, such as surfaces [30–35] , interfaces [36–38], defects [39,40], domain walls [41,42], superlattices [43,44] and nanostructures [45–48].

1.3 The present work

In this work, we studied the ferroelectric behavior of the prototypical ferroelectric materials $BaTiO_3$ and $PbTiO_3$. Experimental studies have shown that the performance

of ferroelectric devices depends strongly on the non-perfect environment encountered in real device structures. In this thesis I address the question how surfaces, domain boundaries, defects and stacking faults change the ferroelectric behavior.

Chapter 2 gives a quick overview to the Kohn-Sham ansatz outlining the general aspects of the density functional theory (DFT) methodology. The full-potential linearized augmented planewave (FLAPW) method is discussed in detail in chapter 3. The implementation of FLAPW method for a film with and without an external electric field is considered.

In ferroelectric materials, the ferroelectric behavior strongly depends on the lattice parameters (e.g. volume and tetragonalty, i.e. c/a-ratio). Thereby, the calculated lattice parameters depend on the choice of the exchange-correlation functional approximation the unknown energy functional of the DFT. An exchange-correlation functional should be chosen where the calculated lattice parameters are close to the experimental results. To this end, the lattice parameters have been calculated with different types of exchange-correlation functionals, summarized in chapter 4. The different ferroelectric behaviors of $BaTiO_3$ and $PbTiO_3$ are explained on the basis of the partial densities of states (PDOS) for $BaTiO_3$ and $PbTiO_3$. The influence of surface and stacking faults on the polarization parallel to the surface plane in the $BaTiO_3$ and $PbTiO_3$ have been studied.

In chapter 5 we considered a polarization perpendicular to the surface plane, the so-called out-of-plane polarization. Understanding the mechanism of stabilization of the out-of-plane polarization is very important for ferroelectric thin films. There are several experimental studies about a stabilized out-of-plane polarization on thin ferroelectric thin films, e.g. out-of-plane polarization which has been stabilized for $BaTiO_3$ nanostructures by molecular hydroxyl (OH) and carboxylate (R-COO) adsorbates [45]. We have studied how to stabilize out-of-plane polarization by using an external electric field or different types of defects at the $BaTiO_3$ and $PbTiO_3$ surfaces. Electronic structures for an out-of-plane polarization, i.e. outward and inward to the $PbTiO_3$ surfaces, have been calculated.

In chapter 6 we studied different types of domain walls, i.e. transversal (TDW) and longitudinal (LDW) in $PbTiO_3$. The longitudinal domain walls are not stable in a stoichiometric material. When such domain walls are formed, the electric charges accumulated at the interface make domain walls metallic and unfavorable due to electrostatic energy. The longitudinal domain walls are stabilized by creating defects at the domain walls in $PbTiO_3$. We compared our TDW and LDW results to the experimental results of C. Jia et al. [49]. Finally, we summarize the main results obtained with in this work.

2 Density functional theory

For calculating physical properties of solids, it is very importance to find a good quantum-mechanical model to simulating these systems. However, the atom nuclei and the electrons constitute a complex manybody problem. A simplification of this problem can be achieved by employing the Born-Oppenheimer-approximation, within which the motion of the nuclei is separated from the motion of the electrons. In any instant, the atomic nuclei can then be considered as point charges at fixed positions. Thus, all quantum effects of the motion of the nuclei are neglected. This approximation, which is made in vast majority of first-principle calculation, leads to the following Schrödinger equation.

$$\begin{aligned} \mathcal{H}\mathbf{\Psi} &= \left\{ -\sum_{i=1}^{N} \frac{\hbar^2}{2m}\nabla^2 + \sum_{\substack{i,j=1 \\ i\neq j}}^{N} \frac{e^2}{|\mathbf{r}_i - \mathbf{r}_j|} - \sum_{i=1}^{N}\sum_{\mu=1}^{M} \frac{e^2 Z^\mu}{|\mathbf{r}_i - \mathbf{R}^\mu|} \right\} \mathbf{\Psi}(\mathbf{r}_1, ..., \mathbf{r}_N) \\ &= \mathcal{E}\mathbf{\Psi}(\mathbf{r}_1, ..., \mathbf{r}_N) \ , \end{aligned} \tag{2.1}$$

where Z^μ and $\mathbf{R}^\mu$ are atomic numbers and positions of atomic nuclei μ, m and $\mathbf{r_i}$ are the absolute mass and positions of electrons.

However, due to large dimension of $\mathbf{\Psi}$ and the requirement of antisymmetry, which means that $\mathbf{\Psi}$ has to be expanded into sum of Slater determinants rather than simple product-functions, this equation can be solved only for tiny systems, including few electrons. In order to deal with realistic materials, relevant in solid state physics, further approximations have to be made.

A breakthrough in the parameter-free ab-initio description of complex electronic systems has been achieved with the development of density functional theory by Hohenberg and Konh [50] and Kohn and Sham [51]

2.1 The theorem of Hohenberg and Kohn

The all-electron wavefunction contains all information available about an electronic system. However, not the whole information is needed to determine the ground state properties of a physical system. The measurable quantities are given by expectation values of quantum-mechanical operators corresponding to the observable under consideration. The central idea of the density functional theory [52] is to replace the complex many particle wavefunction by a far simpler quantity, the electron density, given by

$$\rho(\mathbf{r}) = \langle \mathbf{\Psi} | \sum_{i=1}^{N} \delta(\mathbf{r} - \mathbf{r}_i) | \mathbf{\Psi} \rangle \ . \tag{2.2}$$

Hohenberg and Kohn were able to show for systems with a non-degenerate ground state, that:

- For a given external potential V_{ext}, the ground state energy and all other ground state properties of the system are unique functionals of the electron density $\rho(\mathbf{r})$.
- The energy functional is variational, i.e. the ground state density $\rho_0(\mathbf{r})$ minimizes the energy functional $E[\rho]$, under the subsidiary condition that the number of electrons is kept constant.

$$E[\rho] > E[\rho_0] = E_0 \qquad \text{for all} \qquad \rho(\mathbf{r}) \neq \rho_0(\mathbf{r}). \tag{2.3}$$

The density functional formalism can be extended to degenerate ground states [53]. The second part of the theorem implies, that the ground state density can obtained form the minimization of the energy functional:

$$\delta E[\rho] = 0. \tag{2.4}$$

Levy [54] provided a simpler and more general derivation of the above theorems, defining the energy functional by

$$E[\rho] = min \langle \mathbf{\Psi} | \mathcal{H} | \mathbf{\Psi} \rangle. \tag{2.5}$$

However, no explicit representation of $E[\rho]$ has been derived so far.

2.2 The Kohn-Sham equations

An important step on the way to finding an applicable approximation of the energy functional is the idea of Kohn and Sham [51]. The central concept of their theory is to split the energy functional into several terms:

$$E[\rho] = T_{kin}[\rho] + E_H[\rho] + E_{xc}[\rho] + E_{ext}[\rho] \ , \tag{2.6}$$

where T_{kin} is the kinetic energy of non-interacting electrons, E_H is Hartree energy, i.e. the classical Coulomb energy of the electrons, and $E_{xc}[\rho]$ is the exchange-correlation energy which contains terms coming from the Pauli principle (exchange hole), from correlations due to the repulsive Coulombic electron-electron interaction and from the contribution to the kinetic energy of interacting electrons. E.g. In the local density approximation $E_{xc}[\rho]$ is written in the form $E_{xc}[\rho] = \int drn(\mathbf{r}) \varepsilon_{xc}(\rho(\mathbf{r}))$.

Then E_{ext} is the interaction energy of the electrons with the ions, e.g. described by the $1/r$ potential as in all-electron methods or by pseudo-potentials.

An explicit formula for $T_{kin}[\rho]$ can be obtained using a special ansatz for electrons density. The density can written as a sum of single particle wavefunctions, as in the case of non-interacting electrons

$$\rho(\mathbf{r}) = 2\sum_{i=0}^{N} |\psi_i(\mathbf{r})|^2 \,, \tag{2.7}$$

where the sum is over the occupied states and the factor of two accounts for the spin degeneracy. With this ansatz the kinetic energy can be written as:

$$T_{kin}[\rho] = -2\sum_{i=1}^{N} \int \psi_i^*(\mathbf{r}) \frac{\hbar^2}{2m} \nabla^2 \psi_i(\mathbf{r}) d^3r \,. \tag{2.8}$$

Instead of minimizing the energy functional with respect to the electron density, it can also be minimized with respect to the wavefunctions ψ_i (or their complex conjugates). In this case the subsidiary condition of particle conservation is replaced by the requirement of normalized wavefunctions

$$\int |\psi_i(\mathbf{r})|^2 d^3r = 1 \,, \tag{2.9}$$

this requirement is taken into account by Lagrange parameters ε_i. Applying the variational principle yields the Kohn-sham equation

$$\Big\{\frac{\hbar^2}{2m}\nabla^2 + \hat{\mathcal{V}}_{eff}(\mathbf{r})\Big\}\psi_i(\mathbf{r}) = \varepsilon_i \psi_i(\mathbf{r}) \,, \tag{2.10}$$

with

$$\hat{\mathcal{V}}_{eff} = \hat{\mathcal{V}}_{ext} + \hat{\mathcal{V}}_H + \hat{\mathcal{V}}_{xc} \,. \tag{2.11}$$

In the real space representation the individual terms are the following:

$$\text{external-potential :} \qquad \hat{\mathcal{V}}_{ext}(\mathbf{R}, \mathbf{r}) = -\sum_{\mu=1}^{M} \frac{e^2 Z^2}{|\mathbf{r}_i - \mathbf{R}^\mu|} \tag{2.12}$$

$$\text{Hartree potential:} \qquad \nabla^2 \hat{\mathcal{V}}_H(\mathbf{r}) = 4\pi e^2 \rho(\mathbf{r}) \tag{2.13}$$

$$\text{xc-potential(LDA):} \qquad \hat{\mathcal{V}}_{xc}(\mathbf{r}) = \frac{\delta}{\delta\rho(\mathbf{r})} \int dr \rho(\mathbf{r}) \varepsilon_{xc}(\rho(\mathbf{r})) \tag{2.14}$$

The terms $\hat{\mathcal{V}}_H[\rho]$ and $\hat{\mathcal{V}}_{xc}[\rho]$ are local potentials and explicitly density dependent. Thus, the Hamiltonian $\hat{\mathcal{H}}[\rho]$ and wavefunctions $\psi_i([\rho], \mathbf{r})$ are also dependent on the electron density $\rho(\mathbf{r})$. Together with the expression .(4.1) a self -consistency problem to obtain the charge density $\rho(\mathbf{r})$ is established, which is solved iteratively until the input density (used to define the potential term in the Hamiltonian) is equal to the output density within the required accuracy. The external potential $\hat{\mathcal{V}}_{ext}[\mathbf{R}]$ depends

explicitly on the position $\mathbf{R}$ of all atoms, which change at certain steps to optimize the atomic structure or every time-step of a molecular dynamics algorithm. Thus, the Hamiltonian $\hat{\mathcal{H}}[\rho]$ and the wavefunctions $\psi_i([\rho], \mathbf{r})$ are also dependent on the atomic positions $\mathbf{R}$. After the self-consistency condition for the electron density has been fulfilled, the atom positions are moved by a molecular static or molecular dynamics time-step.

3 The FLAPW method

3.1 The FLAPW method

There are many possible ways to solve the Kohn-sham equations. One common method is to use some kind of basis set to represent the the wavefunctions. A suitable choice that is already suggested by Bloch's theorem are plane waves. They have a lot of advantages : They are orthogonal, they are diagonal in momentum and any power of momentum and the implementation of planewave based methods is rather straightforward because of there simplicity. However, since the electron wavefunctions are varying very quickly near the core, large wavevectors are needed to represent the wevefunctions accurately . This makes planewaves very inefficient. To overcome this problem this require to separate valence from core-electrons "freeze" the latter ones. Then you can use a "pseudo"-potential for the valence e^-, that has the correct scattering properties. one can employ pseudopotential techniques, which allow an accurate description of the wevefunctions between the atoms, but avoid the fast oscillations near the core. Another way to solve this problem is to use a basis set, which contains radial wavefunctions to describe the oscillations near the core. This has already been suggested by Slater [55]. The corresponding technique is called the augmented planewave (APW) method .

3.1.1 The APW method

Within the APW approach, space is divided into spheres centered at each atom site, the so-called muffin-tins, and the remaining interstitial region (cf. Fig. 3.1). In the region far away from the nuclei (interstitial region), the electrons are more or less 'free'. Free electrons can be described by plane waves . Close to the nuclei (muffin-tins region), the electrons behave quite as they were in a free atom, and they can be described more efficiently by atomic like functions. A single augmented plane wave (APW) used in the expansion of $\phi_\nu(\mathbf{k},\mathbf{r})$ is defined as:

$$\varphi_{\mathbf{G}}(\mathbf{k},\mathbf{r}) = \begin{cases} e^{i(\mathbf{G}+\mathbf{k})\mathbf{r}} & \text{interstitial region} \\ \sum_{lm} A_L^{\mu\mathbf{G}}(\mathbf{k}) u_l(r) Y_L(\hat{\mathbf{r}}) & \text{muffin-tin } \mu \end{cases} \tag{3.1}$$

where $\mathbf{k}$ is the Bloch vector, $Y_L(\hat{\mathbf{r}})$ is the spherical harmonics, Ω is the unit-cell volume, $\mathbf{G}$ is a reciprocal lattice vector, L abbreviates the quantum numbers l and m and

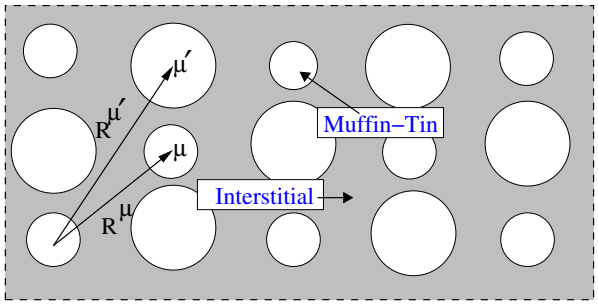

Figure 3.1: Volume of unit cell partitioned into muffin-tin spheres of two different types of atoms and the interstitial region.

u_l is the regular solution of the radial Schrödinger equation

$$\left\{ -\frac{\hbar^2}{2m}\frac{\partial^2}{\partial r^2} + \frac{\hbar^2}{2m}\frac{l(l+1)}{r^2}V(r) - E \right\} r u_l(r) = 0. \tag{3.2}$$

Here E_l is an energy parameter and V(r) is the spherical component of potential $V(\mathbf{r})$. The coefficients $A_L^{\mu\mathbf{G}}(\mathbf{k})$ are determined form the requirement, that the wevefunctions have to be continuous at the boundary of the muffin-tin spheres in order for the kinetic energy to be well-defined.

If the E were kept fixed, used only as parameter during the construction of the basis, the Hamiltonian could be set up in terms of basis. This would lead to a standard secular equation for the band energies. Unfortunately, it turns out, that the APW basis does not offer enough variational freedom if the E is kept fixed. An accurate description can only be achieved if they are set to the corresponding band energies. However, requiring the E's to equal the band energies, the latter can no longer be determined by simple diagonalization of the Hamiltonian matrix. Since the u_l's depend on the band energies, the solution of secular equation becomes a nonlinear problem, which is computationally much more demanding than a secular problem. One way of solving this problem is to fix the energy E and scan over $\mathbf{k}$ to find a solution. i.e. find one band at the time, instead of diagonalization a matrix to find all the bands at a given $\mathbf{k}$. Thus, in Slater's formulation of the method E enters as additional non-linear variational parameter varying the shape of the functions u_l till the optimal shape is found for the band energies one has looked for. Another disadvantage of APW method is, that it is difficult to extend beyond the spherically averaged muffin-tin potential approximation, because in the case of a general potential the optimal choice of E is no longer the band energy. And finally, but less serious, if, for a given choice of E, the radial functions u_l vanish at the muffin-tin radius, The boundary conditions on the spheres cannot be satisfied, i.e. the planewaves and the radial function become decoupled. This called the asymptote problem. It can already cause numerical difficulties

if u_l becomes very small at the sphere boundary. Further information about the APW method can be found in the book by Loucks [56].

3.1.2 The concept of LAPW

The basic idea of the linearized augmented planewave method (LAPW) is to add extra variational freedom to the basis inside the muffin-tins, so that it is not necessary to set the E_l equal to the band energy. This is done by using not only the radial solution of the Schrödinger equation, but also its derivative with respect to the energy. This construction, which was first suggested by O.K. Andersen [57], can be regarded as a linearization of the APW method. To realize this, recall that in the APW method the u_l's depend on the energiesϵ_i and can thus be understood as functions of r and ϵ. Hence, u_l can be expanded into a Taylor-series around a chosen energy E_l

$$u_l(\epsilon, r) = u_l(E_l, r) + \dot{u}_l(E_l, r) + O[(\epsilon - E_l)^2] \; . \tag{3.3}$$

Here $\dot{u}_l$ denote the energy derivative of u_l,$\partial u_l(\epsilon, r)/\partial\epsilon$, and$O[(\epsilon - E_l)^2]$ denotes errors that are quadratic in the energy difference. Ergo, the LAPW method introduces an error of order $(\epsilon - E_l)^2$ in the wavefunction. Therefore, according to the variational principle the error in the calculated band energies is of the order $(\epsilon - E_l)^4$. Because of this high order, the linearization works very well even over rather broad energy regions. In most cases a single set of energy parameters is sufficient for the whole valence band. However, sometimes the energy region has to be split up in two (very rarely more) windows with separate sets of energy parameters. But let's turn to some important properties of the LAPW basis first, before discussing its quality and accuracy. The LAPW basis functions are of the form

$$\varphi_{\mathbf{G}}(\mathbf{k}, \mathbf{r}) = \begin{cases} e^{i(\mathbf{G}+\mathbf{k})\mathbf{r}} & \text{interstitial region} \\ \displaystyle\sum_L A_L^{\mu\mathbf{G}}(\mathbf{k}) u_l(r) Y_L(\hat{\mathbf{r}}) + B_L^{\mu\mathbf{G}}(\mathbf{k}) \dot{u}_l(r) Y_L(\hat{\mathbf{r}}) & \text{muffin-tin } \mu \; , \end{cases} \tag{3.4}$$

with the extra term $B_L^{\mu\mathbf{G}}(\mathbf{k})\dot{u}_l(r)Y_L(\hat{\mathbf{r}})$ compared to the APW method. The additional coefficient is determined by requiring that not only the basis functions, but also their derivatives with respect to r are continuous at the sphere boundaries. This makes the evolution of $\hat{T}_o$ simpler as compared to the APW method. It is useful to require the following normalization.

$$\langle u|u\rangle = \int_0^{R_{MT}} u_l^2(r) r^2 dr = 1 \; . \tag{3.5}$$

Here R_{MT} is the muffin-tin radius. Taking the derivative of (3.5)with respect to the energy it can easily be shown, that u_l and $\dot{u}_l$ are orthogonal. $\dot{u}_l$ is calculated from a

Schrödinger-like equation, derived by taking the energy derivative of(3.2).

$$\left\{ -\frac{\hbar^2}{2m}\frac{\partial^2}{\partial r^2} + \frac{\hbar^2}{2m}\frac{l(l+1)}{r^2}V(r) - E_l \right\} r\dot{u}_l(r) = r u_l(r) \ . \tag{3.6}$$

Still the solution of this equation has to be made orthogonal to u_l, since any linear combination of u_l and $\dot{u}_l$ also solves the equation. Once u_l and $\dot{u}_l$ are made orthogonal the basis function inside the spheres form a completely orthogonal basis set , since the angular functions $Y_{lm}(\hat{\mathbf{r}})$ are also orthogonal. However, the LAPW function are in general not orthogonal to the core states, which are treated separately in the LAPW method. This fact can cause problems in the presence of high lying core states . A detailed discussion of these problems and strategies to circumvent them can be found in the book by Singh [58], which includes a very comprehensive review of many aspects of the LAPW method.

With the construction of the LAPW basis the main problems of the APW method are solved :

- Since it is no longer necessary to set the energy parameters equal the band energies, the latter can be determined by a single diagonalization of the Hamiltonian matrix.
- The LAPW method can be extended to nonspherical muffin tin potentials with little difficulty, because the basis offers enough variational freedom. This leads then to the full-potential linearized augmented plane wave method (FLAPW).
- If u_l is zero at the sphere boundary, its radial derivative u' and $\dot{u}_l$ are in general nonzero. Hence, the boundary conditions can always be satisfied and there is no asymptote problem.

As a final remark it is worth mentioning, that the nonlinearity inherent to the APW method can only be circumvented at the expense of a larger eigenvalue problem. To see this recall that within LAPW (and also within APW) the basis functions are represented by planewaves. The function inside the muffin-tin are coupled to the planewaves via the boundary conditions, and can only be varied indirectly by variation of the planewave coefficients. Clearly, with a finite number of planewaves, at maximum the same number of functions inside the spheres can be varied independently. Hence, to make use of the of the extra variation freedom, that the LAPW basis set allows as compered to the APW basis, i.e. to vary u_l's and the $\dot{u}_l$'s independently, more planewaves have to be used.

3.1.3 The concept of FLAPW

The majority of applications of APW and LAPW method employed shape-approximations on the potential used in the Hamiltonian. Typically, the potential in the unit cell, $V(\mathbf{r})$, is approximated by $V_0(\mathbf{r})$

$$V_0(\mathbf{r}) = \begin{cases} V_0^I = const. & \text{interstitial region} \\ V_0^{MT}(r) & \text{muffin-tin } \mu\ , \end{cases} \tag{3.7}$$

using a constant potential in the interstitial region and a spherically symmetric potential inside each sphere.

While the LAPW method yields accurate results for close-packed metal systems, the shape-approximation becomes difficult to justify for crystals with open structures such as silicides, perovskites, surfaces or clusters.

In the full-potential LAPW method (FLAPW) [59,60] any shape-approximation in the interstitial region and the muffin-tin are dropped. This generalization is achieved by relaxing the constant interstitial potential V_0^I and the spherical muffin-tin approximation $V_(^{MT}r)$ due to the inclusion of a "warped" interstitial $\sum V_I^{\mathbf{G}} e^{i\mathbf{Gr}}$ and the non-spherical terms inside the muffin-tin spheres:

$$V(\mathbf{r}) = \begin{cases} \sum\limits_{\mathbf{G}} V_{\mathbf{G}}^I e^{i\mathbf{Gr}} & \text{interstitial region} \\ \sum\limits_{L} V_L^{MT}(r) Y_L(\hat{\mathbf{r}}) & \text{muffin-tin } \mu\ . \end{cases} \tag{3.8}$$

This method became possible with the development of a technique for obtaining the Coulomb potential for a general periodic charge density without shape-approximation and with the inclusion of the Hamiltonian matrix elements due to the warped interstitial and non-spherical terms of the potential. The charge density is represented in the same way as the potential:

$$\rho(\mathbf{r}) = \begin{cases} \sum\limits_{\mathbf{G}} \rho_{\mathbf{G}}^I e^{i\mathbf{Gr}} & \text{interstitial region} \\ \sum\limits_{L} \rho_L^{MT}(r) Y_L(\hat{\mathbf{r}}) & \text{muffin-tin } \mu\ . \end{cases} \tag{3.9}$$

Detail of the solution of the Poisson equation for an arbitrarily shaped periodic potential are described in section 3.4.

3.1.4 The generalized eigenvalue problem

After discussing the FLAPW basis it is necessary to say a few words about the eigenvalue problem. The solution of eigenvalue problem has to be carried out separately for every Bloch vector. And, of course, the basis set and the Hamiltonian matrix have to be set up for each Bloch vector $\mathbf{k}$. However, I will not add the index $\mathbf{k}$ to the basis function and the Hamiltonian matrix.

There is one important fact that I have not mentioned so far. Even though planewaves form an orthogonal basis set, the FLAPW functions do not. The planewaves in the interstitial-region are non-orthogonal, because the muffin-tin are cut out, i.e. the integration, in term of which orthogonality is defined, dose not stretch over the whole unit cell, but only over interstitial region. An additional contribution comes from the muffin-tin. Even though the $u_l(r)Y_L$ and $\dot{u}_l(r)Y_L$ are mutually orthogonal, in general each planewave couples to all functions in the spheres.

Due to the non-orthogonality of the basis functions the overlap Matrix $\mathbf{S}$ defined by (3.10), is not a diagonal, but a symmetric, real matrix.

$$\mathbf{S}^{\mathbf{G'G}} = \int \varphi^*_{\mathbf{G'}}(\mathbf{r})\varphi_{\mathbf{G}}(\mathbf{r})d^3r \ . \tag{3.10}$$

In (the more convenient) Dirac notation the eigenvalue problem has the following form:

$$\mathcal{H}|\phi_i\rangle = \epsilon_i|\phi_i\rangle \tag{3.11}$$

where $|\phi_i\rangle$ denotes the eigenfunction corresponding to the i^{th} eigenvalue ϵ_i. Substituting the expansion of the eigenfunctions

$$|\phi_i\rangle = \sum_{\mathbf{G}} c_{i\mathbf{G}}|\varphi_{\mathbf{G}}\rangle \tag{3.12}$$

we obtain

$$\sum_{\mathbf{G}} c_{i\mathbf{G}}\mathcal{H}|\varphi_{\mathbf{G}}\rangle = \epsilon_i \sum_{\mathbf{G}} c_{i\mathbf{G}}|\varphi_{\mathbf{G}}\rangle \ . \tag{3.13}$$

Multiplying this form the left with$\langle\varphi_{\mathbf{G'}}|$ we find

$$\sum_{\mathbf{G}} c_{i\mathbf{G}}\langle\varphi_{\mathbf{G'}}|\mathcal{H}|\varphi_{\mathbf{G}}\rangle = \epsilon_i \sum_{\mathbf{G}} c_{i\mathbf{G}}\langle\varphi_{\mathbf{G'}}|\varphi_{\mathbf{G}}\rangle \tag{3.14}$$

which can be written in matrix form

$$\{\mathbf{H} - \epsilon_i\mathbf{S}\}\mathbf{c}_i = 0 \tag{3.15}$$

where the eigenvector $\mathbf{c}_i$ is the coefficient vector corresponding to the i^{th} eigenvalue (3.15) is called a generalized eigenvalue problem.

However, this problem can be reduced to a standard eigenvalue problem using the Cholesky decomposition. It can be shown (e.g. Stoer [61]), that any hermitian and positive definite matrix can be decomposed into a matrix product of a lower triangular matrix with only positive diagonal elements matrix and its transposed. Clearly, the overlap matrix satisfies these conditions and can be written

$$\mathbf{S} = \mathbf{L}\mathbf{L}^{\mathbf{tr}}, \tag{3.16}$$

therefore, (3.15) becomes

$$\mathbf{H}\mathbf{c}_i = \epsilon_i \mathbf{L}\mathbf{L}^{\mathbf{tr}}\mathbf{c}_i \ . \tag{3.17}$$

Multiplying form the left with $\mathbf{L}^{-1}$ and introducing a unit matrix we get

$$\mathbf{L}^{-1}\mathbf{H}(\mathbf{L}^{-1})^{tr}\mathbf{L}^{tr}\mathbf{c}_i = \epsilon_i \mathbf{L}^{tr}\mathbf{c}_i \ . \tag{3.18}$$

Defining

$$\mathbf{P} = \mathbf{L}^{-1}\mathbf{H}(\mathbf{L}^{-1})^{tr}\mathbf{L}^{tr}, \quad \mathbf{x_i} = \mathbf{L}^{tr}\mathbf{c}_i \ , \tag{3.19}$$

we finally have

$$\mathbf{P}\mathbf{x_i} = \epsilon_i \mathbf{x_i} \ . \tag{3.20}$$

Thus the generalized eigenvalue problem has been reduced to a simple eigenvalue problem. The eigenvectors c_i can be obtained by back-transformation

$$\mathbf{c}_i = (\mathbf{L}^{tr})^{-1}\mathbf{x_i}. \tag{3.21}$$

3.1.5 Film calculations within FLAPW

Nowadays the physics of surfaces is an field of major interest and investigation. However, surfaces are difficult to treat, because they break the translational symmetry, i.e. there is only the 2-dimensional symmetry parallel to the surface left to be used to reduce the problem, and a semi-infinite problem is left perpendicular to the surface. In our approach surfaces are approximated by thin films, typically 7-12 atomic layers thick. Obviously, this approximation, which is called the thin-film approximation, can only yield good results if the interaction between the two surfaces of the film is weak enough, so that each of them shows the properties of the surfaces of an ideal semi-infinite crystal.

In the case of film calculations space is divided into three distinct regions, the muffin-tins, the interstitial and the vacuum region (cf. Fig. 3.2). The interstitial region now stretches from $-D/2$ to $D/2$ in z-direction, which is defined to be the direction perpendicular to the film. The representation of the wavefunction inside the muffin-tin spheres remains exactly the same as in the bulk case. Since the periodicity along the z-direction is lost, the unit cell extends principally from $-\infty$ to ∞ in z-direction. Still the wavefunction can be expanded in term of planewaves. However, the wavevectors perpendicular to the film are not defined in terms of D, but in terms of $\tilde{D}$, which is chosen larger than D to gain greater variational freedom. If $D = \tilde{D}$ there would be a node at the vacuum boundary. Therefore, the planewaves have the form

$$\varphi_{\mathbf{G}_{||}\mathbf{G}_\perp}(\mathbf{k}_{||}, \mathbf{r}) = e^{i(\mathbf{G}_{||}+\mathbf{k}_{||})\mathbf{r}_{||}} e^{i\mathbf{G}_\perp z} \tag{3.22}$$

with

$$\mathbf{G}_\perp = \frac{2\pi n}{\tilde{D}} \tag{3.23}$$

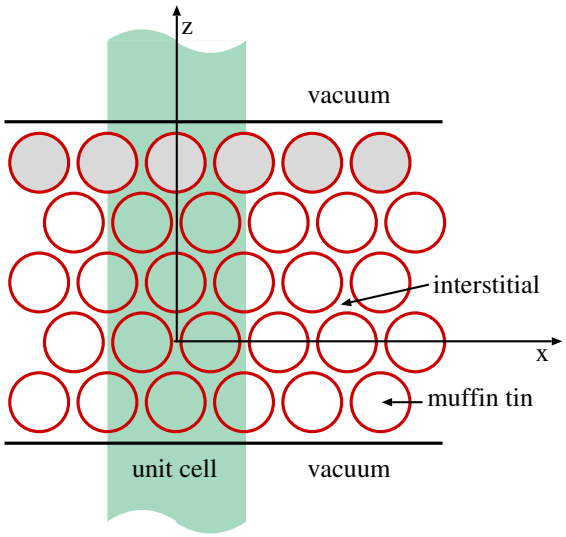

Figure 3.2: The unit cell in film calculations contain two semi-infinite vacuum regions.

where $\mathbf{G}_{||}$ and $\mathbf{k}_{||}$ are the 2-dimensional wave- and Bloch vectors, $\mathbf{r}_{||}$ is the parallel component of $\mathbf{r}$ and $\mathbf{G}_{\perp}$ is the wavevector perpendicular to the film. The basis function in the vacuum region are constructed in same spirit as the function in the muffin-tins. They consist of planewaves parallel to the film, and a z-dependent function $u_{\mathbf{G}_{||}}(\mathbf{k}_{||}, z)$, which solves the corresponding one-dimensional Schrödinger equation (3.24), plus its energy derivative $\dot{u}_{\mathbf{G}_{||}}(\mathbf{k}_{||}, z)$:

$$\left\{ -\frac{\hbar^2}{2m}\frac{\partial^2}{\partial z^2} + V_0(z) - E_{vac} + \frac{\hbar^2}{2m}(\mathbf{G}_{||} + \mathbf{k}_{||})^2 \right\} u_{\mathbf{G}_{||}}(\mathbf{k}_{||}, z) = 0 \,. \tag{3.24}$$

E_{vac} is the vacuum energy parameter and $V_0(z)$ is the planar averaged part of the vacuum potential. As in the case of $\dot{u}_l$ in the muffin-tin, the function $\dot{u}_{\mathbf{G}_{||}}(\mathbf{k}_{||}, z)$ is calculated from a Schrödinger-like equation, which can be obtained by taking the derivative of (3.24) with respect to the energy:

$$\left\{ -\frac{\hbar^2}{2m}\frac{\partial^2}{\partial z^2} + V_0(z) - E_{vac} + \frac{\hbar^2}{2m}(\mathbf{G}_{||} + \mathbf{k}_{||})^2 \right\} \dot{u}_{\mathbf{G}_{||}}(\mathbf{k}_{||}, z) = u_{\mathbf{G}_{||}}(\mathbf{k}_{||}, z). \tag{3.25}$$

The resulting basis functions have the form

$$\varphi_{\mathbf{G}_{||}\mathbf{G}_{\perp}}(\mathbf{k}_{||}, \mathbf{r}) = \left\{ A_{\mathbf{G}_{||}\mathbf{G}_{\perp}}(\mathbf{k}_{||}) u_{\mathbf{G}_{||}}(\mathbf{k}_{||}, z) + B_{\mathbf{G}_{||}\mathbf{G}_{\perp}}(\mathbf{k}_{||}) \dot{u}_{\mathbf{G}_{||}}(\mathbf{k}_{||}, z) \right\} e^{i(\mathbf{G}_{||}+\mathbf{k}_{||})\mathbf{r}_{||}} \tag{3.26}$$

The coefficients $A_{\mathbf{G}_{||}\mathbf{G}_{\perp}}(\mathbf{k}_{||})$ and $B_{\mathbf{G}_{||}\mathbf{G}_{\perp}}(\mathbf{k}_{||})$ are determined in exactly the same way as it done for the muffin-tin by requiring that the functions are continuous and differentiable at the vacuum boundary. It should be mentioned, that the vacuum basis functions offer less variational freedom than the basis set in the interstitial region

does. This can be seen by noting that there are only two functions, $u_{\mathbf{G}_{||}}$ and $\dot{u}_{\mathbf{G}_{||}}$ times the corresponding planar planewave, to be matched to all planewaves of the interstitial region with the same $\mathbf{G}_{||}$. But there are generally far more than two different $\mathbf{G}_{\perp}$'s, i.e. the number of basis functions in the vacuum region is significantly smaller than in the interstitial region.However, this can be improved rather easily. In equation (3.24) only one energy parameter E_{vac} is used. Instead one can used a whole series of parameters E^i_{vac} to cover an energy region. A possible choice of the energy parameters could be $E^i_{vac} = E^{\mathbf{G}_{\perp}}_{vac} = E_{vac} - \frac{\hbar^2}{2m}\mathbf{G}^2_{\perp}$, which leads correspondingly to $\mathbf{G}_{\perp}$ dependent basis functions $u_{\mathbf{G}_{||}\mathbf{G}_{\perp}}(\mathbf{k}_{||}, z)$. For more details see Ref. [62]. In general, however, the present approximations is accurate, the energy spectrum of the electrons in the vacuum region is small due to the work-function.

Finally we would like to summarize the basis set used for thin film calculation with the FLAPW method.

$$\varphi_{\mathbf{G}_{||}\mathbf{G}_{\perp}}(\mathbf{k}_{||}, \mathbf{r}) = \begin{cases} e^{i(\mathbf{G}_{||}+\mathbf{k}_{||})\mathbf{r}_{||}} e^{i\mathbf{G}_{\perp}z} & \text{Int.} \\ \left\{ A_{\mathbf{G}_{||}\mathbf{G}_{\perp}}(\mathbf{k}_{||}) u_{\mathbf{G}_{||}}(\mathbf{k}_{||}, z) + B_{\mathbf{G}_{||}\mathbf{G}_{\perp}}(\mathbf{k}_{||}) \dot{u}_{\mathbf{G}_{||}}(\mathbf{k}_{||}, z) \right\} e^{i(\mathbf{G}_{||}+\mathbf{k}_{||})\mathbf{r}_{||}} & \text{Vac.} \\ \sum_L A^{\mu\mathbf{G}}_L(\mathbf{k}) u_l(r) Y_L(\hat{\mathbf{r}}) + B^{\mu\mathbf{G}}_L(\mathbf{k}) \dot{u}_l(r) Y_L(\hat{\mathbf{r}}) & \text{MT}\mu \end{cases} \tag{3.27}$$

This expansion has been suggested by H.Krakauer, M.Posternak and A.J. Freeman [63].

3.2 Construction of the Hamiltonian matrix

The FLAPW Hamiltonian and overlap matrices consist of three contributions from the three regions into which the space is divided.

$$\mathbf{H} = \mathbf{H_I} + \mathbf{H_{MT}} + \mathbf{H_V} \tag{3.28}$$

$$\mathbf{S} = \mathbf{S_I} + \mathbf{S_{MT}} + \mathbf{S_V} \tag{3.29}$$

All three contributions have to be computed separately. Let's begin with the muffin-tin spheres.

3.2.1 Contribution of the muffin-tins

The contribution of the muffin-tin to the Hamiltonian matrix and the overlap matrix is given by:

$$H_{MT}^{\mathbf{G}'\mathbf{G}}(\mathbf{k}) = \sum_{\mu} \int_{MT^{\mu}} \left(\sum_{L'} A_{L'}^{\mu\mathbf{G}'}(\mathbf{k}) \varphi_{L'}^{\alpha}(\mathbf{r}) + B_{L'}^{\mu\mathbf{G}'}(\mathbf{k}) \dot{\varphi}_{L'}^{\alpha}(\mathbf{r}) \right)^{*} \mathcal{H}_{MT^{\alpha}} \left(\sum_{L} A_{L}^{\mu\mathbf{G}}(\mathbf{k}) \varphi_{L}^{\alpha}(\mathbf{r}) + B_{L}^{\mu\mathbf{G}}(\mathbf{k}) \dot{\varphi}_{L}^{\alpha}(\mathbf{r}) \right) d^3r \tag{3.30}$$

$$S_{MT}^{\mathbf{G}'\mathbf{G}}(\mathbf{k}) = \sum_{\mu} \int_{MT^{\mu}} \left(\sum_{L'} A_{L'}^{\mu\mathbf{G}'}(\mathbf{k}) \varphi_{L'}^{\alpha}(\mathbf{r}) + B_{L'}^{\mu\mathbf{G}'}(\mathbf{k}) \dot{\varphi}_{L'}^{\alpha}(\mathbf{r}) \right)^{*} \left(\sum_{L} A_{L}^{\mu\mathbf{G}}(\mathbf{k}) \varphi_{L}^{\alpha}(\mathbf{r}) + B_{L}^{\mu\mathbf{G}}(\mathbf{k}) \dot{\varphi}_{L}^{\alpha}(\mathbf{r}) \right) d^3r \tag{3.31}$$

with

$$\varphi_{L}^{\alpha}(\mathbf{r}) = u_l(r) Y_L(\hat{\mathbf{r}}), \quad \dot{\varphi}_{L}^{\alpha}(\mathbf{r}) = \dot{u}_l(r) Y_L(\hat{\mathbf{r}}) \, . \tag{3.32}$$

Where we distinguish between the atom index μ and the atom type index $\alpha(\mu)$. In most applications the are symmetry equivalent atom in the unit cell, i.e. some atoms can be mapped into each other by space group operations. Clearly, these atom must possess the same physical properties, e.g. the potential has to be equal. As a consequence, the Hamiltonian and the basis functions $\varphi_{L}^{\alpha}(\mathbf{r})$ do not differ among the atoms of the same type. This fact is exploited in that the muffin-tin potential of an atom type is only stored once for the representative atom, and the matrices eq(3.34)-(3.37) is also calculated for representative only. $\mathcal{H}_{MT^{\mu}}$ is scalar relativistic Hamiltonian operator. It can be split up into two parts, the spherical Hamiltonian $\mathcal{H}_{sp}$ and the nonspherical contributions to the potential V_{ns}:

$$\mathcal{H}_{MT^{\alpha}} = \mathcal{H}_{sp} + V_{ns}^{\alpha} \, . \tag{3.33}$$

The above integrations contain the following matrix elements:

$$t_{L'L}^{\alpha\varphi\varphi} = \int_{MT^{\alpha}} \varphi_{L'}^{\alpha}(\mathbf{r}) \mathcal{H}_{MT^{\alpha}} \varphi_{L}^{\alpha}(\mathbf{r}) d^3r \tag{3.34}$$

$$t_{L'L}^{\alpha\varphi\dot{\varphi}} = \int_{MT^{\alpha}} \varphi_{L'}^{\alpha}(\mathbf{r}) \mathcal{H}_{MT^{\alpha}} \dot{\varphi}_{L}^{\alpha}(\mathbf{r}) d^3r \tag{3.35}$$

$$t_{L'L}^{\alpha\dot{\varphi}\varphi} = \int_{MT^{\alpha}} \dot{\varphi}_{L'}^{\alpha}(\mathbf{r}) \mathcal{H}_{MT^{\alpha}} \varphi_{L}^{\alpha}(\mathbf{r}) d^3r \tag{3.36}$$

$$t_{L'L}^{\alpha\dot{\varphi}\dot{\varphi}} = \int_{MT^{\alpha}} \dot{\varphi}_{L'}^{\alpha}(\mathbf{r}) \mathcal{H}_{MT^{\alpha}} \dot{\varphi}_{L}^{\alpha}(\mathbf{r}) d^3r \tag{3.37}$$

These matrix elements do not depend on the $A_{L}^{\mu\mathbf{G}}(\mathbf{k})$ and $B_{L}^{\mu\mathbf{G}}(\mathbf{k})$ coefficients. Thus, they are independent of Bloch vector and need to be calculated only once per iteration.

The functions φ_L^α and$\dot{\varphi}_L^\alpha$ have been constructed to diagonalize the spherical part $\mathcal{H}_{sp}^\alpha$ of the muffin-tin Hamiltonian $\mathcal{H}_{MT^\alpha}$:

$$\mathcal{H}_{sp}^\alpha \varphi_L^\alpha = E_l \varphi_L^\alpha \,, \tag{3.38}$$

$$\mathcal{H}_{sp}^\alpha \dot{\varphi}_L^\alpha = E_l \dot{\varphi}_L^\alpha + \varphi_L^\alpha \,. \tag{3.39}$$

Multiplying these equations with $\varphi_{L'}^\alpha(\mathbf{r})$ and $\dot{\varphi}_L^\alpha(\mathbf{r})$ respectively and integrating over the muffin-tins gives

$$\langle \varphi_{L'}^\alpha | \mathcal{H}_{sp}^\alpha | \varphi_L^\alpha \rangle_{MT^\alpha} = \delta_{ll'}\delta_{mm'} E_l \tag{3.40}$$

$$\langle \varphi_{L'}^\alpha | \mathcal{H}_{sp}^\alpha | \dot{\varphi}_L^\alpha \rangle_{MT^\alpha} = \delta_{ll'}\delta_{mm'} \tag{3.41}$$

$$\langle \dot{\varphi}_{L'}^\alpha | \mathcal{H}_{sp}^\alpha | \varphi_L^\alpha \rangle_{MT^\alpha} = 0 \tag{3.42}$$

$$\langle \dot{\varphi}_{L'}^\alpha | \mathcal{H}_{sp}^\alpha | \dot{\varphi}_L^\alpha \rangle_{MT^\alpha} = \delta_{ll'}\delta_{mm'} E_l \langle \dot{\varphi}_{L'}^\alpha | \dot{\varphi}_L^\alpha \rangle_{MT^\alpha} \tag{3.43}$$

where the normalization condition for φ_L^α has been used. So, only the expectation values of the nonspherical part of the potential are left to be determined. The potential is also expanded into a product of radial functions and spherical harmonics (3.44), the corresponding integrals consist of product of a radial integrals and an angular integrals over three spherical harmonics, the so-called gaunt coefficients.

$$V^\alpha(\mathbf{r}) = \sum_{L''} V_{L''}^\alpha(r) Y_{L''}(\hat{\mathbf{r}}) \tag{3.44}$$

$$t_{L'L}^{\alpha\varphi\varphi} = \sum_{l''} I_{l'll''}^{\alpha\varphi\varphi} G_{l'll''}^{m'mm''} + \delta_{ll'}\delta_{mm'} E_l \tag{3.45}$$

$$t_{L'L}^{\alpha\varphi\dot{\varphi}} = \sum_{l''} I_{l'll''}^{\alpha\varphi\dot{\varphi}} G_{l'll''}^{m'mm''} + \delta_{ll'}\delta_{mm'} \tag{3.46}$$

$$t_{L'L}^{\alpha\dot{\varphi}\varphi} = \sum_{l''} I_{l'll''}^{\alpha\dot{\varphi}\varphi} G_{l'll''}^{m'mm''} \tag{3.47}$$

$$t_{L'L}^{\alpha\dot{\varphi}\dot{\varphi}} = \sum_{l''} I_{l'll''}^{\alpha\dot{\varphi}\dot{\varphi}} G_{l'll''}^{m'mm''} + \delta_{ll'}\delta_{mm'} E_l \langle \dot{\varphi}_{lm}^\alpha | \dot{\varphi}_{lm}^\alpha \rangle_{MT^\alpha} \tag{3.48}$$

with

$$I_{l'll''}^{\alpha\varphi\varphi} = \int (g_{l'}^\alpha(r) g_l^\alpha(r) + \phi_{l'}^\alpha(r)\phi_l^\alpha(r)) V_{l''}^\alpha(r) r^2 dr \tag{3.49}$$

$$I_{l'll''}^{\alpha\varphi\dot{\varphi}} = \int (g_{l'}^\alpha(r) \dot{g}_l^\alpha(r) + \phi_{l'}^\alpha(r)\dot{\phi}_l^\alpha(r)) V_{l''}^\alpha(r) r^2 dr \tag{3.50}$$

$$I_{l'll''}^{\alpha\dot{\varphi}\varphi} = \int (\dot{g}_{l'}^\alpha(r) g_l^\alpha(r) + \dot{\phi}_{l'}^\alpha(r)\phi_l^\alpha(r)) V_{l''}^\alpha(r) r^2 dr \tag{3.51}$$

$$I_{l'll''}^{\alpha\dot{\varphi}\dot{\varphi}} = \int (\dot{g}_{l'}^\alpha(r) \dot{g}_l^\alpha(r) + \dot{\phi}_{l'}^\alpha(r)\dot{\phi}_l^\alpha(r)) V_{l''}^\alpha(r) r^2 dr \tag{3.52}$$

and

$$G_{ll'l''}^{mm'm''} = \int Y_{lm}^* Y_{l'm'}^* Y_{l''m''}^* d\Omega \,. \tag{3.53}$$

The I matrices contain the radial integrals. Finally, the Hamiltonian and overlap matrix elements become

$$\begin{aligned} H_{MT}^{\mathbf{G}'\mathbf{G}}(\mathbf{k}) = \; & \sum_{\mu} \sum_{L'L} (A_{L'}^{\mu\mathbf{G}'}(\mathbf{k}))^* t_{L'L}^{\alpha\varphi\varphi} A_L^{\mu\mathbf{G}}(\mathbf{k}) + (B_{L'}^{\mu\mathbf{G}'}(\mathbf{k}))^* t_{L'L}^{\alpha\dot{\varphi}\dot{\varphi}} B_L^{\mu\mathbf{G}}(\mathbf{k}) \\ & + (A_{L'}^{\mu\mathbf{G}'}(\mathbf{k}))^* t_{L'L}^{\alpha\varphi\dot{\varphi}} B_L^{\mu\mathbf{G}}(\mathbf{k}) + (B_{L'}^{\mu\mathbf{G}'}(\mathbf{k}))^* t_{L'L}^{\alpha\dot{\varphi}\varphi} A_L^{\mu\mathbf{G}}(\mathbf{k}) \end{aligned} \tag{3.54}$$

$$S_{MT}^{\mathbf{G}'\mathbf{G}}(\mathbf{k}) = \sum_{\mu} \sum_{L} (A_{L'}^{\mu\mathbf{G}'}(\mathbf{k}))^* A_L^{\mu\mathbf{G}}(\mathbf{k}) + (B_{L'}^{\mu\mathbf{G}'}(\mathbf{k}))^* B_L^{\mu\mathbf{G}}(\mathbf{k}) \langle \dot{\varphi}_L^{\alpha} | \dot{\varphi}_L^{\alpha} \rangle_{MT^{\mu}}. \tag{3.55}$$

3.2.2 The vacuum contribution

The vacuum contribution to the Hamiltonian and overlap matrix are given by:

$$\begin{aligned} H_V^{\mathbf{G}'\mathbf{G}}(\mathbf{k}_{||}) = \; & \int_V \Big(\big\{ A_{\mathbf{G}'_{||}G'_{\perp}}(\mathbf{k}_{||}) u_{\mathbf{G}'_{||}}(\mathbf{k}_{||}, z) + B_{\mathbf{G}'_{||}G'_{\perp}}(\mathbf{k}_{||}) \dot{u}_{\mathbf{G}'_{||}}(\mathbf{k}_{||}, z) \big\} e^{i(\mathbf{G}'_{||} + \mathbf{k}_{||})\mathbf{r}_{||}} \Big)^* \\ & \mathcal{H}_V \Big(\big\{ A_{\mathbf{G}_{||}G_{\perp}}(\mathbf{k}_{||}) u_{\mathbf{G}_{||}}(\mathbf{k}_{||}, z) + B_{\mathbf{G}_{||}G_{\perp}}(\mathbf{k}_{||}) \dot{u}_{\mathbf{G}_{||}}(\mathbf{k}_{||}, z) \big\} e^{i(\mathbf{G}_{||} + \mathbf{k}_{||})\mathbf{r}_{||}} \Big) d^3 r \\ S_V^{\mathbf{G}'\mathbf{G}}(\mathbf{k}_{||}) = \; & \int_V \Big(\big\{ A_{\mathbf{G}'_{||}G'_{\perp}}(\mathbf{k}_{||}) u_{\mathbf{G}'_{||}}(\mathbf{k}_{||}, z) + B_{\mathbf{G}'_{||}G'_{\perp}}(\mathbf{k}_{||}) \dot{u}_{\mathbf{G}'_{||}}(\mathbf{k}_{||}, z) \big\} e^{i(\mathbf{G}'_{||} + \mathbf{k}_{||})\mathbf{r}_{||}} \Big)^* \\ & \Big(\big\{ A_{\mathbf{G}_{||}G_{\perp}}(\mathbf{k}_{||}) u_{\mathbf{G}_{||}}(\mathbf{k}_{||}, z) + B_{\mathbf{G}_{||}G_{\perp}}(\mathbf{k}_{||}) \dot{u}_{\mathbf{G}_{||}}(\mathbf{k}_{||}, z) \big\} e^{i(\mathbf{G}_{||} + \mathbf{k}_{||})\mathbf{r}_{||}} \Big) d^3 r. \end{aligned} \tag{3.56}$$

The treatment of the vacuum region in FLAPW is in many ways similar to the treatment of the muffin-tins. As in the muffin-tin the basis functions are constructed to diagonalize only a certain part of the Hamiltonian. Here this part of the Hamiltonian includes only the non-corrugated planar averaged part of the potential $(V_{nc}(z))$, that depends only on z.

$$\mathcal{H}_V = \mathcal{H}_{nc} + V_{co}(\mathbf{r}) \tag{3.57}$$

The t-matrices can be defined in the same way as inside the muffin-tin spheres(3.34)(3.34)

$$t_{\mathbf{G}'_{||}\mathbf{G}_{||}}^{uu}(\mathbf{k}_{||}) = \langle \varphi_{\mathbf{G}'_{||}}(\mathbf{k}_{||}) | \mathcal{H}_V | \varphi_{\mathbf{G}_{||}}(\mathbf{k}_{||}) \rangle_V \tag{3.58}$$

$$t_{\mathbf{G}'_{||}\mathbf{G}_{||}}^{u\dot{u}}(\mathbf{k}_{||}) = \langle \varphi_{\mathbf{G}'_{||}}(\mathbf{k}_{||}) | \mathcal{H}_V | \dot{\varphi}_{\mathbf{G}_{||}}(\mathbf{k}_{||}) \rangle_V \tag{3.59}$$

$$t_{\mathbf{G}'_{||}\mathbf{G}_{||}}^{\dot{u}u}(\mathbf{k}_{||}) = \langle \dot{\varphi}_{\mathbf{G}'_{||}}(\mathbf{k}_{||}) | \mathcal{H}_V | \varphi_{\mathbf{G}_{||}}(\mathbf{k}_{||}) \rangle_V \tag{3.60}$$

$$t_{\mathbf{G}'_{||}\mathbf{G}_{||}}^{\dot{u}\dot{u}}(\mathbf{k}_{||}) = \langle \dot{\varphi}_{\mathbf{G}'_{||}}(\mathbf{k}_{||}) | \mathcal{H}_V | \dot{\varphi}_{\mathbf{G}_{||}}(\mathbf{k}_{||}) \rangle_V. \tag{3.61}$$

The contribution to these matrices from $\mathcal{H}_{nc}$, are given by the analog of equations (3.41)-(3.44). The corrugated potential is expanded into z-dependent functions and planewaves in the $x-y$ plane

$$V_{co}(\mathbf{r}) = \sum_{\mathbf{G''}_{||}} V_{\mathbf{G''}_{||}}(z) e^{i\mathbf{G''}_{||}\mathbf{r}}, \tag{3.62}$$

The contribution due to the expectation values of $V_{co}(\mathbf{r})$ consists of a z-dependent integral and an integral in the x-y-plane of the following form

$$\int e^{-i\mathbf{G'}_{||}\mathbf{r}} e^{i\mathbf{G''}_{||}\mathbf{r}} e^{i\mathbf{G}_{||}\mathbf{r}} dxdy = \delta_{\mathbf{G'}_{||}}(\mathbf{G}_{||} + \mathbf{G''}_{||}). \tag{3.63}$$

Thus, the t-matrices are finally given by

$$t^{uu}_{\mathbf{G'}_{||}\mathbf{G}_{||}}(\mathbf{k}_{||}) = I^{uu}_{\mathbf{G'}_{||}\mathbf{G}_{||}(\mathbf{G'}_{||}-\mathbf{G}_{||})}(\mathbf{k}_{||}) + \delta_{\mathbf{G'}_{||}\mathbf{G}_{||}} E_{vac} \tag{3.64}$$

$$t^{u\dot{u}}_{\mathbf{G'}_{||}\mathbf{G}_{||}}(\mathbf{k}_{||}) = I^{u\dot{u}}_{\mathbf{G'}_{||}\mathbf{G}_{||}(\mathbf{G'}_{||}-\mathbf{G}_{||})}(\mathbf{k}_{||}) + \delta_{\mathbf{G'}_{||}\mathbf{G}_{||}} \tag{3.65}$$

$$t^{\dot{u}u}_{\mathbf{G'}_{||}\mathbf{G}_{||}}(\mathbf{k}_{||}) = I^{\dot{u}u}_{\mathbf{G'}_{||}\mathbf{G}_{||}(\mathbf{G'}_{||}-\mathbf{G}_{||})}(\mathbf{k}_{||}) \tag{3.66}$$

$$t^{\dot{u}\dot{u}}_{\mathbf{G'}_{||}\mathbf{G}_{||}}(\mathbf{k}_{||}) = I^{\dot{u}\dot{u}}_{\mathbf{G'}_{||}\mathbf{G}_{||}(\mathbf{G'}_{||}-\mathbf{G}_{||})}(\mathbf{k}_{||}) + \delta_{\mathbf{G}_{||}\mathbf{G}_{||}} E_{vac} \langle \dot{u}_{\mathbf{G'}_{||}}(\mathbf{k}_{||}) | \dot{u}_{\mathbf{G}_{||}}(\mathbf{k}_{||}) \rangle_V \tag{3.67}$$

Where the I matrices abbreviate the z-dependent integrals including $V_{(\mathbf{G'}_{||}-\mathbf{G}_{||})}(z)$

$$I^{uu}_{\mathbf{G'}_{||}\mathbf{G}_{||}\mathbf{G''}_{||}}(\mathbf{k}_{||}) = \int u_{\mathbf{G'}_{||}}(\mathbf{k}_{||}) u_{\mathbf{G}_{||}}(\mathbf{k}_{||}) V_{\mathbf{G''}_{||}}(z) dz \tag{3.68}$$

$$I^{u\dot{u}}_{\mathbf{G'}_{||}\mathbf{G}_{||}\mathbf{G''}_{||}}(\mathbf{k}_{||}) = \int u_{\mathbf{G'}_{||}}(\mathbf{k}_{||}) \dot{u}_{\mathbf{G}_{||}}(\mathbf{k}_{||}) V_{\mathbf{G''}_{||}}(z) dz \tag{3.69}$$

$$I^{\dot{u}u}_{\mathbf{G'}_{||}\mathbf{G}_{||}\mathbf{G''}_{||}}(\mathbf{k}_{||}) = \int \dot{u}_{\mathbf{G'}_{||}}(\mathbf{k}_{||}) u_{\mathbf{G}_{||}}(\mathbf{k}_{||}) V_{\mathbf{G''}_{||}}(z) dz \tag{3.70}$$

$$I^{\dot{u}\dot{u}}_{\mathbf{G'}_{||}\mathbf{G}_{||}\mathbf{G''}_{||}}(\mathbf{k}_{||}) = \int \dot{u}_{\mathbf{G'}_{||}}(\mathbf{k}_{||}) \dot{u}_{\mathbf{G}_{||}}(\mathbf{k}_{||}) V_{\mathbf{G''}_{||}}(z) dz \tag{3.71}$$

The Hamiltonian and overlap matrix elements are calculated according to

$$\begin{aligned} H_V^{\mathbf{G'G}}(\mathbf{k}_{||}) = \; & A^*_{\mathbf{G'}}(\mathbf{k}_{||})) t^{uu}_{\mathbf{G'}_{||}\mathbf{G}_{||}}(\mathbf{k}_{||}) A_{\mathbf{G}}(\mathbf{k}_{||}) \\ & + A^*_{\mathbf{G'}}(\mathbf{k}_{||})) t^{u\dot{u}}_{\mathbf{G'}_{||}\mathbf{G}_{||}}(\mathbf{k}_{||}) B_{\mathbf{G}}(\mathbf{k}_{||}) \\ & + B^*_{\mathbf{G'}}(\mathbf{k}_{||})) t^{\dot{u}u}_{\mathbf{G'}_{||}\mathbf{G}_{||}}(\mathbf{k}_{||}) A_{\mathbf{G}}(\mathbf{k}_{||}) \\ & + B^*_{\mathbf{G'}}(\mathbf{k}_{||})) t^{\dot{u}\dot{u}}_{\mathbf{G'}_{||}\mathbf{G}_{||}}(\mathbf{k}_{||}) B_{\mathbf{G}}(\mathbf{k}_{||}) \end{aligned} \tag{3.72}$$

$$\begin{aligned} S_V^{\mathbf{G'G}}(\mathbf{k}_{||}) = \; & A^*_{\mathbf{G'}}(\mathbf{k}_{||}) A_{\mathbf{G}}(\mathbf{k}_{||}) \delta_{\mathbf{G'}_{||}\mathbf{G}_{||}} \\ & + B^*_{\mathbf{G'}}(\mathbf{k}_{||}) B_{\mathbf{G}}(\mathbf{k}_{||}) \langle \dot{u}_{\mathbf{G'}_{||}}(\mathbf{k}_{||}) | \dot{u}_{\mathbf{G}_{||}}(\mathbf{k}_{||}) \rangle_V \delta_{\mathbf{G'}_{||}\mathbf{G}_{||}} \end{aligned} \tag{3.73}$$

3.2.3 The interstitial contribution

The interstitial contribution to Hamiltonian and overlap matrix have the following form

$$H_I^{\mathbf{GG'}} = \frac{1}{\Omega}\int_I e^{-i(\mathbf{G}+\mathbf{k})\mathbf{r}}\Big(-\frac{\hbar^2}{2m}\Delta + V(\mathbf{r})\Big)e^{i(\mathbf{G'}+\mathbf{k})\mathbf{r}}d^3r \tag{3.74}$$

$$S_I^{\mathbf{GG'}} = \frac{1}{\Omega}\int_I e^{-i(\mathbf{G}+\mathbf{k})\mathbf{r}}e^{i(\mathbf{G}+\mathbf{k})\mathbf{r}}d^3r \tag{3.75}$$

The potential is also expanded into planewaves in the interstitial region.

$$V(\mathbf{r}) = \sum_G V_G e^{i\mathbf{G}\mathbf{r}} \tag{3.76}$$

Without the existence of the muffin-tin spheres the integration would stretch over the entire unit cell and the integration becomes rather simple. The kinetic energy is diagonal in momentum space and the potential is local, diagonal is real space and of convolution form in momentum space.

$$H_I^{\mathbf{GG'}}(\mathbf{r}) = \frac{\hbar^2}{2m}|\mathbf{G}+\mathbf{k}|^2\delta_{\mathbf{GG'}} + V_{(\mathbf{G}-\mathbf{G'})} \tag{3.77}$$

$$S_I^{\mathbf{GG'}} = \delta_{\mathbf{GG'}} \tag{3.78}$$

However, these matrix elements are not as straightforward to calculate as they appear at first glance, because of the complicated structure of the interstitial region. The integration has to be performed only in between the muffin-tins. Therefore, a step function $\Theta(\mathbf{r})$ has to be introduced, that cuts out the muffin-tins.

$$\Theta(\mathbf{r}) = \begin{cases} 1 & \text{in the interstitial region} \\ 0 & \text{muffin-tins} \end{cases} \tag{3.79}$$

In film calculation the region between $D/2$ and $\tilde{D}/2$ has to be cut out too, but to keep it simple we will discuss the only bulk case in this section. Using the step function the matrix elements can be written:

$$\begin{aligned} H_I^{\mathbf{GG'}} = \; & \frac{1}{\Omega}\int_{cell} e^{-i(\mathbf{G}-\mathbf{G'})\mathbf{r}}V(\mathbf{r})\Theta(\mathbf{r})d^3r \\ & +\tfrac{1}{2}(\mathbf{G'}+\mathbf{k})^2\frac{1}{\Omega}\int_{cell} e^{-i(\mathbf{G}-\mathbf{G'})\mathbf{r}}\Theta(\mathbf{r})d^3r \end{aligned} \tag{3.80}$$

$$S_I^{\mathbf{GG'}} = \frac{1}{\Omega}\int_{cell} e^{-i(\mathbf{G}-\mathbf{G'})\mathbf{r}}\Theta(\mathbf{r})d^3r. \tag{3.81}$$

In momentum space (3.80) becomes:

$$H_I^{\mathbf{GG'}} = (V\Theta)_{(\mathbf{G}-\mathbf{G'})} + \frac{\hbar}{2m}(\mathbf{G'}+\mathbf{k})^2\Theta_{(\mathbf{G}-\mathbf{G'})} \tag{3.82}$$

$$S_I^{\mathbf{G}\mathbf{G}'} = \Theta_{(\mathbf{G}-\mathbf{G}')} \tag{3.83}$$

Where $\Theta_{\mathbf{G}}$ and $(V\Theta)_{\mathbf{G}}$ are Fourier coefficients of $\Theta(\mathbf{r})$ and $V(\mathbf{r})\Theta(\mathbf{r})$ respectively. Apparently these coefficients are needed up to a cut-off of $2G_{max}$. The step function can be Fourier transformed analytically.

$$\Theta_{\mathbf{G}} = \delta_{\mathbf{G},\mathbf{0}} - \sum_{\mu} e^{i\mathbf{G}\mathbf{p}^{\mu}} \frac{4\pi (R_{MT}^{\alpha})^3}{\Omega} \frac{j_1(GR_{MT}^{\alpha})}{GR_{MT}^{\alpha}}$$

The Fourier transform of the product of $V(\mathbf{r})$ and $\Theta(\mathbf{r})$ is given by a convolution in momentum space.

$$(V\Theta)_{\mathbf{G}} = \sum_{\mathbf{G}'} V_{\mathbf{G}'}\Theta_{(\mathbf{G}-\mathbf{G}')} \tag{3.84}$$

This convolution depends on both, $\mathbf{G}$ and $\mathbf{G}'$, therefore the numerical effort increases like$(G_{max})^6$. However,$(V\Theta)_{\mathbf{G}}$ can be determined more efficiently, using Fast-Fourier-transformation (FFT) . In fig 3.3 it is shown schematically how $(V\Theta)_{\mathbf{G}}$ can be obtained using FFT. Using this scheme the numerical effort increases like$(G_{max})^3 ln((G_{max})^3)$

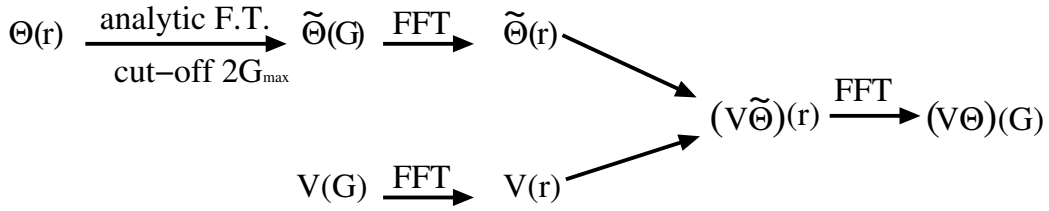

Figure 3.3: Schematic representation of the calculation of $(V\Theta)_{\mathbf{G}}$ First $\Theta(\mathbf{r})$ is Fourier transformed analytically with a cut-off $2G_{max}$ yielding $\tilde{\Theta}_{\mathbf{G}}$. Then $\tilde{\Theta}_{\mathbf{G}}$ and$V_{\mathbf{G}}$ are fast Fourier transformed and multiplied on real space mesh. Finally, the result$(V\tilde{\Theta})(\mathbf{r})$ is back-transformed to momentum space.

3.2.4 The muffin-tin A- and B-coefficients

Within the FLAPW method the electron wavefunction are expanded differently in the interstitial region and the muffin-tins. Each basis function consists of a planewave in the interstitial, which is matched to the radial functions and spherical harmonics in the muffin-tins. The coefficient of the function inside the spheres are determined from the requirement, that the basis functions and their derivatives are continuous at the sphere boundaries. These coefficients play an important role. In this section we will, therefore, discuss how matching conditions can be solved and what properties they induce.

In many systems, that the FLAPW method can be applied to, some atoms are symmetry equivalent, i.e. these atoms can be mapped onto each other by a space group operation $\{\mathbf{R}|\tau\}$. Such a group of atoms is called an atom type, represented by one of the atoms. Let $\{\mathbf{R}^\mu|\tau^\mu\}$ the operation that maps the atom μ onto its representative. This atom can now be assigned a local coordinate frame S^μ (cf. Fig. 3.4), where the origin of S^μ is at the atoms position $\mathbf{p}^\mu$. The local frame is chosen such that the unit vectors of the local frame S^μ are mapped onto those of the global frame by $\mathbf{R}^g$ ($\mathbf{R}^\mu S^\mu = S^g$). The local frame of the representative atom S^α is only translated with respect to the global frame, i.e. the same rotation $\mathbf{R}^\mu$ maps S^μ onto S^α. The potential (and other quantities) inside the muffin-tins can now be written in terms of the local coordinate system. Due to symmetry we find $V_{MT^\alpha}(\mathbf{r}^\alpha) = V_{MT^\mu}(\mathbf{r}^\mu)$, where $\mathbf{r}^\alpha$ and $\mathbf{r}^\mu$ are expanded in terms of the local frames S^α and S^μ respectively. As a consequence the radial functions $u_l(r)$ and the t-matrices are the same for all atoms of the same type. This way symmetry is exploited to save memory and computer time (during the calculation of the t-matrices).

Any planewave can be expanded into spherical harmonics via the Rayleigh expansion

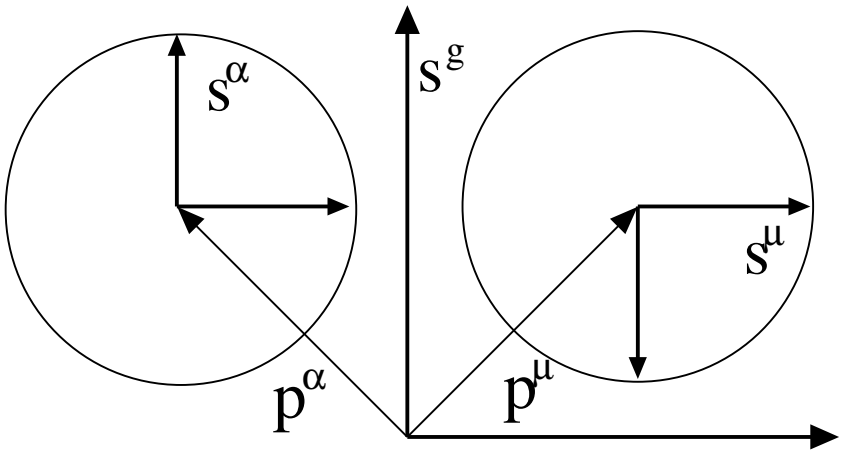

Figure 3.4: Local coordinate frames inside each muffin-tin

$$e^{i\mathbf{Kr}} = 4\pi \sum_L i^l j_l(rK) Y_L^*(\hat{\mathbf{K}}) Y_L(\hat{\mathbf{r}}) \tag{3.85}$$

where $r = |\mathbf{r}|$, $K = |\mathbf{K}|$ and $\mathbf{K}$ abbreviates $(\mathbf{G} + \mathbf{k})$. Looked at from the the

local frame $\mathbf{K}$ and $\mathbf{p}^\mu$ appear rotated, besides the origin of the local frame is shifted. Therefore, the planwave has the following form in the local frame:

$$e^{i(\mathbf{R}^\mu\mathbf{K})(\mathbf{r}+\mathbf{R}^\mu\mathbf{p}^\mu)} \; . \tag{3.86}$$

Thus, the Rayleigh expansion of the planewave in the local frame is given by:

$$e^{i\mathbf{K}\mathbf{p}^\mu} 4\pi \sum_L i^l j_l(rK) Y_L^*(\mathbf{R}^\mu\hat{\mathbf{K}}) Y_L(\hat{\mathbf{r}}) \; . \tag{3.87}$$

The requirement of continuity of the wavefunctions at the sphere boundary leads to the equation:

$$\begin{aligned} &\sum_L A_L^{\mu\mathbf{G}}(\mathbf{k}) u_l(R_{MT^\alpha}) Y_L(\hat{\mathbf{r}}) + B_L^{\mu\mathbf{G}}(\mathbf{k}) \dot{u}_l(R_{MT^\alpha}) Y_L(\hat{\mathbf{r}}) \\ &= e^{i\mathbf{K}\mathbf{p}^\mu} 4\pi \sum_L i^l j_l(rK) Y_L^*(\mathbf{R}^\mu\hat{\mathbf{K}}) Y_L(\hat{\mathbf{r}}) \end{aligned} \tag{3.88}$$

where R_{MT^α} is the muffin-tin radius of the atom type α. The second requirement is, that the derivative with respect to r, denoted by $\partial/\partial r = '$, is also continuous.

$$\begin{aligned} &\sum_L A_L^{\mu\mathbf{G}}(\mathbf{k}) u_l'(R_{MT^\alpha}) Y_L(\hat{\mathbf{r}}) + B_L^{\mu\mathbf{G}}(\mathbf{k}) \dot{u}_l'(R_{MT^\alpha}) Y_L(\hat{\mathbf{r}}) \\ &= e^{i\mathbf{K}\mathbf{p}^\mu} 4\pi \sum_L i^l j_l'(rK) Y_L^*(\mathbf{R}^\mu\hat{\mathbf{K}}) Y_L(\hat{\mathbf{r}}) \end{aligned} \tag{3.89}$$

These conditions can only be satisfied, if the coefficients of each spherical harmonic $Y_L(\hat{\mathbf{r}})$ are equal. Solving the resulting equations for $A_L^{\mu\mathbf{G}}(\mathbf{k})$ and $B_L^{\mu\mathbf{G}}(\mathbf{k})$ yields:

$$\begin{aligned} A_L^{\mu\mathbf{G}}(\mathbf{K}) = \; & e^{i\mathbf{K}\mathbf{p}^\mu} 4\pi \tfrac{1}{W} i^l Y_L^*(\mathbf{R}^\mu\hat{\mathbf{K}}) \\ & [\dot{u}_l(R_{MT^\alpha}) K j_l'(R_{MT^\alpha}K) - \dot{u}_l'(R_{MT^\alpha}) j_l(R_{MT^\alpha}K)] \\ B_L^{\mu\mathbf{G}}(\mathbf{K}) = \; & e^{i\mathbf{K}\mathbf{p}^\mu} 4\pi \tfrac{1}{W} i^l Y_L^*(\mathbf{R}^\mu\hat{\mathbf{K}}) \\ & [u_l'(R_{MT^\alpha}) j_l(R_{MT^\alpha}K) - u_l(R_{MT^\alpha}) K j_l'(R_{MT^\alpha}K)] \; . \end{aligned} \tag{3.90}$$

The Wronskian W is given by:

$$W = [\dot{u}_l(R_{MT^\alpha}) u_l'(R_{MT^\alpha}) - u_l(R_{MT^\alpha}) \dot{u}_l'(R_{MT^\alpha})] \tag{3.91}$$

Transformation of the FLAPW basis functions in systems that possess inversion symmetry

Planewaves transform in very simple way under the operation $\mathbf{r} \to -\mathbf{r}$. Let $\mathcal{I}$ be the inversion operator:

$$\mathcal{I} e^{i\mathbf{K}\mathbf{r}} = e^{-i\mathbf{K}\mathbf{r}} = \left(e^{i\mathbf{K}\mathbf{r}}\right)^* \tag{3.92}$$

The FLAPW basis functions still have this property, i.e. $\varphi_{\mathbf{G}}(\mathbf{k}, -\mathbf{r}) = \varphi_{\mathbf{G}}^*(\mathbf{k}, \mathbf{r})$. Clearly, the system must possess inversion symmetry, because only if there is an

equivalent atom at the position $-\mathbf{p}^\mu$ to each atom μ at position $\mathbf{p}^\mu$, the basis functions inside the corresponding spheres can be complex conjugates. The function $\varphi_{\mathbf{G}}(\mathbf{k},\mathbf{r})$ inside the muffin-tin μ is give by:

$$\varphi_{\mathbf{G}}(\mathbf{k},\mathbf{r}) = \sum_L A_L^{\mu\mathbf{G}}(\mathbf{k}) u_l(r) Y_L(\hat{\mathbf{r}}) + B_L^{\mu\mathbf{G}}(\mathbf{k}) \dot{u}_l(r) Y_L(\hat{\mathbf{r}}) \tag{3.93}$$

The vector $-\mathbf{r}$ lies in the opposite muffin-tin at the position $-\mathbf{p}^\mu$. Let's denote this atom by $-\mu$ Thus, we find:

$$\varphi_{\mathbf{G}}(\mathbf{k},\mathbf{r}) = \sum_L A_L^{-\mu\mathbf{G}}(\mathbf{k}) u_l(r) Y_L(\hat{\mathbf{r}}) + B_L^{-\mu\mathbf{G}}(\mathbf{k}) \dot{u}_l(r) Y_L(\hat{\mathbf{r}}) \tag{3.94}$$

The argument of the spherical harmonic is $\hat{\mathbf{r}}$ rather than $-\hat{\mathbf{r}}$, because the vector is expanded in the local frame of the atom $-\mu$. Substituting the explicit form of $A_L^{-\mu\mathbf{G}}(\mathbf{k})$ and $B_L^{-\mu\mathbf{G}}(\mathbf{k})$ from(3.90), yields:

$$\varphi_{\mathbf{G}}(\mathbf{k},-\mathbf{r}) = \sum_L e^{i\mathbf{K}(-\mathbf{p}^\mu)} i^l Y_L^*(-\mathbf{R}^\mu\hat{\mathbf{K}}) Y_L(\hat{\mathbf{r}}) \{A u_l(r) + B \dot{u}_l(r)\} \tag{3.95}$$

Where it has been used, that $\mathbf{p}^{-\mu} = -\mathbf{p}^\mu$ and $\mathbf{R}^{-\mu} = -\mathbf{R}^\mu$, A and B abbreviates all terms in (3.90) that are real and do not depend on r or $\hat{\mathbf{r}}$. Using that $Y_L(\hat{\mathbf{r}}) = (-1)^l Y_L(-\hat{\mathbf{r}})$ (3.95)becomes:

$$\varphi_{\mathbf{G}}(\mathbf{k},-\mathbf{r}) = \sum_L e^{-i\mathbf{K}(\mathbf{p}^\mu)} (-i)^l Y_L^*(\mathbf{R}^\mu\hat{\mathbf{K}}) Y_L(\hat{\mathbf{r}}) \{A u_l(r) + B \dot{u}_l(r)\} \tag{3.96}$$

In the last step it can be exploited that $Y_{l-m}(\hat{\mathbf{r}}) = (-1)^m Y_{lm}^*(\hat{\mathbf{r}})$.Substituting $m' = -m$ (3.96) becomes:

$$\varphi_{\mathbf{G}}(\mathbf{k},-\mathbf{r}) = \sum_{lm'} e^{-i\mathbf{K}(\mathbf{p}^\mu)} (-i)^l Y_{lm'}^*(\mathbf{R}^\mu\hat{\mathbf{K}}) Y_{lm'}^*(\hat{\mathbf{r}}) \{A u_l(r) + B \dot{u}_l(r)\} \tag{3.97}$$

Hence, we have shown, that the FLAPW basis functions transform according to

$$\varphi_{\mathbf{G}}(\mathbf{k},-\mathbf{r}) = \varphi_{\mathbf{G}}^*(\mathbf{k},\mathbf{r}) \tag{3.98}$$

in the interstitial region and muffin-tins, if the system possesses inversion symmetry.

The Hamiltonian Matrix of Systems with Inversion Symmetry

The properties of the FLAPW basis function derived in the previous section leads to property of the Hamiltonian and overlap matrix. In systems that possess inversion symmetry these two matrices are real symmetric rather than complex hermitian. The Hamiltonian depends explicitly on $\mathbf{r}$ via the potential. The matrix elements are given by:

$$H^{\mathbf{G'G}}(\mathbf{k}) = \int \varphi^*_{\mathbf{G'}}(\mathbf{k},\mathbf{r})\mathcal{H}(\mathbf{r})\varphi_{\mathbf{G}}(\mathbf{k},\mathbf{r})d^3r \tag{3.99}$$

Substituting $\mathbf{r'} = -\mathbf{r}$ yield:

$$H^{\mathbf{G'G}}(\mathbf{k}) = \int \varphi_{\mathbf{G'}}(\mathbf{k},\mathbf{r'})\mathcal{H}(\mathbf{r'})\varphi^*_{\mathbf{G}}(\mathbf{k},\mathbf{r'})d^3r. \tag{3.100}$$

Where (3.98) and $\mathcal{H}(\mathbf{r}) = \mathcal{H}(-\mathbf{r})$ have been used. In addition the Hamiltonian operator is real, i.e. $\mathcal{H}(\mathbf{r}) = \mathcal{H}^*(\mathbf{r})$. Thus, we finally obtain:

$$\begin{aligned} H^{\mathbf{G'G}}(\mathbf{k}) &= \int \varphi_{\mathbf{G'}}(\mathbf{k},\mathbf{r'})\mathcal{H}^*(\mathbf{r'})\varphi^*_{\mathbf{G}}(\mathbf{k},\mathbf{r'})d^3r \\ &= \left(H^{\mathbf{G'G}}(\mathbf{k})\right)^*. \end{aligned} \tag{3.101}$$

Apparently, the same relation holds for the overlap matrix. The fact, that the two matrices are real means a great simplification in actual calculation. In principle, the diagonalization of a hermitian matrix is no more difficult than in the real case. However, one complex multiplication contains four real multiplication, and therefore the complex problem is far more "expensive" than the real one since the diagonalization needs the biggest part of the computer-time in each iteration.

3.2.5 Brillouin zone integration and Fermi energy

If density functional theory is applied to infinite periodic solids, quantities that are given by integrals of functions that depend on band and Bloch vector over the Brillouin zone have to determined. These integrations stretch only over the occupied part of the band, i.e over the region of the Brillouin zone where the band energy $\epsilon_\nu(\mathbf{k})$ (ν is the band index) is smaller than the Fermi energy. Hence, the integrals are of the form

$$\frac{1}{V_{BZ}} \int_{BZ} \sum_{\nu,\epsilon_\nu(\mathbf{k})<E_F} f_\nu(\mathbf{k})d^3k, \tag{3.102}$$

where f is the function to be integrated. Example of such quantities are the number of electrons per unit cell

$$N = \frac{1}{V_{BZ}} \int_{BZ} \sum_{\nu,\epsilon_\nu(\mathbf{k})<E_F} \mathbf{1}d^3k, \tag{3.103}$$

the electron (charge) density and the eigenvalue sum

$$\frac{1}{V_{BZ}} \int_{BZ} \sum_{\nu,\epsilon_\nu(\mathbf{k})<E_F} \epsilon_\nu(\mathbf{k})d^3k. \tag{3.104}$$

Numerically, these integrations are performed on discrete mesh in the Brillouin zone. In fact, only the irreducible part can be used to save computer time. There are different methods, that can be used to perform the integration, e.g. the special point method[ref] and tetrahedron method[ref]. The special points method is a method to integrate smoothly varying periodic functions of $\mathbf{k}$. The function to be integrated has to be calculated a set of special points in the (irreducible) Brillouin zone, each of which is assigned a weight. Thus, the Brillouin zone integration is transformed into a sum over a set of $\mathbf{k}$-points. However, these weights do not take into account, that the integration stretches only over the occupied part of the bands. This problem is solved by including only those bands into the summation that have an energy below the Fermi energy at the $\mathbf{k}$-point under consideration. Thus, the integrals become:

$$\frac{1}{V_{BZ}} \int_{BZ} \sum_{\nu,\epsilon_\nu(\mathbf{k})<E_F} f_\nu(\mathbf{k}) d^3k \longrightarrow \sum_{\mathbf{k}} \sum_{\nu,\epsilon_\nu(\mathbf{k})<E_F} f_\nu(\mathbf{k})\omega(\mathbf{k}) \tag{3.105}$$

Alternatively, this integration can be viewed as an integration over the whole Brillouin zone, where the function to be integrated is given by product of the function f with a step function that cuts out the region of Brillouin zone, where the band energy is above the Fermi energy. Clearly, the resulting function dose not satisfy the condition of being smoothly varying. Therefore, the special $\mathbf{k}$-points methods dose not converge very quickly, and rather many $\mathbf{k}$-points are needed to obtain accurate results. On the other hand this method is simple to implement, because the weights depend only on $\mathbf{k}$ and the band energy (via the step function) at each $\mathbf{k}$-point. Another problem arises from this "sharp" differentiation between occupied and empty bands (parts of bands). Let's consider a band that very close to Fermi energy at a certain $\mathbf{k}$-point. During the iterations the energy of this band might rise above or drop below the Fermi energy. This leads to sudden changes in the charge density, which can slow down or even prevent the convergence of density. These sudden changes are clearly a result of discretization in momentum space. To avoid this problem, the sharp edges of the step function have to removed. This can be done, e.g. by using the Fermi function $(e^{(\epsilon-E_F)/k_BT}+1)^{-1}$ rather than the step function. In other words, the function to be integrated is artificially made smoothly varying. The temperature T can then be adjusted to obtain the best convergence. This method is called temperature broadening.

In the current implementation of the FLAPW method the Fermi energy is determined in two steps. First the bands are occupied (at all $\mathbf{k}$-point simultaneously), starting from the lowest energy, until the sum of their weights equals the total number of electrons per unit cell, i.e. the discretized equivalent of (3.103) is solved at $T = 0$. Then the step function is replaced by the Fermi energy is determined from the requirement that:

$$N = \sum_{\mathbf{k}} \sum_{\nu} \omega(\mathbf{k}, \epsilon_\nu(\mathbf{k}) - E_F) \tag{3.106}$$

Where the weights are given by:

$$\omega(\mathbf{k}, \epsilon_\nu(\mathbf{k}) - E_F) = \omega(\mathbf{k}) \frac{1}{(e^{(\epsilon_\nu(\mathbf{k}) - E_F)/k_B T} + 1)} \tag{3.107}$$

The weights $\omega(\mathbf{k}, \epsilon_\nu(\mathbf{k}) - E_F)$ are stored to be used later for Brillouin zone integrations.

3.2.6 Representation of the density and the potential

The expansion of the charge density ρ and potential is very similar to expansion of the wavefunction. In the interstitial-region the two quantities are expanded into three-dimensional planewave, inside the muffin-tins they are represented by spherical harmonics and radial functions, which are store on an exponential mesh and in the vacuum they are expanded into two-dimensional planewave and z-depended functions, which are also given on an exponential mesh. The charge density is given by

$$\rho(\mathbf{r}) = \sum_i |\psi_i(\mathbf{r})|^2 \tag{3.108}$$

which contains terms of the form $e^{i(\mathbf{G}-\mathbf{G}')\mathbf{r}}$. Consequently, for a consistent representation the charge density planewave cut-off has to be twice the wavefunction cut-off G_{max}. In section (3.2.3) we explained, that the potential is also needed up to cut-off $2G_{max}$. This leads to large number of coefficients that need to be stored. Fortunately, this number can be reduced, if the symmetry of the system is exploited. Of course, the charge density and the potential posses the lattice symmetry. Therefore, the expansion into planewave is often more general than necessary. The planewave can be replaced by symmetrized planewaves, the so called star function. They are defined by :

$$\Phi_G^{3D}(\mathbf{r}) = \frac{1}{N_{op}} \sum_{op} e^{i\mathbf{R}\mathbf{G}(\mathbf{r}-\tau)} \tag{3.109}$$

where $\{\mathbf{R}|\tau\}$ are the symmetry operation of the lattice space group; if all the translation vectors τ are zero, the space group is cell symmorphic. By this construction all planewaves, that are symmetry equivalent, are combined to form one star. The two-dimensional stars $\Phi_s^{2D}(\mathbf{r})$ are defined in the same way, applying the operations of the two-dimensional space group only.

The same arguments can be applied to the expansion of the $\rho(V)$ inside the muffin-tin. In this case the relevant symmetry group is point group of the atom under consideration. Thus, different expansions are used at different atoms types, α, in the unit-cell. The symmetrized functions are called lattice harmonics and they are linear combinations of spherical harmonics

$$K_\nu(\hat{\mathbf{r}}) = \sum_m c_{\nu,m}^\alpha Y_L(\hat{\mathbf{r}}) \; . \tag{3.110}$$

The lattice harmonics are real, orthonormal and invariant under the point group operations. Finally, the expansion of the charge density has the form

$$\rho(\mathbf{r}) = \begin{cases} \sum_G \rho_G \Phi_G^{3D}(\mathbf{r}) & \mathbf{r} \in I \\ \sum_{G_{||}} \rho_{G_{||}}(z) \Phi_{G_{||}}^{2D}(\mathbf{r}) & \mathbf{r} \in \text{Vacuum} \\ \sum_G \rho_G^\alpha(r) K_\nu(\hat{\mathbf{r}}) & \mathbf{r} \in MT^\alpha \end{cases} \tag{3.111}$$

The potential is expanded in exactly the same way.

3.3 Construction of the electron density

In this section we will discuss the determination of the charge density from the eigenfunctions. In density functional calculations of an infinite periodic solid the electron density is given by an integral over the Brillouin zone

$$\rho(\mathbf{r}) = \frac{1}{V_{BZ}} \int_{BZ} \sum_{\nu, \epsilon_\nu(\mathbf{k}) < E_F} |\psi_\nu(\mathbf{k}, \mathbf{r})|^2 d^3k \tag{3.112}$$

where V_{BZ} is volume of the Brillouin zone, ν is the band index and E_F is the Fermi energy. In spin-polarized calculations the summation includes also the spin-index σ while in a non-magnetic calculation a factor of two has to be added to account for the spin-degeneracy. In the case of film calculations the three dimensional Brillouin zone is replaced by two-dimensional Brillouin zone. In both cases integration methods that sample eigenfunctions and eigenvalues on discrete k-points are used to compute the integrals. These methods transform the integration into a weighted sum over the k-points, where the choice of k-points and their weights depend on the integration method used. These weights depend not only on the k-point, but also on the energy of band, i.e. on the band (index), because each band contributes to the electron density only if its energy is below the Fermi energy.

$$\rho(\mathbf{r}) = \sum_{\mathbf{k}} \sum_{\nu} |\psi_\nu(\mathbf{k}, \mathbf{r})|^2 \omega(\nu, \mathbf{k}) \; . \tag{3.113}$$

Within the FLAPW method the eigenfunctions are represented in terms of the coefficients of the augmented planewaves

$$\psi_\nu(\mathbf{k}, \mathbf{r}) = \sum_{\mathbf{G}} c_\nu^{\mathbf{G}}(\mathbf{k}) \varphi_{\mathbf{G}}(\mathbf{k}, \mathbf{r}) \; . \tag{3.114}$$

Inside the muffin-tin spheres each planewave is coupled to sum of spherical harmonics and radial functions. Hence, in a sphere μ an eigenfunction is given by:

$$\psi_\nu^\mu(\mathbf{k}, \mathbf{r}) = \sum_{\mathbf{G}} c_\nu^{\mathbf{G}}(\mathbf{k}) \sum_L \left(A_L^{\mu\mathbf{G}}(\mathbf{k}) u_l^\alpha(r) + B_L^{\mu\mathbf{G}}(\mathbf{k}) \dot{u}_l^\alpha(r) \right) Y_L(\hat{\mathbf{r}}). \tag{3.115}$$

The $A_L^{\mu\mathbf{G}}(\mathbf{k})$ and $B_L^{\mu\mathbf{G}}(\mathbf{k})$ coefficients can be replaced by band dependent A- and B-coefficients, obtained by performing the contraction over the planewaves:

$$\psi_\nu^\mu(\mathbf{k},\mathbf{r}) = \sum_L \left(A_{L,\nu}^\mu(\mathbf{k}) u_l^\alpha(r) + B_{L,\nu}^\mu(\mathbf{k}) \dot{u}_l^\alpha(r) \right) Y_L(\hat{\mathbf{r}}) \tag{3.116}$$

where

$$A_{L,\nu}^\mu(\mathbf{k}) = \sum_{\mathbf{G}} c_\nu^{\mathbf{G}}(\mathbf{k}) A_L^\mu(\mathbf{k}), \quad B_{L,\nu}^{\mu\mathbf{G}}(\mathbf{k}) = \sum_{\mathbf{G}} c_\nu^{\mathbf{G}}(\mathbf{k}) B_L^{\mu\mathbf{G}}(\mathbf{k}). \tag{3.117}$$

3.3.1 "l-like" charge

Since the wavefunctions are expanded into spherical harmonics,Y_{lm} inside the muffin-tin spheres, they can be split up into contributions with a certain-l-character,

$$\psi_\nu^\mu(\mathbf{k},\mathbf{r}) = \sum_l \psi_{\nu,l}^\mu(\mathbf{k},\mathbf{r}) \tag{3.118}$$

The particle density of certain state depends on the square of wavefunction. Therefore, it contains cross-terms with a mixture of different l's:

$$\rho_\nu^\mu(\mathbf{r}) = \frac{1}{V_{BZ}} \int_{BZ} \left\{ \sum_l |\psi_{\nu,l}^\mu(\mathbf{k},\mathbf{r})|^2 + \sum_{l'l} 2 \left(\psi_{\nu,l'}^\mu(\mathbf{k},\mathbf{r}) \right)^* \psi_{\nu,l}^\mu(\mathbf{k},\mathbf{r}) \right\} d^3k \tag{3.119}$$

If, however, the density is integrated over the muffin-tin, the cross-terms vanish because of orthogonality of the spherical harmonics. Thus, the total electron density inside a sphere can be written as a sum over contributions with definite l-character:

$$n_\nu^\mu = \sum_l n_{\nu,l}^\mu, \quad n_{\nu,l}^\mu = \frac{1}{V_{BZ}} \int_{BZ} \int_{MT^\mu} |\psi_{\nu,l}^\mu(\mathbf{k},\mathbf{r})|^2 d^3r d^3k. \tag{3.120}$$

where $n_{\nu,l}^\mu$ is called l-like charge. We can also define a $\mathbf{k}$-dependent l-like charge by:

$$n_{\nu,l}^\mu(\mathbf{k}) = \int_{MT^\mu} |\psi_{\nu,l}^\mu(\mathbf{k},\mathbf{r})|^2 d^3r \tag{3.121}$$

Substituting (3.116)yields:

$$n_{\nu,l}^\mu(\mathbf{k}) = \sum_{m=-l}^{l} |A_{L,\nu}^\mu(\mathbf{k})|^2 + |B_{L,\nu}^\mu(\mathbf{k})|^2 \dot{N}_l^\alpha \tag{3.122}$$

where

$$\dot{N}_l^\alpha = \int_0^{R_{MT^\alpha}} (\dot{u}_l^\alpha(r))^2 r^2 dr \tag{3.123}$$

and the orthogonality of the spherical harmonics, the normalization of u_l^α and the orthogonality of u_l^α and $\dot{u}_l^\alpha$ have been used.

3.3.2 Determination of the optimal energy parameter

In order to minimize the linearization error, the energy parameters should be chosen as close to the band energies as possible. However, the band energies $\epsilon_\nu(\mathbf{k})$ depend on $\mathbf{k}$ whereas the energy parameters E_l^α are constants. In addition, the radial functions contribute to the eigenfunctions of different band with different energies. Therefore, deviations between $\epsilon_\nu(\mathbf{k})$ and E_l^α have to be minimized. An optimal choice can be obtained from the requirement, that the energy parameters minimize

$$\int_{BZ} \sum_{\nu,\epsilon_\nu(\mathbf{k})<E_F} \left(\epsilon_\nu(\mathbf{k}) - E_l^\alpha\right)^2 \rho_{\nu,l}^\mu(\mathbf{k}) d^3k \tag{3.124}$$

which is the quadratic error weighted with the amount of charge that each band contributes to the l-like charge with the l-character of the energy parameter. Setting the derivative $(\partial/\partial E_l^\alpha)$ equal to zero yields the optimal energy parameter:

$$E_l^\alpha = \left(\int_{BZ} \sum_{\nu,\epsilon_\nu(\mathbf{k})<E_F} \epsilon_\nu(\mathbf{k}) \rho_{\nu,l}^\mu(\mathbf{k}) d^3k\right) \Bigg/ \left(\int_{BZ} \sum_{\nu,\epsilon_\nu(\mathbf{k})<E_F} \rho_{\nu,l}^\mu(\mathbf{k}) d^3k\right). \tag{3.125}$$

The Brillouin zone integration methods transform this into sum over a discrete $\mathbf{k}$-point set

$$E_l^\alpha = \left(\sum_{\mathbf{k}} \sum_{\nu} \epsilon_\nu(\mathbf{k}) \rho_{\nu,l}^\mu \omega(\nu,\mathbf{k})\right) \Bigg/ \left(\sum_{\mathbf{k}} \sum_{\nu} \rho_{\nu,l}^\mu(\mathbf{k}) \omega(\nu,\mathbf{k})\right). \tag{3.126}$$

Of course, the band energies, are not known in advance, therefore values last iteration have to be used.

3.3.3 Construction of the electron density in the muffin-tins

Substituting (3.116) into (3.112) yields the electron density in the muffin-tin spheres:

$$\begin{aligned}\rho^\mu(\mathbf{r}) = \frac{1}{V_{BZ}} \int_{BZ} \sum_{\nu,\epsilon_\nu(\mathbf{k})<E_F} \sum_{L'} \left(A_{L',\nu}^\mu(\mathbf{k}) u_{l'}^\alpha(r) + B_{L',\nu}^\mu(\mathbf{k}) \dot{u}_{l'}^\alpha(r)\right)^* Y_{L'}^*(\hat{\mathbf{r}}) \\ \sum_L \left(A_{L,\nu}^\mu(\mathbf{k}) u_l^\alpha(r) + B_{L,\nu}^\mu(\mathbf{k}) \dot{u}_l^\alpha(r)\right) Y_L(\hat{\mathbf{r}}) d^3k.\end{aligned} \tag{3.127}$$

The particle density inside the muffin-tins is also expanded into spherical harmonics.

$$\rho^\mu(\mathbf{r}) = \sum_L C_L^\mu(r) Y_L(\hat{\mathbf{r}}) \tag{3.128}$$

The coefficients $C_{L''}^\mu(r)$ can be determined by multiplying (**??**) with $\int Y_{L''}(\hat{\mathbf{r}})$ and integration over the sphere

$$C^{\mu}_{L''}(r) = \frac{1}{V_{BZ}} \int_{BZ} \sum_{\nu,\epsilon_\nu(\mathbf{k})<E_F} \sum_{L'} \left(A^{\mu}_{L',\nu}(\mathbf{k}) u^{\alpha}_{l'}(r) + B^{\mu}_{L',\nu}(\mathbf{k}) \dot{u}^{\alpha}_{l'}(r)\right)^* \sum_{L} \left(A^{\mu}_{L,\nu}(\mathbf{k}) u^{\alpha}_{l}(r) + B^{\mu}_{L,\nu}(\mathbf{k}) \dot{u}^{\alpha}_{l}(r)\right) G^{mm'm''}_{ll'l''} d^3k \tag{3.129}$$

with Gaunt coefficients

$$G^{mm'm''}_{ll'l''} = \int Y^*_{l,m} Y_{l',m'} Y_{l'',m''} d\Omega \tag{3.130}$$

where it has been used, that the Gaunt coefficients are real, i.e.

$$\int Y_{l,m} Y^*_{l',m'} Y^*_{l'',m''} d\Omega = \int Y^*_{l,m} Y_{l',m'} Y_{l'',m''} d\Omega \; . \tag{3.131}$$

Finally, applying a Brillouin zone integration method yields:

$$\begin{aligned} C^{\mu}_{L''}(r) \; &= \sum_{ll'} \left(\sum_{\mathbf{k}} \sum_{\nu} \sum_{mm'} \left(A^{\mu}_{L',\nu}(\mathbf{k})\right)^* A^{\mu}_{L,\nu}(\mathbf{k}) G^{mm'm''}_{ll'l''} \omega(\nu,\mathbf{k}) \right) u^{\alpha}_{l'}(r) u^{\alpha}_{l}(r) \\ &+ \sum_{ll'} \left(\sum_{\mathbf{k}} \sum_{\nu} \sum_{mm'} \left(A^{\mu}_{L',\nu}(\mathbf{k})\right)^* B^{\mu}_{L,\nu}(\mathbf{k}) G^{mm'm''}_{ll'l''} \omega(\nu,\mathbf{k}) \right) u^{\alpha}_{l'}(r) \dot{u}^{\alpha}_{l}(r) \\ &+ \sum_{ll'} \left(\sum_{\mathbf{k}} \sum_{\nu} \sum_{mm'} \left(B^{\mu}_{L',\nu}(\mathbf{k})\right)^* A^{\mu}_{L,\nu}(\mathbf{k}) G^{mm'm''}_{ll'l''} \omega(\nu,\mathbf{k}) \right) \dot{u}^{\alpha}_{l'}(r) u^{\alpha}_{l}(r) \\ &+ \sum_{ll'} \left(\sum_{\mathbf{k}} \sum_{\nu} \sum_{mm'} \left(B^{\mu}_{L',\nu}(\mathbf{k})\right)^* B^{\mu}_{L,\nu}(\mathbf{k}) G^{mm'm''}_{ll'l''} \omega(\nu,\mathbf{k}) \right) \dot{u}^{\alpha}_{l'}(r) \dot{u}^{\alpha}_{l}(r) \; . \end{aligned} \tag{3.132}$$

3.3.4 Construction of the electron density in the interstitial region

In the interstitial region the wavefunctions are represented in the following form.

$$\psi_\nu(\mathbf{k},\mathbf{r}) = \sum_{\mathbf{G}} c^{\mathbf{G}}_{\nu}(\mathbf{k}) e^{i(\mathbf{G}+\mathbf{k})\mathbf{r}}. \tag{3.133}$$

Starting form (4.1) the electron density is given by:

$$\rho(\mathbf{r}) = \frac{1}{V_{BZ}} \int_{BZ} \sum_{\nu,\epsilon_\nu(\mathbf{k})<E_F} \sum_{\mathbf{G'}\mathbf{G''}} \left(c^{\mathbf{G'}}_{\nu}(\mathbf{k})\right)^* c^{\mathbf{G''}}_{\nu}(\mathbf{k}) d^3k e^{i(\mathbf{G''}-\mathbf{G'})\mathbf{r}} \; . \tag{3.134}$$

The electron density in the interstitial region is also expanded into planewaves

$$\rho(\mathbf{r}) = \sum_{\mathbf{G}} n^{\mathbf{G}} e^{i\mathbf{G}\mathbf{r}} \; , \tag{3.135}$$

hence, the planewave coefficients of the electron density are:

$$\rho^{\mathbf{G}} = \frac{1}{V_{BZ}} \int_{BZ} \sum_{\nu,\epsilon_\nu(\mathbf{k})<E_F} \sum_{\substack{\mathbf{G}'\mathbf{G}'' \\ \mathbf{G}''-\mathbf{G}'=\mathbf{G}}} \left(c_\nu^{\mathbf{G}}(\mathbf{k})\right)^* c_\nu^{\mathbf{G}''}(\mathbf{k}) d^3k \; . \tag{3.136}$$

Apparently, the planewave cut-off of the particle density has to be twice the cut-off of the wavefunction expansion (G_{max}) to allow an accurate description. The $\mathbf{k}$ and state dependent density

$$\rho_\nu^{\mathbf{G}}(\mathbf{k}) = \sum_{\substack{\mathbf{G}'\mathbf{G}'' \\ \mathbf{G}''-\mathbf{G}'=\mathbf{G}}} \left(c_\nu^{\mathbf{G}'}(\mathbf{k})\right)^* c_\nu^{\mathbf{G}''}(\mathbf{k}) = \sum_{\mathbf{G}'} \left(c_\nu^{\mathbf{G}'}(\mathbf{k})\right)^* c_\nu^{(\mathbf{G}+\mathbf{G}')}(\mathbf{k}) \tag{3.137}$$

is given by a convolution in momentum space. For each coefficient a sum over $\mathbf{G}$ has to be performed. Consequently, the numerical effort put into the determination of $n_\nu^{\mathbf{G}}(\mathbf{k})$ scales proportional to the number of G-vectors squared, i.e. proportional to $(G_{max})^6$. However, $n_\nu^{\mathbf{G}}(\mathbf{k})$ can be calculated more efficiently using the fast Fourier transform (FFT). First, $c_\nu^{\mathbf{G}}(\mathbf{k})$ is Fourier transformed to real space, where it is squared on a real space mesh yielding $n_\nu(\mathbf{k},\mathbf{r})$, then all states are summed up and finally the resulting particle density is back-transformed to momentum space.

$$c_\nu^{\mathbf{G}}(\mathbf{k}) \xrightarrow{\text{FFT}} \psi_\nu(\mathbf{k},\mathbf{r}) \xrightarrow{\text{square}} n_\nu(\mathbf{k},\mathbf{r}) \xrightarrow{\sum_\nu} \rho(\mathbf{k},\mathbf{r}) \xrightarrow{\text{FFT}^{-1}} \rho^{\mathbf{G}}(\mathbf{k})$$

With this scheme the numerical effort increases proportional to $(G_{max})^3 ln((G_{max})^3)$, which is a major improvement for large systems. In a last step the planewaves have to be combined to form the three-dimensional stars.

3.3.5 Construction of the electron density in the vacuum region

In the vacuum region the wavefunctions are expanded into two-dimensional planewaves parallel to the surface and z-dependent functions perpendicular to the surface

$$\psi_\nu(\mathbf{k}_{||},\mathbf{r}) = \sum_{\mathbf{G}_{||}G_\perp} c_\nu^{\mathbf{G}_{||}G_\perp}(\mathbf{k}_{||}) \left(A_{\mathbf{G}_{||}G_\perp}(\mathbf{k}_{||}) u_{\mathbf{G}_{||}}(\mathbf{k}_{||},z) + B_{\mathbf{G}_{||}G_\perp}(\mathbf{k}_{||}) \dot{u}_{\mathbf{G}_{||}}(\mathbf{k}_{||},z)\right) e^{i(\mathbf{G}_{||}+\mathbf{k}_{||})\mathbf{r}_{||}} \; , \tag{3.138}$$

Hence, the electron density is given by

$$\begin{aligned} \rho(\mathbf{r}) = \; & \frac{1}{V_{BZ}} \int_{BZ} \sum_{\nu,\epsilon_\nu(\mathbf{k})<E_F} \sum_{\mathbf{G}'_{||}G'_\perp} \sum_{\mathbf{G}''_{||}G''_\perp} e^{i(\mathbf{G}''_{||}-\mathbf{G}'_{||})\mathbf{r}_{||}} \\ & \left(c_\nu^{\mathbf{G}'_{||}G'_\perp}(\mathbf{k}_{||}) \left(A_{\mathbf{G}'_{||}G'_\perp}(\mathbf{k}_{||}) u_{\mathbf{G}'_{||}}(\mathbf{k}_{||},z) + B_{\mathbf{G}'_{||}G'_\perp}(\mathbf{k}_{||}) \dot{u}_{\mathbf{G}'_{||}}(\mathbf{k}_{||},z) \right) \right)^* \\ & \left(c_\nu^{\mathbf{G}''_{||}G''_\perp}(\mathbf{k}_{||}) \left(A_{\mathbf{G}''_{||}G''_\perp}(\mathbf{k}_{||}) u_{\mathbf{G}''_{||}}(\mathbf{k}_{||},z) + B_{\mathbf{G}''_{||}G''_\perp}(\mathbf{k}_{||}) \dot{u}_{\mathbf{G}''_{||}}(\mathbf{k}_{||},z) \right) \right) d^3k \; . \end{aligned} \tag{3.139}$$

The particle density in the vacuum is represented in the following form.

$$\rho(\mathbf{r}) = \sum_{\mathbf{G}_{||}} n^{\mathbf{G}_{||}}(z) e^{i\mathbf{G}_{||}\mathbf{r}_{||}} \ , \tag{3.140}$$

Performing the Brillouin zone integration on a discrete $\mathbf{k}_{||}$-mesh and carrying out the summation over $\mathbf{G'}_{\perp}$ and $\mathbf{G''}_{\perp}$ we find that the coefficients $n^{\mathbf{G}_{||}}(z)$ are :

$$\begin{aligned}
\rho^{\mathbf{G}_{||}}(z) \ = & \sum_{\mathbf{k}_{||}} \sum_{\nu} \sum_{\mathbf{G'}_{||}} \left(A_{\mathbf{G'}_{||},\nu}(\mathbf{k}_{||}) \right)^* A_{(\mathbf{G}_{||}+\mathbf{G'}_{||}),\nu}(\mathbf{k}_{||}) \omega(\nu,\mathbf{k}_{||}) u_{\mathbf{G'}_{||}}(\mathbf{k}_{||},z) u_{(\mathbf{G}_{||}+\mathbf{G'}_{||})}(\mathbf{k}_{||},z) \\
& + \sum_{\mathbf{k}_{||}} \sum_{\nu} \sum_{\mathbf{G'}_{||}} \left(A_{\mathbf{G'}_{||},\nu}(\mathbf{k}_{||}) \right)^* B_{(\mathbf{G}_{||}+\mathbf{G'}_{||}),\nu}(\mathbf{k}_{||}) \omega(\nu,\mathbf{k}_{||}) u_{\mathbf{G'}_{||}}(\mathbf{k}_{||},z) \dot{u}_{(\mathbf{G}_{||}+\mathbf{G'}_{||})}(\mathbf{k}_{||},z) \\
& + \sum_{\mathbf{k}_{||}} \sum_{\nu} \sum_{\mathbf{G'}_{||}} \left(B_{\mathbf{G'}_{||},\nu}(\mathbf{k}_{||}) \right)^* A_{(\mathbf{G}_{||}+\mathbf{G'}_{||}),\nu}(\mathbf{k}_{||}) \omega(\nu,\mathbf{k}_{||}) \dot{u}_{\mathbf{G'}_{||}}(\mathbf{k}_{||},z) u_{(\mathbf{G}_{||}+\mathbf{G'}_{||})}(\mathbf{k}_{||},z) \\
& + \sum_{\mathbf{k}_{||}} \sum_{\nu} \sum_{\mathbf{G'}_{||}} \left(B_{\mathbf{G'}_{||},\nu}(\mathbf{k}_{||}) \right)^* B_{(\mathbf{G}_{||}+\mathbf{G'}_{||}),\nu}(\mathbf{k}_{||}) \omega(\nu,\mathbf{k}_{||}) \dot{u}_{\mathbf{G'}_{||}}(\mathbf{k}_{||},z) \dot{u}_{(\mathbf{G}_{||}+\mathbf{G'}_{||})}(\mathbf{k}_{||},z)
\end{aligned} \tag{3.141}$$

with

$$A_{\mathbf{G}_{||},\nu}(\mathbf{k}_{||}) = \sum_{G_{\perp}} c_{\nu}^{\mathbf{G}_{||}G_{\perp}}(\mathbf{k}_{||}) A_{\mathbf{G}_{||}G_{\perp}}(\mathbf{k}_{||}), \quad B_{\mathbf{G}_{||},\nu}(\mathbf{k}_{||}) = \sum_{G_{\perp}} c_{\nu}^{\mathbf{G}_{||}G_{\perp}}(\mathbf{k}_{||}) B_{\mathbf{G}_{||}G_{\perp}}(\mathbf{k}_{||}) \ . \tag{3.142}$$

Here, the terms of the form

$$\sum_{\mathbf{G'}_{||}} \left(A_{\mathbf{G'}_{||},\nu}(\mathbf{k}_{||}) \right)^* A_{(\mathbf{G}_{||}+\mathbf{G'}_{||}),\nu}(\mathbf{k}_{||}) u_{\mathbf{G'}_{||}}(\mathbf{k}_{||},z) u_{(\mathbf{G}_{||}+\mathbf{G'}_{||})}(\mathbf{k}_{||},z)$$

represent convolutions in momentum space. Similar to the interstitial region these terms could be calculated more efficiently, using two-dimensional fast Fourier transform. However, there are far less two-dimensional planewaves than three-dimensional planewaves. Therefore, the possible saving of computer time is much smaller.

3.4 Construction of the Coulomb potential

The Coulomb potential consists of two parts, the Hartree term $V_H(\mathbf{r})$ and the external potential of the nuclei $V_i(\mathbf{r})$

$$V_c(\mathbf{r}) = V_H(\mathbf{r}) + V_i(\mathbf{r}) \ . \tag{3.143}$$

The Hartree potential has to be determined from the charge density via the Poisson equation

$$\Delta V_H(\mathbf{r}) = 4\pi\rho(\mathbf{r}) \ . \tag{3.144}$$

In real space the solution of (3.169) is given by

$$V_H(\mathbf{r}) = \int \frac{4\pi\rho(\mathbf{r}')}{|\mathbf{r}-\mathbf{r}'|} d^3\mathbf{r} \; . \tag{3.145}$$

In reciprocal space, however, the Poisson equation is diagonal, as a result the solution is very simple

$$V_H(\mathbf{G}) = \frac{4\pi\rho(\mathbf{G})}{\mathbf{G^2}} \; . \tag{3.146}$$

Therefore, and because of the representation of the charge density and the potential in the interstitial- and vacuum-region, the solution of the Poisson equation in reciprocal space appears to the convenient. However, due to rather localized core and valence states the charge density changes on a very small length scale near the nuclei. Therefore, the planewave expansion of ρ convergences slowly, and a direct use of (3.146) is impractical, if not impossible. This difficulty can be circumvented via the pseudocharge method.

3.5 The pseudocharge method

The pseudocharge method, developed by Weinert [64], is a very elegant technique to calculate the interstitial and vacuum Hartree potential. The underlying idea is to divide the solution of the Poisson equation into two steps. In the fist step the true muffin-tin charge is replaced by a convergent (in terms of planewaves) pseudocharge density $\tilde{\rho}$, that leads to the same potential outside the muffin-tins(i.e. it has the same multipole moments). Then the interstitial (and vacuum) potential is calculated in reciprocal space. In the second step the muffin-tin potential is determined from the Dirichlet boundary value problem, defined by the exact muffin-tin charge and the interstitial potential on the muffin-tin spheres due to a charge distribution inside the sphere is determined completely by its multipole moments q_L:

$$V(\mathbf{r}) = \sum_{l=0}^{\infty} \sum_{m=-l}^{l} \frac{4\pi}{2l+1} \frac{q_L}{r^{l+1}} Y_L(\hat{\mathbf{r}}). \tag{3.147}$$

However, the multipole moments do not define the charge density uniquely. The charge density is given by:

$$\rho(\mathbf{r}) = \rho_I(\mathbf{r})\Theta(\mathbf{r} \in I) + \sum_{\alpha} \rho_\alpha(\mathbf{r})\Theta(\mathbf{r} \in MT^\alpha) \tag{3.148}$$

Of course, in film calculation there is also a vacuum charge, and we will come back to this later. (3.147) can be re written

$$\rho(\mathbf{r}) = \rho_I(\mathbf{r}) + \sum_{\alpha} [\rho_\alpha(\mathbf{r}) - \rho_I(\mathbf{r})]\Theta(\mathbf{r} \in MT^\alpha) \tag{3.149}$$

Thus, the interstitial charge has been extended into the muffin-tin and subtracted there again. The second term in (3.149) can now be replaced by a pseudocharge $\tilde{\rho}^{\alpha}$, that has the same multipole moments(s. [64] for detail). The resultant pseudocharge $\tilde{\rho}$ is given by:

$$\tilde{\rho}(\mathbf{r}) = \rho_I(\mathbf{r}) + \sum_{\alpha} \tilde{q}^{\alpha}(\mathbf{r}) \tag{3.150}$$

$\tilde{\rho}(\mathbf{r})$ is constructed to have a more rapidly converging Fourier expansion than the original charge density $\rho(\mathbf{r})$. Therefore, the Poisson equation can now be solved using (3.146).

Still, the muffin-tin potential V_{MT}^{α} remains to be determined. For this step the exact muffin-tin charge ρ_{α} has to be used. Since, the interstitial potential is already known at this point, the calculation of V_{MT}^{α} constitutes a classical spherically symmetric Diriclet boundary value problem, which can be solved by the Green's function method [65].

$$V_{MT}^{\alpha}(\mathbf{r}) = \int_{MT_{\alpha}} \rho(\mathbf{r}')G(\mathbf{r},\mathbf{r}')d^3r' - \frac{R_{\alpha}^2}{4\pi}\oint_{S^{\alpha}} V_I(\mathbf{r}')\frac{\partial G}{\partial n'}d\Omega' \tag{3.151}$$

The second integral is over the muffin-tin sphere boundary S^{α}, and it is necessary to satisfy the boundary conditions. The Green's function is given by:

$$G^{\alpha}(\mathbf{r},\mathbf{r}') = 4\pi\sum_{l,m}\frac{Y_L(\hat{\mathbf{r}'})Y_L(\hat{\mathbf{r}})}{2l+1}\frac{r_<^l}{r_>^{l+1}}\big(1-\big(\frac{r_>}{R_{MT^{\alpha}}}\big)^{2l+1}\big) = \tag{3.152}$$

where $r_> = max\{|\mathbf{r}'|,|\mathbf{r}|\}, r <= min\{|\mathbf{r}'|,|\mathbf{r}|\}$. Finally, the muffin-tin potential has to be expanded into lattice harmonics $K_{\nu}(\hat{\mathbf{r}})$.

$$V_{MT}^{\alpha}(\mathbf{r}) = \sum_{\nu} V_{MT,\nu}^{\alpha}(r)K_{\nu}(\hat{\mathbf{r}})\ . \tag{3.153}$$

The potential of the nuclei $V_i^{\alpha}(r) = \frac{ez_{\alpha}}{|r|}$ is added to the spherical $(l=0)$ component of the potential $V_{MT,0}^{\alpha}(\mathbf{r})$.

The muffin-tin potential is commuted in the same way for both, bulk and film calculations. Apparently, the interstitial and the vacuum have to be treated differently is the two cases, due to the different boundary conditions and the different representation of the vacuum potential. Therefore, the next two sections the solution of the Poisson equation will be outlined separately for these cases.

3.5.1 Determination of the interstitial Coulomb potential in bulk calculation

In the case of the bulk calculation we have periodic boundary conditions in three dimensions. Therefore, the solution of the Poisson equation,

$$\mathbf{G}^2V(\mathbf{G}) = 4\pi\tilde{\rho}(\mathbf{G}) \tag{3.154}$$

is very simple. Obviously this equation can only be solved, if $\tilde{\rho}(\mathbf{0}) = 0$. Since $\tilde{\rho}(\mathbf{0})$ is the average charge density, this means, that charge neutrality is essential. Still, $V(0)$ remains undetermined by (3.149), i.e. one has the freedom to shift the potential by a constant. This is a consequence of the periodic boundary conditions, because they do not fix the reference of the potential. Usually $V(0)$ is chosen to be zero, hence the Coulomb potential in the interstitial-region is given by:

$$V_I(\mathbf{r}) = \sum_{\mathbf{G}\neq 0} \frac{4\pi\tilde{\rho}(\mathbf{G})}{\mathbf{G}^2} e^{i\mathbf{G}\mathbf{r}} = \sum_{s\neq 0} \frac{4\pi\tilde{\rho}_s}{\mathbf{G_s^2}} \Phi_s^{3D}(\mathbf{r}) \tag{3.155}$$

where the first summation is expressed in terms of G-vectors and the second in terms of stars.

3.5.2 Determination of the interstitial and vacuum Coulomb potential in film calculations

In a film the translational symmetry in z-direction is lost. Accordingly, the boundary conditions are periodic in two dimensions only. In z-direction the periodic boundary conditions are replaced by the requirement, that the potential on one side of the film (at least) approaches zero at infinity (and also derivative=0, on both side). The latter condition defines the absolute reference of the potential. As a consequence of the symmetry breaking, the following expansion of V and ρ is most suitable to solve the Poisson equation:

$$V(\mathbf{r}) = V_0(z) + \sum_{\mathbf{G}_\parallel\neq\mathbf{0}} V_{\mathbf{G}_\parallel}(z) e^{i\mathbf{G}_\parallel\mathbf{r}} \tag{3.156}$$

$$\rho(\mathbf{r}) = \rho_0(z) + \sum_{\mathbf{G}_\parallel\neq\mathbf{0}} \rho_{\mathbf{G}_\parallel}(z) e^{i\mathbf{G}_\parallel\mathbf{r}} \,. \tag{3.157}$$

Substituting this into the Poisson equations yields:

$$\left(\frac{d^2}{dz^2} - G_\parallel^2\right) V_{G_\parallel}(z) = -4\pi\rho_{G_\parallel}(z) \tag{3.158}$$

This equation is treated differently for $G_\parallel = 0$ and $G_\parallel \neq 0$.

The $G_\parallel = 0$ component of the potential

For the $G_\parallel = 0$ component of the potential the Poisson equation has the form

$$\frac{d^2}{dz^2} V_0(z) = -4\pi\rho_0(z) \tag{3.159}$$

The $G_\parallel = 0$ component of the pseudocharge density is given by:

$$\rho_0(z) = \begin{cases} \rho_I^{0,0} + \sum_{G_\perp} \rho_I^{0,G_\perp} e^{iG_\perp z} & |z| \leq \frac{D}{2} \\ \rho_V^0(z) & |z| > \frac{D}{2} \,. \end{cases} \tag{3.160}$$

The Poisson equation for the $G_\parallel = 0$ can be integrated directly. The result in the vacuum region is given by:

$$V_V^0(z) = -4\pi \int_z^\infty \sigma_V(z')dz' + \left(\frac{\partial}{\partial z} V_V^0(z) \Big|_{z=\infty} \right) z, \tag{3.161}$$

$(\frac{\partial}{\partial z}) V_V^0(z)|_{z=\infty} = -E_{ext}$ which is assumed to be zero for the moment then,

$$\sigma_V(z) = \int_{\frac{D}{2}}^z \rho_V^0(z')dz' + \bar{\rho}_I \frac{D}{2} \,, \quad \left(\frac{\partial}{\partial z} V_V^0(z) \Big|_{z=\infty} \right) = 0 \,, \tag{3.162}$$

where the average interstitial charge density $\bar{\rho}_I$ is given by:

$$\bar{\rho}_I = \sum_{G_\perp} \rho_I^{0,G_\perp} j_0(G_\perp^n D). \tag{3.163}$$

Here $\bar{\rho}_I$ does not equal $\rho_I^{0,0}$, because the $G_\perp$ are defined in terms of $\tilde{D}$ rather than D, i.e. the period of the z-dependent planewaves does not equal the integration interval.

In the interstitial region the solution to is (3.154) is

$$V_I^0(z) = -2\pi\rho_I^{0,0}\big(z^2 - \frac{D^2}{4}\big) - 4\pi \sum_{G_\perp} \frac{\rho_I^{0,G_\perp}}{G_\perp^2} \big(e^{iG_\perp z} - e^{iG_\perp \frac{D}{2}}\big) - 4\pi \int_{\frac{D}{2}}^\infty \sigma_V(z')dz' \,. \tag{3.164}$$

The $G_\parallel \neq 0$ component of the potential

In the case $G_\parallel \neq 0$ the Poisson equation is solved via the Green's function method.

$$V_{G_\parallel}(z) = \int_{-\infty}^\infty \rho_{G_\parallel} G_{G_\parallel}(z - z')dz' \tag{3.165}$$

where the Green's function is given by:

$$G_{G_\parallel}(z - z') = \frac{2\pi}{G_\parallel} e^{|G_\parallel||z-z'|} \,. \tag{3.166}$$

This leads to the following solution in the vacuum-region

$$\begin{aligned} V_V^{G_\parallel}(z) \;=\; & \frac{2\pi}{G_\parallel} e^{G_\parallel z} \int_{-\infty}^z \rho_V^{G_\parallel}(z') e^{-G_\parallel z'} dz' \\ & + \frac{2\pi}{G_\parallel} e^{-G_\parallel z} \int_z^{-\frac{D}{2}} \rho_V^{G_\parallel}(z') e^{-G_\parallel z'} dz' \\ & + \frac{2\pi}{G_\parallel} e^{G_\parallel z} \sum_{G_\perp} \frac{\rho_I^{G_\parallel, G_\perp}}{G_\parallel + iG_\perp} \big(e^{(G_\parallel + iG_\perp)z} - e^{-(G_\parallel + iG_\perp)z}\big) \end{aligned} \tag{3.167}$$

and in the interstitial-region

$$
\begin{aligned}
V_I^{G_\parallel}(z) &= 4\pi \sum_n \frac{\rho_I^{G_\parallel, G_\perp}}{G^2} e^{iG_\perp z} \\
&+ \frac{2\pi}{G_\parallel} \sum_{G_\perp} \frac{\rho_I^{G_\parallel, G_\perp}}{G^2} \Big[e^{G_\parallel z}(G_\parallel + iG_\perp) e^{-(G_\parallel - iG_\perp)\frac{D}{2}} \\
&+ e^{-G_\parallel z}(G_\parallel - iG_\perp) e^{-(G_\parallel + iG_\perp)\frac{D}{2}} \Big] \\
&+ \frac{2\pi}{G_\parallel} \left[e^{G_\parallel z} \int_{\frac{-D}{2}}^{\infty} \rho_V^{G_\parallel}(z') e^{-G_\parallel z'} dz' + e^{-G_\parallel z} \int_{-\infty}^{\frac{D}{2}} \rho_V^{G_\parallel}(z') e^{-G_\parallel z'} dz' \right] .
\end{aligned}
\tag{3.168}
$$

3.5.3 External electric field

Including external electric fields in a standard electronic structure calculation is problematic since the resulting potential is not periodic. Within the film geometry of the FLAPW method, however, the external electric fields can be included straightforwardly [66–68].

In the last section, Poisson's equation have been solved for determining the Coulomb potential of the film. Because of the linearity of Poisson's equation, we are free to pick these boundary conditions in any convenient manner. One choice to include the electric field is to set $(\frac{\partial}{\partial z})V_V^0(z)|_{z=\infty} = -E$ in Eq. (3.161); in this case, no ρ_{ext} is required to describe the field. Likewise, one can apply two-point boundary conditions, giving the potential at opposite sides of a film. These choices are useful when, for instance, specifying the potential drop across a film.

Another choice, with a different physical interpretation, is to require

$$V(\infty) = 0 \,, \tag{3.169}$$

$$\frac{\partial}{\partial z} V(\infty) = 0 \,, \tag{3.170}$$

consistent with the boundary conditions for the zero-field case, and requires an external charge distribution ρ_{ext} to describe the field. To represent the uniform electric field, elementary electrostatics gives that a planar sheet of charge with surface density $\sigma = q/A$ (q is the total charge and A is the area of the surface unit-cell) will generate a normal field $E = 4\pi\sigma\hat{\mathbf{n}}$. Finally this external charge distribution ρ_{ext} can be added to Eq (3.162):

$$\sigma_V(z) = \int_{\frac{D}{2}}^{z} \rho_V^0(z')dz' + \bar{\rho}_I \frac{D}{2} + \int_{\frac{D}{2}}^{z} \rho_{ext}(z')dz' \tag{3.171}$$

Thus, to include the external field, we can place a sheet of charge 'far enough' outside the surface so that the electrons have negligible overlap with the sheet; this distance is typically 2-10 a.u from the last row of atoms for metals.

3.5.4 Computation of the exchange correlation potential

The problem of the determination of the exchange correlation potential is handled differently from the Coulomb potential. On one hand, V_{xc}^{σ} is a local quantity, i.e. $V_{xc}^{\sigma}(\mathbf{r})$ depends only $n_{\uparrow}(\mathbf{r})$ and $n_{\downarrow}(\mathbf{r})$ at the same position $\mathbf{r}$. Thus, the muffin-tins, the interstitial-and vacuum-region can be treated independently. On the other hand, V_{xc}^{σ} and ϵ_{xc}^{σ} are non-linearfunctions of $n_{\uparrow}$ and $n_{\downarrow}$. Therefore, V_{xc}^{σ} and ϵ_{xc}^{σ} have to be calculated in real space. V_{xc}^{σ} and ϵ_{xc}^{σ} are determined in the same way. First, $n_{\uparrow}$ and $n_{\downarrow}$ are transformed to real space, where V_{xc}^{σ} and ϵ_{xc}^{σ} are calculated. Then V_{xc}^{σ} and ϵ_{xc}^{σ} are back-transformed. Then, V_{xc}^{σ} is added to the Coulomb potential, yielding the spin-dependent potential $V_{\uparrow}$ and $V_{\downarrow}$. ϵ_{xc}^{σ} is needed for the determination of the total energy.

3.5.5 Calculation of ϵ_{xc}^{σ} and V_{xc}^{σ} in the interstitial-region

In the interstitial-region the charge density is expanded into three-dimensional stars with coefficient n_s^{σ}. Multiplying these by $e^{i\mathbf{R}\mathbf{G}\tau}$ yields the planewave coefficients n_G^{σ}. If the space group is symmorphic, the star and planewave coefficients are identical. However, due to numerical inaccuracy, the calculated coefficients of symmetry equivalent planewaves are not exactly equal, and the corresponding star coefficient is obtained from the average of the planewave coefficients. In the nest step a three dimensional fast-Fourier transform is carried out. Then the exchange correlation potential is calculated on a real space mesh r_i. Finally, V_{xc}^{σ} is back-transformed, and the star coefficients are computed.

$$\rho_s^{\sigma} \;\rightarrow\; \rho_G^{\sigma} \;\xrightarrow{\text{FFT}}\; \rho^{\sigma}(\mathbf{r}) \;\rightarrow\; V_{xc}^{\sigma}(\mathbf{r}) \;\xrightarrow{\text{FFT}^{-1}}\; V_{xc}^{\sigma,G} \;\rightarrow\; V_{xc}^{\sigma,s}$$

3.5.6 Calculation of ϵ_{xc}^{σ} and V_{xc}^{σ} in the vacuum-region

The vacuum charge density is stored in terms of two-dimensional stars and a z-dependent exponential mesh z_i. The $G_{\parallel}$ component reaches further into the vacuum than $G_{\parallel} \neq 0$ component. In the so called warping region the planewave coefficient on each mesh point are determined by a multiplication with the phase factor $e^{i\mathbf{R}\mathbf{G}_{\parallel}\tau}$. Then, for each grid point, z_i along the z-axis, the two-dimensional charge density is Fourier transformed to a real space grid $(\mathbf{r}_{\parallel}, z_i)$, where V_{xc}^{σ} is calculated. Afterwards, V_{xc}^{σ} is back-transformed and the star coefficients are computed.

$$\rho^{\sigma}(\Phi_s^{2D}, z_i) \;\longrightarrow\; \rho^{\sigma}(\mathbf{G}_{||}, z_i) \;\xrightarrow{\text{2DFFT}}\; \rho^{\sigma}(\mathbf{r}_{||}, z_i) \;\longrightarrow\; V_{xc}^{\sigma}(\mathbf{r}_{||}, z_i)$$

$$\xrightarrow{\text{2DFFT}^{-1}}\; V_{xc}^{\sigma}(\mathbf{r}_{||}, z_i) \;\longrightarrow\; V_{xc}^{\sigma}(\Phi_s^{2D}, z_i)$$

Beyond the warping (i.e. where $\rho(r)$ is no longer expanded in 2D planewaves) region the exchange correlation potential is calculated directly on the z-dependent mesh.

3.5.7 Calculation of ϵ_{xc}^{σ} and V_{xc}^{σ} in the muffin-tin spheres

The muffin-tin charge is expanded into lattice harmonics and radial functions. The radial functions are stored on a discrete real-space mesh. Thus, the transforms to real space affects only the angular part. The charge density is calculated on a set of special angular points $\hat{r_i} = (\theta_i, \phi_i)$. Again, the exchange correlation potential is calculated in real space. Thereafter, the result $V_{xc}^{\sigma}(\mathbf{r})$ is expanded into spherical harmonics Y_L. The Y_L are orthonormal, therefore the coefficients can be obtained from

$$v_{xc,L}^{\sigma}(r) = \int Y_L(\hat{\mathbf{r}}) V_{xc}^{\sigma}(r, \hat{\mathbf{r}}) d\Omega. \tag{3.172}$$

The choice of the points $\hat{r_i} = (\theta_i, \phi_i)$, on which $n^{\sigma}(\mathbf{r})$ and $V_{xc}^{\sigma}(\mathbf{r})$ are calculated, depends on the integration method, that is used to perform the angular integration. In the current implementation (3.172) is computed via a Gauß-Legendre integration and the angular points are chosen such, that the orthonormality condition of the Y_L holds also for the angular mesh $\hat{r_i}$.

3.6 The local orbital extension

In certain materials high-lying core states, the so-called semicore states, pose a problem to FLAPW calculations: they are too delocalized to be described as core electrons (contained entirely in the muffin-tin), but the energy parameter E_l, which would be needed for their description, is already used to describe higher lying valence states. E.g. the $5p$ levels of La are too high in energy to be neglected in total energy calculations [69]. Several possible strategies have been proposed to overcome this problem: The above mentioned reduction of the size of the muffin-tin radius [70], so-called two-window calculations [71] , and the use of local orbitals [69].

The local orbitals are an extension to the FLAPW basis, that can be used to improve the variational freedom for a specific purpose, e.g. to improve the representation of the semicore states. The extra basis functions are completely localized inside the muffin-tin spheres, i.e. their value and derivative falls to zero at the muffin-tin radius. Thus, no additional boundary conditions have to be satisfied. This can be achieved via a linear combination including three radial functions, the standard FLAPW functions u_l^{μ} and $\dot{u}_l^{\mu}$ plus a further radial function u_{lo}^{μ}. This new radial function is constructed in the same way as u_l^{μ}, but with a different energy parameter E_{lo}^{μ}. If the local orbitals are used to treat semicore states, this energy parameter is set to the energy of these states.

The combination of the three radial functions and a spherical harmonic, $\big(a_{lo}^{\alpha} u_l^{\alpha}(r) + b_{lo}^{\alpha} \dot{u}_l^{\alpha}(r) + c_{lo}^{\alpha} u_{lo}^{\alpha}(r)\big) Y_L$, will be called local orbital. l is the angular momentum quantum number of the local orbital, $l = l_{lo}$. The index lo counts the different local orbital radial functions. Let's consider as an example the treatment of the $2p$, $3s$ and $3p$ semicore states of Ti. three additional radial functions are needed, e.g. $2p$: $lo = 1$, $3s$: $lo = 2$, and $3p$: $lo = 3$, thus $l_{lo=1} = 1$, $l_{lo=2} = 0$ and $l_{lo=3} = 1$. The local orbitals with

$lo = 1$ and $lo = 3$ have the same angular momentum quantum number, they differ only by their energy parameters, $E_{lo=1} \neq E_{lo=3}$ and, as a consequence, by their radial functions, $u_{lo=1}(r) \neq u_{lo=3}(r)$. Later in this section linear combinations of the local orbitals will be constructed, by formally coupling the local orbitals to planewaves, as if boundary conditions had to be satisfied. These linear combinations will also be called local orbitals.

The three functions u_l^μ, $\dot{u}_l^\mu$ and u_{lo}^μ have to be combined, so that the value and the derivative of the local orbital go to zero at the muffin-tin radius. Additionally, the resulting radial functions can be required to be normalized. Hence, to determine the coefficients of the radial functions a_{lo}^α, b_{lo}^α and c_{lo}^α we make use of the following three conditions:

$$a_{lo}^\alpha u_l^\alpha\left(R_{MT^\alpha}\right) + b_{lo}^\alpha \dot{u}_l^\alpha\left(R_{MT^\alpha}\right) + c_{lo}^\alpha u_{lo}^\alpha\left(R_{MT^\alpha}\right) = 0 \quad (3.173)$$

$$a_{lo}^\alpha \frac{\partial u_l^\alpha}{\partial r}\left(R_{MT^\alpha}\right) + b_{lo}^\alpha \frac{\partial \dot{u}_l^\alpha}{\partial r}\left(R_{MT^\alpha}\right) + c_{lo}^\alpha \frac{\partial u_{lo}^\alpha}{\partial r}\left(R_{MT^\alpha}\right) = 0 \quad (3.174)$$

$$\int_0^{R_{MT^\alpha}} \left(a_{lo}^\alpha u_l^\alpha\left(R_{MT^\alpha}\right) + b_{lo}^\alpha \dot{u}_l^\alpha\left(R_{MT^\alpha}\right) + c_{lo}^\alpha u_{lo}^\alpha\left(R_{MT^\alpha}\right)\right)^2 r^2 dr = 1 \quad (3.175)$$

where lo is the index of the local orbital, which is necessary because more than one local orbital can be added for each atom. In actual calculations linear combinations of local orbitals that satisfy Bloch's theorem have to be constructed. Therefore $A-$, $B-$ and C-coefficients are employed, which are constructed in the same way as FLAPW A- and B-coefficients (3.90) Hence the additional basis functions are given by:

$$\varphi_{\mathbf{G}_{lo}}^{\mu,lo}(\mathbf{k},\mathbf{r}) = \sum_m \left(A_{Lo}^{\mu\mathbf{G}_{lo}}(\mathbf{k}) u_l^\alpha + B_{Lo}^{\mu\mathbf{G}_{lo}}(\mathbf{k}) \dot{u}_l^\alpha + C_{Lo}^{\mu\mathbf{G}_{lo}}(\mathbf{k}) u_{lo}^\alpha\right) Y_L(\hat{\mathbf{r}}) \quad (3.176)$$

with

$$A_{Lo}^{\mu\mathbf{G}_{lo}}(\mathbf{k}) = e^{i\mathbf{K}_{lo}\tau^\mu} a_{lo}^\alpha 4\pi \frac{1}{W} i^l Y_L^*(\mathbf{R}^\mu \hat{\mathbf{K}}_{\mathbf{lo}}) \quad (3.177)$$

$$B_{Lo}^{\mu\mathbf{G}_{lo}}(\mathbf{k}) = e^{i\mathbf{K}_{lo}\tau^\mu} b_{lo}^\alpha 4\pi \frac{1}{W} i^l Y_L^*(\mathbf{R}^\mu \hat{\mathbf{K}}_{\mathbf{lo}}) \quad (3.178)$$

$$C_{Lo}^{\mu\mathbf{G}_{lo}}(\mathbf{k}) = e^{i\mathbf{K}_{lo}\tau^\mu} c_{lo}^\alpha 4\pi \frac{1}{W} i^l Y_L^*(\mathbf{R}^\mu \hat{\mathbf{K}}_{\mathbf{lo}}) \quad (3.179)$$

Where $\mathbf{K}_{\mathbf{lo}}$ abbreviates $\mathbf{G}_{\mathbf{lo}} + \mathbf{k}$ and Lo abbreviates (lo, m). The local orbitals are coupled to "fictitious" planewaves, even though no boundary conditions have to be satisfied. The G_{lo} can be chosen arbitrarily, subject to the constraint that they yield linearly independent functions $\varphi_{\mathbf{G}_{lo}}^{\mu,lo}(\mathbf{k},\mathbf{r})$. Finding such vectors is straightforward, e.g. by selecting planewave one at time and testing whether the corresponding $\varphi_{\mathbf{G}_{lo}}^{\mu,lo}(\mathbf{k},\mathbf{r})$ is linearly independent of the previous local orbitals. If this is the case, the planewave is accepted, otherwise it is rejected. This procedure is carried out separately for each atom, i.e. the radial functions and spherical harmonics at a single atom form a local orbital, which is added to the FLAPW basis set.

3.7 Minimization of the energy functional

The aim of electronic structure calculation is to minimize the energy functional with respect to the electron density. Within density functional theory this minimization is performed implicitly, by the determination of a selfconsistent density $\rho(\mathbf{r})$. In the previous sections we described, how an effective potential can be calculated form a charge density, how the Kohn-Sham equations including this potential can be solved and how a new electron density can be calculated from the resulting single particle wavefunctions. Combining these steps define a map:

$$\rho'(\mathbf{r}) = F\{\rho(\mathbf{r})\} \tag{3.180}$$

The electron density that minimizes the energy functional $\rho_0(\mathbf{r})$. is a fix-point of $F\{\rho(\mathbf{r})\}$, i.e. it solves

$$\mathcal{F}\{\rho_0(\mathbf{r})\} = 0, \quad \text{with } \mathcal{F}\{\rho(\mathbf{r})\} = F\{\rho(\mathbf{r})\} - \rho(\mathbf{r}) \tag{3.181}$$

The density is expanded into a large set of basis functions. Therefore, in actual calculations, the charge density is a coefficient vector of dimension n, where n is typically of the order of 10^4. Thus, (3.181) constitutes a system of n nonlinear equations, which can be solved by iteration:

$$\rho^{m+1}(\mathbf{r}) = F\{\rho^m(\mathbf{r})\} \tag{3.182}$$

A starting density can be constructed by a superposition of atomic densities. However, this scheme is in general divergent. To achieve convergence the output density has to be mixed with the input density. Different mixing schemes are discussed in the following.

3.7.1 Simple mixing

The slowest method is the “simple mixing”, which converges only linearly.

$$\frac{|\delta\rho^{(m+1)}|}{|\delta\rho^{(m)}|} \leq \text{const.} \tag{3.183}$$

where $\delta\rho^{(m)}$ is the difference of the density of the m$^{\text{th}}$ iteration and the unknown fix-point, $\delta\rho^{(m)} = \rho^{(m)} - \rho_0$. The density for the next iteration is constructed as a linear combination of $\rho^{(m)}$ and $F\{\rho^m\}$ according to :

$$\begin{aligned} \rho^{(m+1)} &= (1-\alpha)\rho^{(m)} + \alpha F\{\rho^m\} \\ &= \rho^{(m)} + \alpha\mathcal{F}\{\rho^{(m)}\} \end{aligned} \tag{3.184}$$

α is the so-called mixing parameter. If it is chosen small enough the iteration converges and is very stable. In spin-polarized calculations different mixing parameters can be used for the charge and the magnetization density. Usually, the spin mixing parameter can be chosen far larger than the parameter for the charge density. However,

for the type of systems we are interested in α is very small, requiring many hundreds of iterations.

3.7.2 The Newton-Raphson method

In the Newton-Raphson method the functional $\mathcal{F}\{\rho\}$ is linearized around the approximate solution $\rho^{(m)}$

$$\mathcal{F}\{\rho\} \approx \mathcal{F}\{\rho^{(m)}\} + \mathcal{J}\{\rho^{(m)}\}(\rho - \rho^{(m)}) \tag{3.185}$$

where the Jacobian is defined by :

$$\mathcal{J}\{\rho^{(m)}(\mathbf{r})\} = \left.\frac{\partial \mathcal{F}\{\rho(\mathbf{r})\}}{\partial \rho(\mathbf{r}')}\right|_{\rho^{(m)}(\mathbf{r})} \tag{3.186}$$

In actual calculations the Jacobian is a $n \times n$ matrix. Similar to the well known Newton method for one dimensional functions, the next approximation to ρ_0, $\rho^{(m+1)}$, is determined from the requirement, that the linearized functional in (3.185) vanishes at $\rho^{(m+1)}$. Thus, $\rho^{(m+1)}$ is given by :

$$\rho^{(m+1)} = \rho^{(m)} - \left[\mathcal{J}\{\rho^{(m)}\}\right]^{-1} \mathcal{F}\{\rho^{(m)}\} \, . \tag{3.187}$$

The Newton-Rapson method converges quadratically:

$$\frac{|\delta\rho^{(m+1)}|}{|\delta\rho^{(m)}|^2} \leq \text{const.} \tag{3.188}$$

The major drawback of this method is the difficulty to evaluate the Jacobian. Even if the functional $\mathcal{F}\{\rho\}$ was know, the evaluation would be cumbersome due to the enormous size of $\mathcal{J}\{\rho\}$. In addition, the Jacobian has to inverted where the amount of calculation scales with cube of the dimension. A further problem is that the convergence radius is rather small so that the method can only be used if $\rho^{(m)}$ is already very close to ρ_0.

3.7.3 Quasi-Newton methods

With the development of the Quasi-Newton methods it became possible to exploit the advantages of the Newton-Raphson method, i.e. to make use of the information that is contained in the Jacobian, for problems where the Jacobian can not be calculated or its determination is too demanding. Rather than computing the Jacobian each iteration, an approximate Jacobian is set up and improved iteration by iteration. Form the linearization of $\mathcal{F}\{\rho\}$ (3.185) we find the following condition for the Jacobian, which is usually called quasi-Newton condition:

$$\begin{aligned} \Delta\rho^{(m)} &= \left[\mathcal{J}^{(m)}\right]^{-1}\Delta\mathcal{F}^{(m)} \\ \Delta\rho^{(m)} = \rho^{(m)} - \rho^{(m-1)}, &\Delta\mathcal{F}^{(m)} = \mathcal{F}\{\rho^{(m)}\} - \mathcal{F}\{\rho^{(m-1)}\}\ . \end{aligned} \tag{3.189}$$

Quasi-Newton methods converge super-linearly

$$\frac{|\delta\rho^{(m+1)}|}{|\delta\rho^{(m)}|} \to 0,$$

and have a larger convergence radius than the Newton-Raphson method. Since the Jacobian is build up iteration, the "history" of the previous iterations is memorized in $\mathcal{J}$, whereas the Jacobian of the Newton-Raphson method depends only on the previous iteration. In this sense the Newton-Raphson method is self corrective [72], it "forgets" inadequately chosen correction. The quasi-Newton method sometimes need to be restarted, if the iteration converges only slowly. This can happen if the starting density is very far from n_0 or when physical or numerical parameters that affect the calculations are changed during the iteration. Equation (3.189) does not determine the Jacobian uniquely, instead(3.189) constitutes a system of n equations for n^2 unknowns. The various quasi-Newton schemes differ by the ansatz how the new information is used to build the inverse Jacobian . The methods that are implemented in the FLAPW code are discussed in [73]

4 In plane polarization of $BaTiO_3$ and $PbTiO_3$ thin films

Perovskites are an extremely important class of ferroelectric materials. Generically these compounds have the chemical formula ABO_3 where A is a monovalent or divalent cation and B is often penta- or tetravalent metal. The perfect perovskite structure is very simple and has full cubic symmetry Fig. 4.1 (left). It can be thought of as a lattice of corner sharing oxygen octahedra with interpenetrating simple cubic lattices of A and B cations. The B cations sit at the center of each oxygen octahedron while the A metal ions lie in 12-fold coordinated sites between the octahedral. The perovskites exhibit a diverse range of phases including transitions to both ferroelectric and antiferroelectric states as well as structural transitions to states involving the tilting of oxygen octahedra.

In spite of the fact that the perovskites have been the subject of intense investigation since the discovery of ferroelectricity in $BaTiO_3$ in the 1940s, there is still no complete understanding of nature of the transitions in these materials.

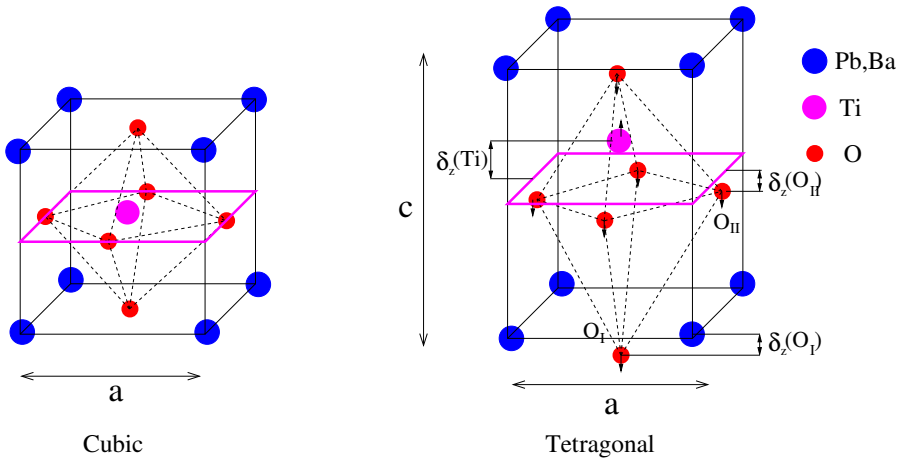

Figure 4.1: Structure of the cubic and tetragonal perovskite compounds $ATiO_3$. Cubic Structure left, tetragonal Structure right.

4.1 Crystal structure

$PbTiO_3$ undergoes a single transition cubic into a tetragonal ferroelectric (FE) phase at 763 K and then remains in this structure down to zero temperature. $BaTiO_3$ displays

a series of three transitions from cubic to tetragonal, orthorhombic, and rhombohedral FE phases at 403 K, 278 K, and 183 K, respectively [74]. Because we are primarily interested in the room-temperature structures of these materials, we have focused on the cubic and tetragonal phases structures Fig.4.1.

The structural optimization is performed with the density function of theory (DFT) formalism. It basically consist in determining the lattice parameters and atomic positions which minimize the total energy of system and the forces on each atoms. The Calculations have been performed in the general framework of DFT using the full-potential linearized augmented planewave (FLAPW) method as implemented in FLEUR code. Exchange and correlation were treated using the GGA (PBE [75] and WC [76]) and LDA [77] for the potential. The wave functions within the muffin-tin spheres were expanded in spherical harmonics with an angular momentum of up to l = 14. In the interstitial region, plane waves with reciprocal lattice vectors up to G_{max} = 11(a.u.)$^{-1}$ were included and the plane-wave cutoff ($R_{MT}K_{max}$) was set to 6.3. For each compound, the muffin-tin radii (R_{MT}) were chosen as 2.5, 2.1, 1.71, and 1.30 a.u. for Ba, Pb, Ti, and O, respectively. Ba $5s$ and $5p$ states, Pb $5d$ states, Ti $3s$ and $3p$ states were treated as local orbitals. Selfconsistency was considered to be achieved when the total energy variation from iteration to iteration did not exceed 10^{-6} Htr. A mesh containing 40 **k** $[8 \times 8 \times 8]$ points in the irreducible Brillouin zone for the cubic (tetragonal) phases was used.

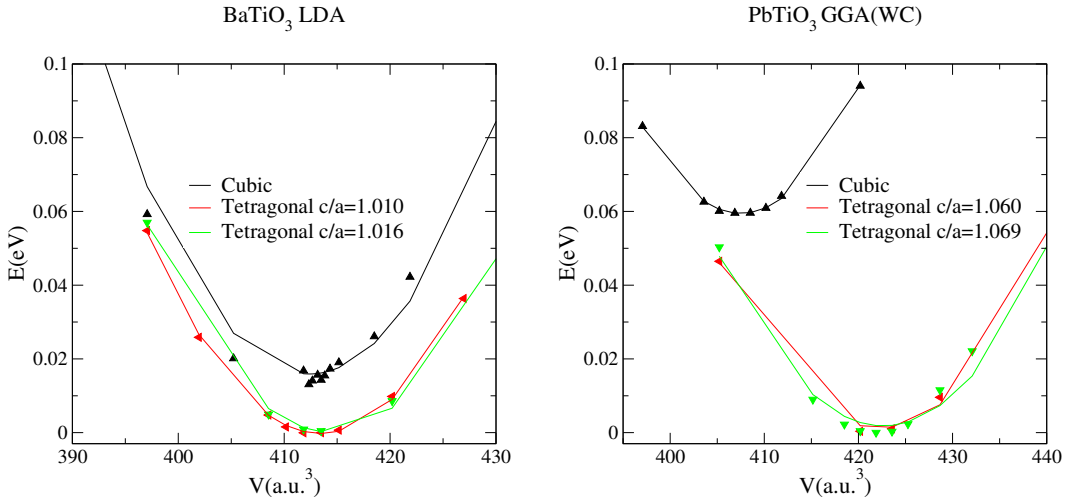

Figure 4.2: Energy as a function of volume for the cubic and tetragonal phases of $BaTiO_3$ (left), $PbTiO_3$ (right) from DFT calculations.

The optimization procedure is as the following. For cubic structures, we minimized the total energy respect to lattice constant a. The tetragonal structures were optimized by letting the internal coordinates of the ions change in the way symmetry allows (distortion in z direction) at fixed c/a ratio and volume. The forces on each ion were minimized to less than 10^{-3} Htr/a.u. Then, by using the optimized internal coordinates of the ions, c/a ratio was optimized at constant volume. Afterwards

by using the optimized fractional coordinates of the ions and c/a, volume has been optimized. This process was repeated until consistency.

Table 4.1 and 4.2 show the structural parameters for $BaTiO_3$ and $PbTiO_3$. We compared different structures which are calculated with different exchange and correlation potential. We find that gives best agreement to experimental data LDA for $BaTiO_3$ and GGA(WC) for $PbTiO_3$. This is not surprising, since a WC was designed for $PbTiO_3$. But for $BaTiO_3$ the old HL-LDA performs better. Energy-volume behavior of the different crystalline phases of $BaTiO_3$ and $PbTiO_3$ are shown Fig.4.2. The volumes of cubic and tetragonal phases for $BaTiO_3$ are the same and the difference between the energy of the two phases is 18eV. For the $PbTiO_3$ the difference of volumes for cubic and tetragonal phases is about 3% of cubic volume and the differnce for enegy is 60 meV.

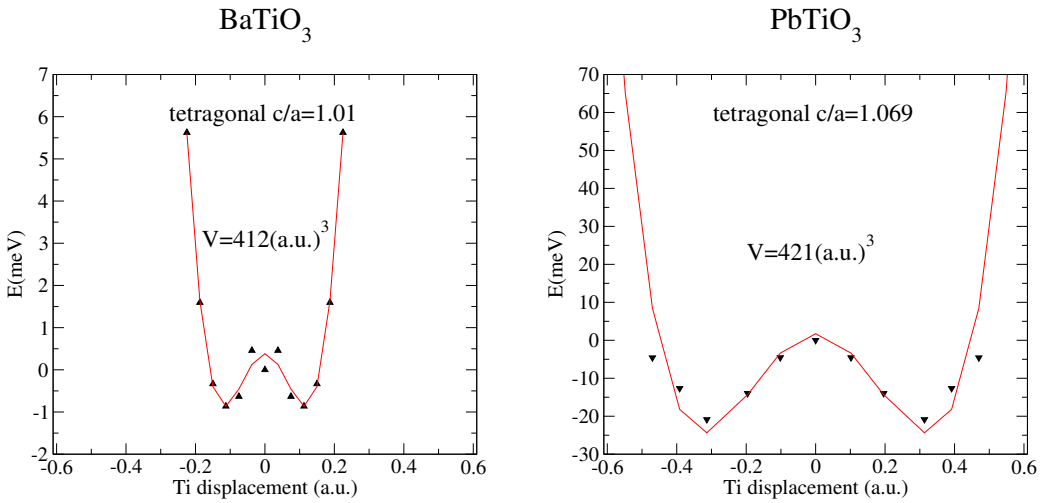

Figure 4.3: Energy(per 5 atom unit cell) versus displacement of Ti along the [001] direction in $BaTiO_3$ and $PbTiO_3$. Optimized volumes and c/a with DFT calculations have been used for $BaTiO_3$ and $PbTiO_3$ in tetragonal phases.

The potential energy surface for tetragonal displacements in $BaTiO_3$ and $PbTiO_3$ have been considered. All atoms have been frozen at the paraelectric perovskite structural(A(0.0,0.0,0.0), Ti(0.5,0.5,0.5), O(0.5,0.5,0.0), O(0.5,0.0,0.5), O(0.0,0.5,0.5)). Afterwards energies are calculated in terms of distortion the Ti along [001] direction. Figure 4.3 shows energy surfaces versus the displacement of Ti for $BaTiO_3$ and $PbTiO_3$. The most challenging feature is the large deference in well depth for $BaTiO_3$ and $PbTiO_3$. The differences are consistent with different ferroelectric behavior of two material.

Table 4.1: $BaTiO_3$ bulk properties:volume(V), c/a ratio and internal coordinates δ_z for the cubic and tetragonal phases using different xc-potentials. experimental data was taken from Ref. [78]

Phase	Parameter	Expt.	LDA	WC	PBE
cubic	V(a.u.^{3})	430.59	411.70	423.74	439.82
tetragonal	V(a.u.^{3})	434.47	412.49	426.95	449.45
	c/a	1.011	1.010	1.024	1.048
	δ_z(Ti)	0.0135	0.0075	0.0142	0.0110
	δ_z(O_I)	-0.0240	-0.0220	-0.0320	-0.0550
	δ_z(O_{II})	-0.0150	-0.0165	-0.0200	-0.0350

Table 4.2: $PbTiO_3$ bulk properties:volume(V), c/a ratio and internal coordinates δ_z for the cubic and tetragonal phases using different xc-potentials. experimental data was taken from Ref. [79]

Phase	Parameter	Expt.	LDA	WC	PBE
cubic	V(a.u.^{3})	391.13	395.36	408.04	421.61
tetragonal	V(a.u.^{3})	426.18	402.43	421.36	475.80
	c/a	1.071	1.033	1.068	1.234
	δ_z(Ti)	0.0380	0.0284	0.0347	0.0521
	δ_z(O_I)	0.1120	0.0779	0.1040	0.1622
	δ_z(O_{II})	0.1120	0.0916	0.1120	0.1774

4.1.1 Electronic structure

$PbTiO_3$ and $BaTiO_3$ have different ferroelectric behavior. For example $PbTiO_3$ has bigger c/a ratio as compered to $BaTiO_3$. That is important to understand the origin of the differences in their behavior. To this end partial densities of states for $BaTiO_3$ and $PbTiO_3$ are calculated using the structural parameters as given in the previous section. Figure 4.4 show the electronic partial densities of states for $PbTiO_3$ cubic and tetragonal. The left set of panels show the partial densities of states for cubic $PbTiO_3$. In the cubic case O_I and O_{II} have same electronic structures and Ti $3d$ orbitals show cubic (O_n) symmetry: all $t_{2g}(d_{xy}, d_{yz}, d_{zx})$ and $e_g(d_{x^2-y^2}, d_{z^2})$ orbitals are energetically equivalent. The right set of panels show the partial densities of states for tetragonal $PbTiO_3$. In the tetragonal case the Ti $d_{x^2-y^2}$ states move down in energy, Ti $3d_{z^2}$ are split of. There is a strong hybridization between O_{II} $2p_y$ and Ti $3d_{x^2-y^2}$ but also between O_I $2p$ and Pb $6s$.

Figure 4.5 shows the electronic densities of states for tetragonal $PbTiO_3$ and $BaTiO_3$. The big difference between $PbTiO_3$ and $BaTiO_3$ electronic structures is the large hybridization between the Pb $6s$ and O $2p$ states, whereas there is little hybridization between the Ba $5p$ and the O $2p$ states; the Ba ion is close to be totally ionized and thus a spherical, Ba^{2+} ion. Furthermore, the interaction between the Pb $6s$ and O $2p$ leads indirectly to increased hybridization between the Ti $3d$ and O $2p$ states, which further stabilizes the ferroelectric state in $PbTiO_3$ relative to $BaTiO_3$. It is the large covalency between Pb and O and the stronger interactions between Ti and O that lead

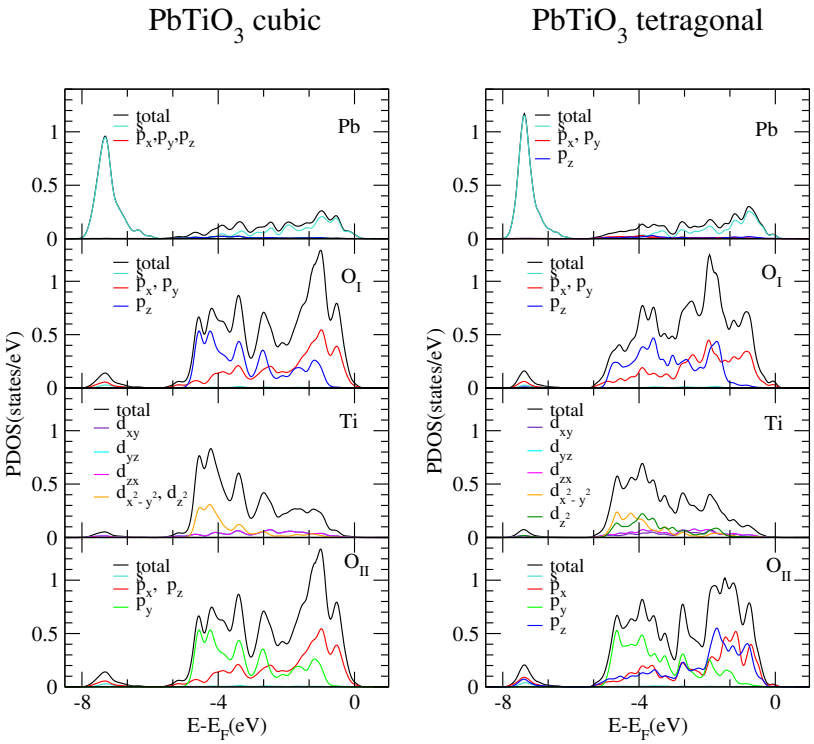

Figure 4.4: Partial densities of states (PDOS) of $PbTiO_3$ cubic and tetragonal. The left set of panels show the partial densities of states for cubic $PbTiO_3$, O_I and O_{II} have same electronic structures and Ti $3d$ has symmetric structure. The right set of panels show the partial densities of states for tetragonal $PbTiO_3$, $d_{x^2-y^2}$ states move down in energy and Ti $3d_{z^2}$ and $3d_{x^2-y^2}$ are split.

to the greater well depths in $PbTiO_3$ and larger ferroelectric distortion in $PbTiO_3$. Also, the favorable interactions between Pb and O cause the energy to be lowered when the Pb-O distance is reduced. However, in the perovskite structure, the Ti-O repulsion dominates in the equation of state, so that the cell volume can only shrink slightly in $PbTiO_3$ relative to $BaTiO_3$. By straining, however, four oxygens (in the $a - b$ plane, assuming c is elongated) move closer to the Pb, linear in the strain, whereas the other eight Pb-O distances are increased [25]. An indirect effect of the Pb-O bonding on the Ti-O hybridization is that the Ti $3d$ states in $PbTiO_3$ are lower than in $BaTiO_3$. It should be noted that in many IV-VI semiconductors a structural distortion can actually be driven solely by the ns^2(n is Quantum number) valent electrons of the cation [80–82]. The ns^2, usually referred to as the lone pair, can lose inversion symmetry due to mixing of the ns^2 ground state with the low-lying excited ns^1np^1 state. this mixing can only occur if the ionic site does not have inversion symmetry [83] and so when the energy gain due the mixing is larger than the interionic repulsion which oppose the ionic shift, the crystal distorts [84].

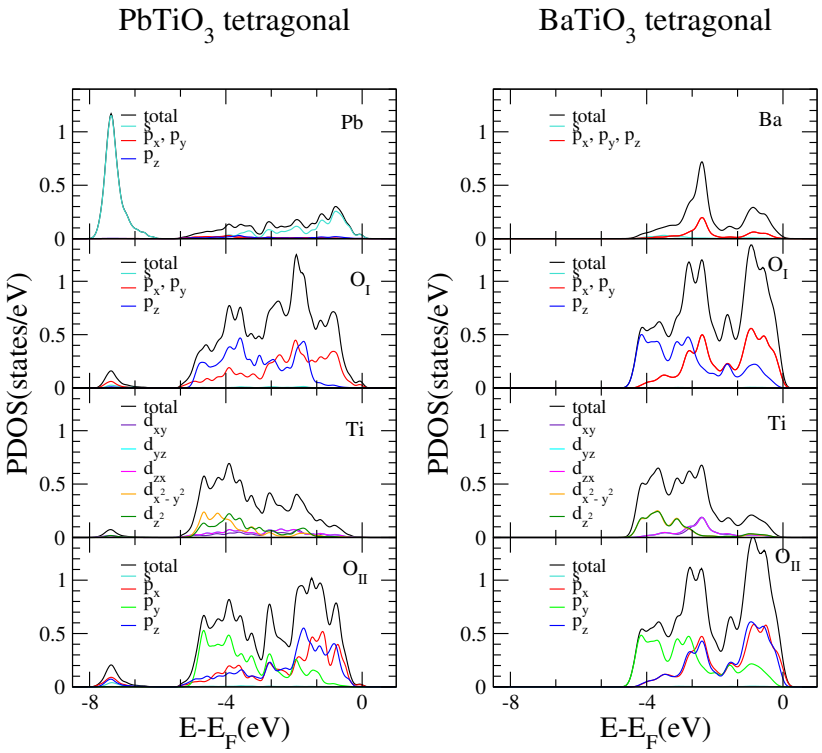

Figure 4.5: Partial densities of states (PDOS) of $PbTiO_3$ and $BaTiO_3$ in tetragonal structure. The left set of panels show the partial densities of states for $PbTiO_3$. The right set of panels show the partial densities of states for $BaTiO_3$. The most important difference between $PbTiO_3$ $BaTiO_3$ densities of states is in the large hybridization of the Pb $6s$ states with the O $2p$ states in $PbTiO_3$.

4.2 Surface effects on in plane polarization

In recent years, a large amount of research worldwide was focused on the growth and characterization of ferroelectric thin films. On one hand, their ferroelectric, dielectric, and piezoelectric properties were found to be promising for microelectronic and micromechanical applications [85]. On the other hand, the physical properties of ferroelectric thin films were found to be substantially different from those of bulk materials. The ferroelectric properties are known to degrade in thin films [86], and it is very important to understand the origin of this effect.

First-principles studies on ABO_3 perovskite oxides thin films considered isolated slabs in vacuum with free surfaces. These calculations were a perfect scenario to ascertain whether the mere presence of a surface is enough to suppress the spontaneous polarization or, in other words, to assign a completely intrinsic origin to the degradation of the ferroelectric properties observed experimentally in small particles and thin films [87–91].

At any surface the translational symmetry is broken, i.e. the surface can remain periodic in the plane, but the crystal is no more periodic in the direction perpendic-

ular to the surface. The atoms in the outermost layers (those which are closer to the surface) will feel the absence of neighboring atoms to interact with. These missing bonds affect the structural and electronic properties of the materials. In the particular case of ABO_3 perovskite oxides, the hybridization between Ti $3d$ and O $2p$ orbitals, responsible for the giant effective charges and, ultimately, for the ferroelectric instability, is modified(see Sec. 4.2.3) The absence of some of the atoms leaves highly energetic and electronically active dangling bonds at the surface. In most cases this leads to structural relaxations, and in case of covalent bonding e.g. in semiconductors even reconstructions of the surface geometry to produce a more satisfactory bonding configuration, that might affect significantly the physical properties surface. The energy scale of the surface relaxations and reconstructions is orders of magnitude higher than the depth of the bulk ferroelectric double well, so it is expected to affect the ferroelectric ground state of the system.

The determination of electronic and structural properties is a delicate problem, that turns out to be strongly dependent on the nature of the material. Only changing one of the cations in a ABO_3 perovskite surface can lead to very different qualitative and quantitative behavior. Even more, for a given material the results change also with the particular orientation and atomic termination i.e. AO or BO_2 of the surface.

For studying of thin films or heterostructures, the first step is to choose an initial symmetry for the simulations and to define a reference ionic configuration that is obtained by cutting the bulk material along a particular direction. The reference configuration to which we will refer when discussing surface atomic relaxation is therefore the atomic arrangement of an unrelaxed truncated bulk structure. Usually, the bulk structure that is truncated is the theoretically relaxed bulk structure. In some cases, however, in order to include the effect of the epitaxial strain induced by a substrate, the reference configuration is defined by cutting a strained bulk phase, with the same strain constraints than those expected in the thin film. The three most important orientations for ABO_3 surfaces (and also those which have been most investigated theoretically) are (001), (110) [91–93], and (111) [94–96]. In the (001) cut, the ABO_3 perovskite structure can be considered as an alternating stack of AO and BO_2 layers. For II-IV perovskites, where atoms A and B are divalent and tetravalent respectively, in the ionic limit, the structure is a sequence of neutral sheets ($A^{2+}O^{2-})^0$ and $[B^{4+}(O^{2-})_2]^0$. The surface might have two possible different terminations, with the outermost layer being a AO layer or a BO_2 layer. By contrast, both the (110) and the (111) orientations are polar irrespectively of the cation valence states. In the (110) cut, the perovskite structure is composed of $(ABO)^{4+}$ and $(O_2)^{4-}$ stacks, whereas the atomic planes in the (111) cut are AO_3 and B, and they are both charged. The highly polar nature of the (110) and (111) surfaces makes them unstable and highly reactive in comparison to the (001) surface [97]. We will focus on the (001) orientation of the $BaTiO_3$ and $PbTiO_3$ structures.

In these system, bulk properties are recovered a few atomic layers away from the outermost surface layers. This allows the use of thin slabs of the order of ten layers thick. Typically (1×1) surface geometries are simulated. This constraint al-

lows atomic relaxations but prevents the study of more complicated reconstructions involving for instance the rotation of oxygen octahedra, essential to describe the antiferrodistortive instability that is observed on $PbTiO_3$ surfaces [31, 98].

If the original bulk, from which the reference structure is cleaved had a perfect cubic symmetry, then the resulting cubic surface would display mirror symmetry planes M_x , M_y and, if the slab is symmetrically terminated, M_z (this last one relative to the central layer of the slab). A tetragonal reference structure can also be constructed for $BaTiO_3$ and $PbTiO_3$ by cleaving the bulk tetragonal material. The cases with a polarization normal to the surface will be discussed in chapter 5. There, we will assume that the ferroelectric axis lies parallel to the surface along the x-axis(Fig 4.6), then the M_x symmetry is broken in the tetragonal reference configuration, whereas the system preserves the M_y symmetry and, additionally for symmetric slabs, the M_z symmetry with respect to the center of the slab.

4.2.1 Structural relaxations

As it has been already mentioned before, the existence of highly energetic dangling bonds at the surface yields non-vanishing forces on the atoms in the layers close to the surface. Therefore atomic rearrangements (including relaxations and reconstructions) occur at the surface in order to strengthen the remaining bonds, and to minimize the effects of the lack of hybridization with the missing atoms. Starting from the truncated bulk reference ionic configuration previously defined, a relaxation of the atomic coordinates, while preserving the full set of symmetries, is carried out until the maximum component of the force on any atom is smaller than a given threshold, of the order of 10^{-3}Htr/a.u. In order to characterize the atomic relaxation, we define δ_z (K_i) [respectively $\delta_z(O_i)$] as the displacement of the cation (respectively oxygen) along z in layer i, with respect to the initial reference configuration. We introduce the displacement of the mean position of each atomic plane as (4.1)

$$\beta_i = [\delta_z(K_i) + \delta_z(O_i)]/2 \tag{4.1}$$

and the change in the interplanar distance between consecutive planes i and j as

$$\Delta d_{ij} = \beta_i - \beta_j. \tag{4.2}$$

The rumpling parameter of layer i describes the movement of the ions with respect to the mean position of each atomic plane and corresponds to

$$\eta_i = [\delta_z(K_i) - \delta_z(O_i)]/2. \tag{4.3}$$

It is positive when the cation K_i is above the oxygen, and negative otherwise. Table 4.3 and 4.4 show the atomic relaxations for the cubic and tetragonal, symmetric, (1×1) TiO_2-terminated and *A*O-terminated free-standing slabs of $BaTiO_3$, and $PbTiO_3$, all of them obtained within the LDA and GGA(WC) approximation to DFT (respectively for $BaTiO_3$ $PbTiO_3$). In each case, the in-plane lattice constant was constrained

	$BaTiO_3$		$PbTiO_3$	
	cubic	tetragonal	cubic	tetragonal
Δd_{12}	-0.1110	-0.1040	-0.179	-0.1511
Δd_{23}	0.0675	0.0640	0.1361	0.1830
Δd_{34}	-0.0080	-0.0160	-0.0276	-0.0295
Δd_{45}	0.0100	0.0120	0.007	0.0086
η_1	-0.0460	-0.0490	-0.0700	-0.0679
η_2	0.0437	0.0400	0.0862	0.0787
η_3	-0.0062	-0.0080	-0.0152	-0.0960
η_4	0.0055	0.0065	0.0120	0.0137

Table 4.3: Change of the interlayer distance Δd_{ij} and layer rumpling η_i (units of lattice constant) for the relaxed TiO_2-terminated (001) surfaces of $BaTiO_3$ and $PbTiO_3$ in the cubic and tetragonal phases.

to the one which is given in Sec(4.2) for each material. This choice ensures that the relaxations are intrinsic to the surface and not induced by mechanical strains.

Some common important features for all the surfaces are as follows: (i) As expected, the largest relaxations are found for the surface atoms. (ii) The surface layer contracts substantially inwards (i.e. toward the bulk) with both metal and oxygen atoms displacing in the same direction with respect to reference positions. (iii) The relaxations of the metal atoms are much larger, leading to a rumpling of the layers, and to the appearance of an ionic surface dipole. (iv) All the surfaces display a similar oscillating relaxation pattern with a reduction of the interlayer distance Δd_{12}, an expansion of Δd_{23} , and a reduction again of Δd_{34}. Compared to $BaTiO_3$, the amplitudes of the relaxation of $PbTiO_3$ are significantly larger; (v) A similar oscillating behavior is observed for η_i (successive $+$ and $-$ signs). The amplitude of η rapidly decreases showing that the major relaxations are localized at the surface. (vi) The outward relaxation of the *A*-cation of the second layer of the TiO_2-terminated surface is noteworthy, at odds with an usual experimental approximation, made to simplify the refinement procedure of the data, that assumes the absence of buckling in the second and third layers.

Starting from the tetragonal phase with the polarization lying in a plane parallel to the surface, the most important change is the lack of symmetry of the O atoms of the TiO_2 layer with respect to their position perpendicular to the surface. Almost no change in the relaxations along z for $BaTiO_3$ is observed with respect to those of the cubic phase. The same is true for the TiO_2-terminated surface of $PbTiO_3$. For the PbO-terminated surface, in contrast, the changes in the interlayer distances and the layer rumplings are reduced in the tetragonal phase.

	$BaTiO_3$		$PbTiO_3$	
	cubic	tetragonal	cubic	tetragonal
Δd_{12}	-0.1000	-0.1080	-0.1863	-0.1110
Δd_{23}	0.0550	0.0516	0.1147	0.0670
Δd_{34}	-0.0110	-0.0185	-0.0368	-0.0220
Δd_{45}	0.0010	0.0021	0.0024	0.0027
η_1	-0.0301	-0.0315	-0.0775	-0.0238
η_2	0.0082	0.0071	0.0253	0.0154
η_3	-0.0084	-0.0101	-0.0240	-0.0166
η_4	0.0312	0.0021	0.0032	0.0037

Table 4.4: Change of the interlayer distance Δd_{ij} and layer rumpling η_i (units of lattice constant)for the relaxed *A*O-terminated (001) surface of $BaTiO_3$ and $PbTiO_3$ in the cubic and tetragonal phases.

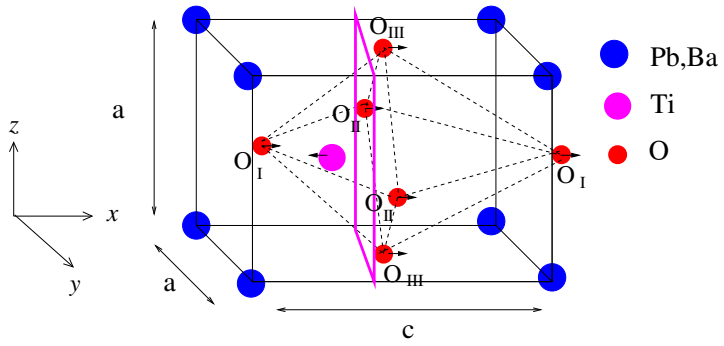

Tetragonal

Figure 4.6: Structure of the tetragonal perovskite compounds $ATiO_3$. O_I ,O_{II} and O_{III} are the oxygen atoms lying along the x, y and z direction from the Ti atom, respectively. Arrows indicate the displacements of the Ti and O atoms relative to the A atoms in the case of the tetragonal phase.

4.2.2 Influence of the surface upon ferroelectricity

We turn now to the question of whether the presence of the surface has a strong effect upon the near surface ferroelectricity. To analyze whether the ferroelectric order is enhanced or suppressed near the surface, we introduce average ferroelectric distortions δ_{FE} for each layer of the surface slabs cf.Fig 4.7:

$$\begin{aligned} \delta_{FE} &= |\delta_x(A) - \delta_x(\mathrm{O_{III}})| \\ \delta_{FE} &= |\delta_x(\mathrm{Ti}) - [\delta_x(\mathrm{O_I}) + \delta_x(\mathrm{O_{II}})]/2| \end{aligned} \tag{4.4}$$

The calculated values of δ_{FE} for $BaTiO_3$ and $PbTiO_3$ are shown in fig 4.7. For the PbO-terminated surface of $PbTiO_3$, one can see a clear increase in the average ferroelectric distortions δ_{FE} when going from the bulk values to the surface layer. On the other hand, for the TiO_2-terminated surface, the average distortions are slightly

decreased at the surface. Surprisingly, this is just the opposite of what one observes for $BaTiO_3$, where a reduction of the ferroelectric distortions for the BaO-terminated surface and a moderate enhancement for the TiO_2-terminated surface can be observed. (Of course, the distortions are also much smaller for $BaTiO_3$ surfaces, as they are in the bulk, compared to $PbTiO_3$.) These results tend to confirm that Pb is a much more active constituent in $PbTiO_3$ than is Ba in $BaTiO_3$.

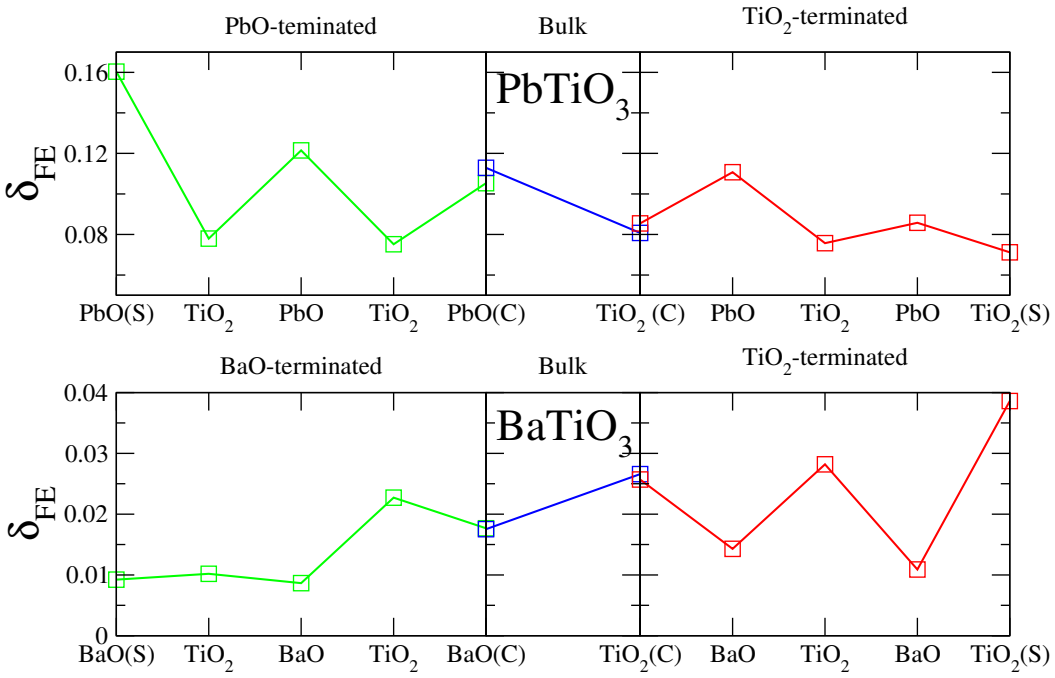

Figure 4.7: Calculated FE distortion δ_{FE} for 9 layer $PbTiO_3$ and $BaTiO_3$ thin film with mirror symmetry (left and right) film and bulk(in middle)

4.2.3 Electronic structure

To analyze the electronic origin of the enhancement/reduction of the polarization at the surface in this section the influence of surface on partial densities of states has been investigated. Figures 4.8 to 4.11 depict the partial densities of states (PDOS) of $BaTiO_3$ and $PbTiO_3$ thin films, where both TiO_2 and AO terminated surfaces are considered. The PDOS at the central layers is similar to the bulk but at the surfaces it has a different behavior: All states of O at the BaO-terminated surface are shifted to high energy (Fig. 4.8) which indicates a decrease in hybridization. Therefore FE distortion δ_{FE} at the BaO-terminated surface layer has been reduced. In contrast to $BaTiO_3$, there is a strong hybridization between O $2p$ and Pb s at the PbO terminated surface (Fig. 4.9). Thus FE distortion δ_{FE} at the PbO-terminated surface layer has been enhanced. Figure 4.10 show O p_y at the TiO_2 terminated surface of $BaTiO_3$ is shifted toward the Fermi level.

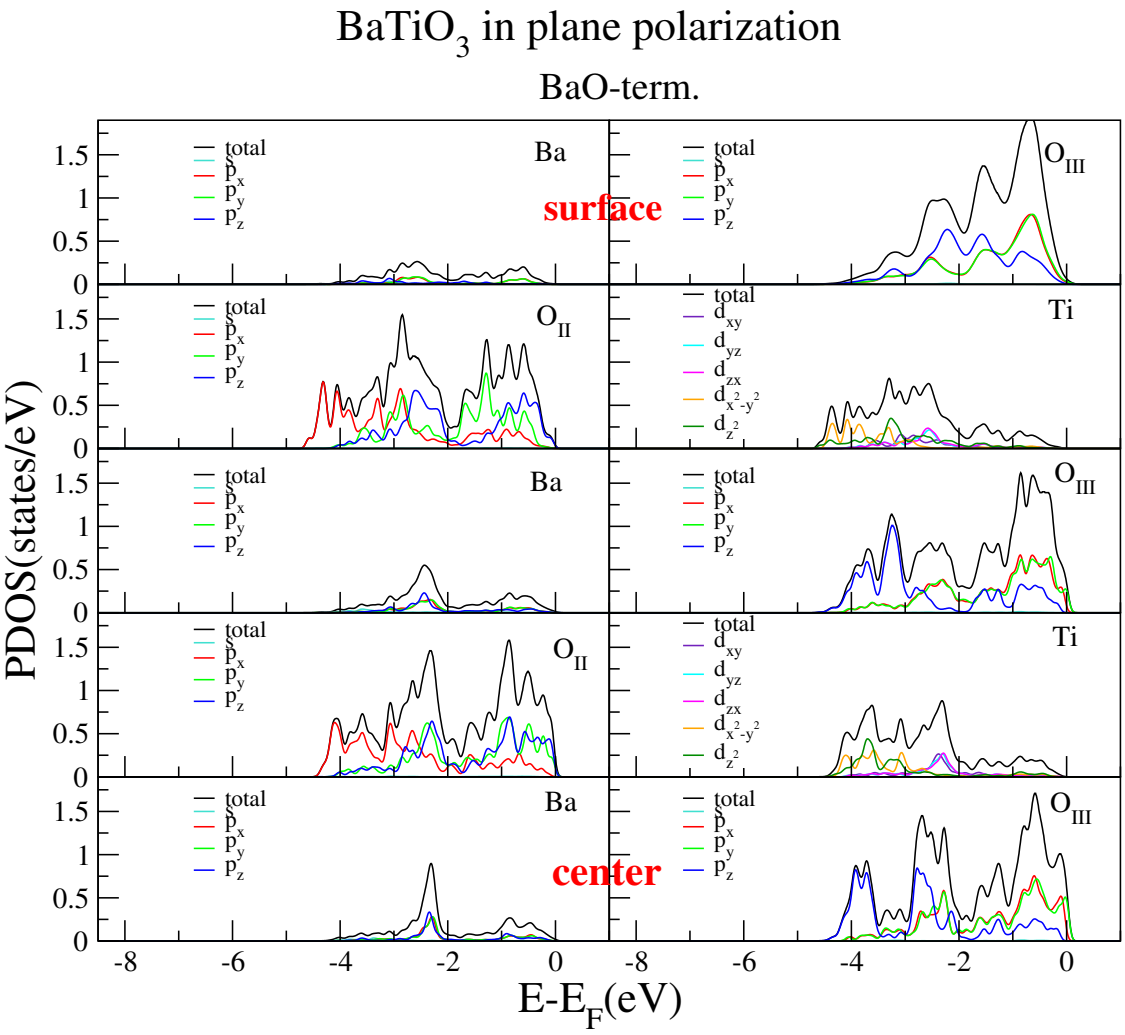

Figure 4.8: Partial densities of states (PDOS) for a BaO terminated symmetric 9 layer film of $BaTiO_3$ with in plane polarization. States of O at the surface move up in energy indicating decrease hybridization.

4.3 Stacking faults effects on in plane polarization

Oxide thin films at the film/substrate interface have complex structures that is depend on the growth conditions. Stress relaxation in mismatched epitaxial films leads to the formation of misfit dislocations at the interfaces, which are commonly accompanied by threading dislocations that extend across the film. Several results have been reported on misfit dislocation in epitaxial pervskite oxide thin films. Structure of misfit dislocation have been analyzed in $PbTiO_3$ films grown on MgO(100)and $SrTiO_3$ substrates [99, 100]. Other reports have indicated that misfit dislocation in $BaTiO_3/SrTiO_3$ and $BaTiO_3/LaAlO_3$ are edge dislocation and the existence of stack-

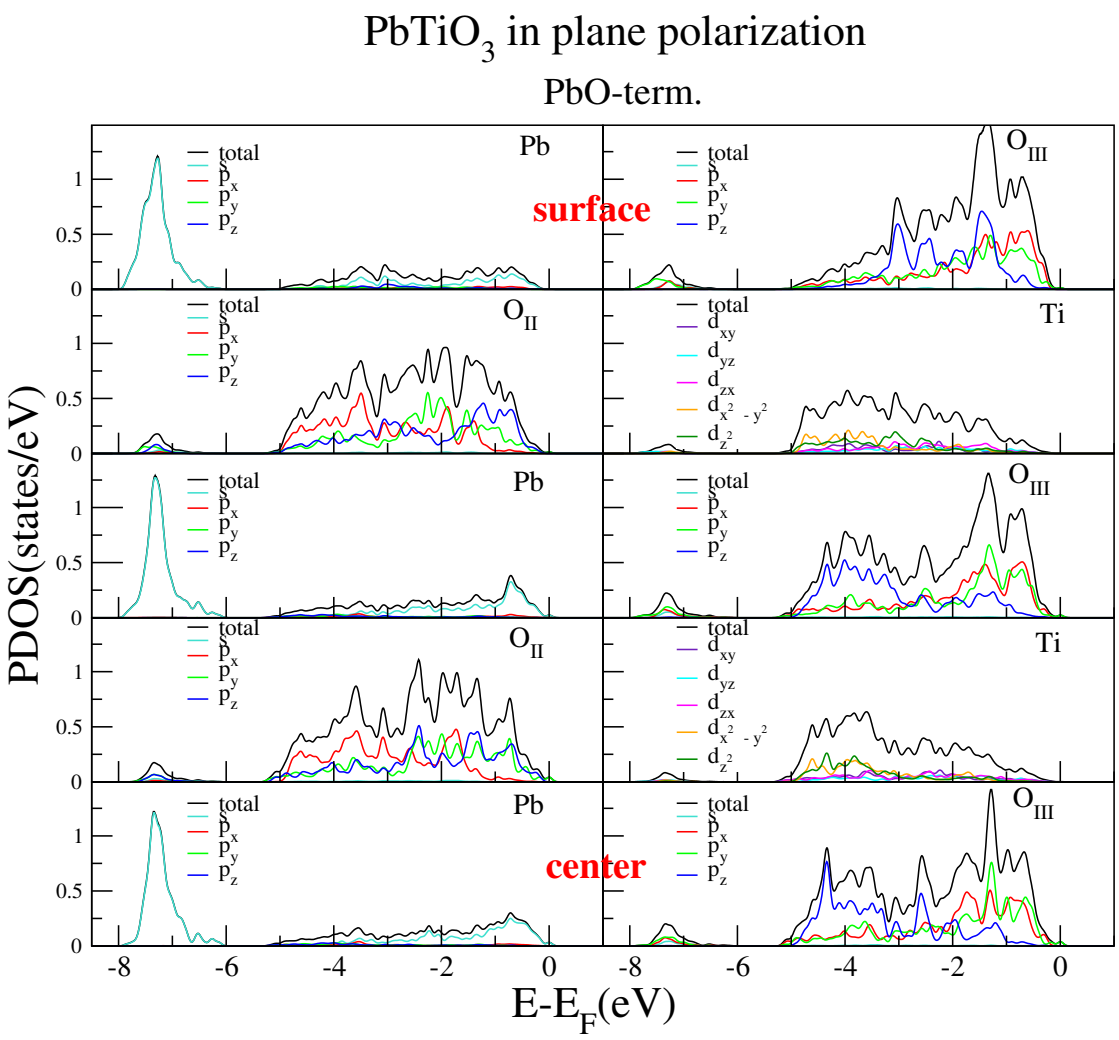

Figure 4.9: Partial densities of states (PDOS) of PbO terminated 9 layers thin film of $PbTiO_3$ with in plane polarization.Op_y at the surface of is shifted toward to Fermi level.

ing faults [101–103]. Structural defects such as misfit dislocation and stacking faults are well known to significantly influence the physical properties of oxide thin films and heterostructures [104].

In this section we have studied influences of stacking faults on the polarization. Two models of stacking faults for $BaTiO_3$ and $PbTiO_3$ thin films are considered. In the first model putting double layers of TiO_2 (Ti_2O_4) on one side of the films are formed while in the second one we study double layers of AO (A_2O_2) on one side of the films. For the Ti_2O_4 model, the positions of atoms at the layer are in inner TiO_2 the same as in the unfaulted structure. In the surface layer the positions of O are $(00z)$ and $(\frac{1}{2}\frac{1}{2}z)$ which leave two possibilities for the position of Ti: The first possibility is $(\frac{1}{2}0z)$ (i.e. it lies on the axis of polarization(x)) and the second is $(0\frac{1}{2}z)$(i.e. it lies on the y axis). The former possibility will be denoted as Ti$_x$, the latter one as Ti$_y$. For

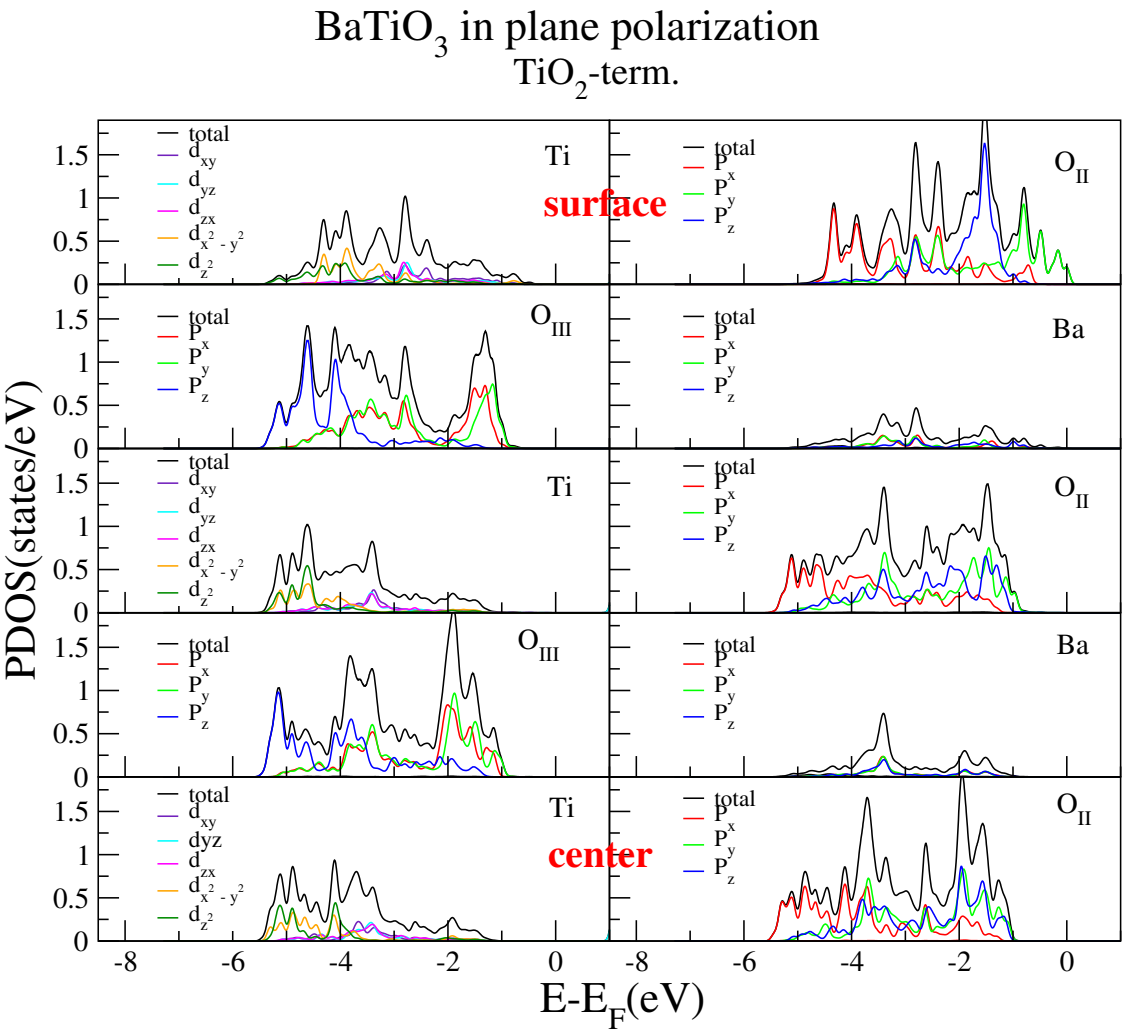

Figure 4.10: Partial densities of states (PDOS) of a TiO_2 terminated symmetric 9 layer film of $BaTiO_3$ with in plane polarization.

the A_2O_2 model, positions of atoms at the inner layer are the same as the perovskite positions. In the surface layer the O position is $(00z)$ and the A position is $(\frac{1}{2}\frac{1}{2}z)$.

Ti_x stacking faults have a big influence on the $BaTiO_3$ polarization, which can bee seen to increase at stacking the fault region. Unlike the $BaTiO_3$, Ti_x stacking faults enhanced the polarization at stacking the fault region of $PbTiO_3$. Ti_y stacking faults suppress the polarization for both $BaTiO_3$ and $PbTiO_3$, where the decrease in polarization for $PbTiO_3$ is stronger than in $BaTiO_3$. AO stacking faults enhance the polarization for $BaTiO_3$ and $PbTiO_3$,where the enhancement of polarization for $PbTiO_3$ is stronger than in $BaTiO_3$.

.

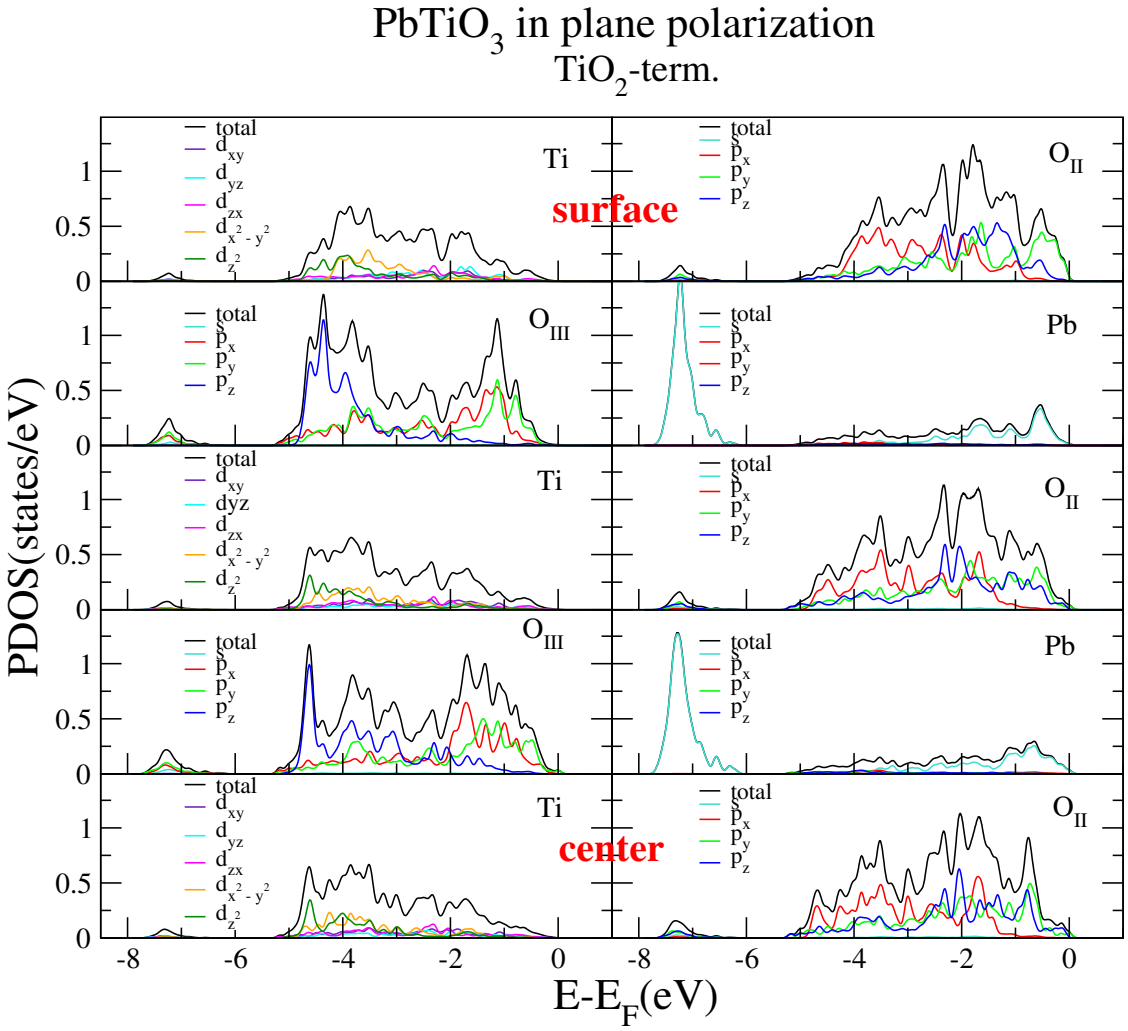

Figure 4.11: Partial densities of states (PDOS) of TiO_2 terminated 9 layers thin film of $PbTiO_3$ with in plane polarization.

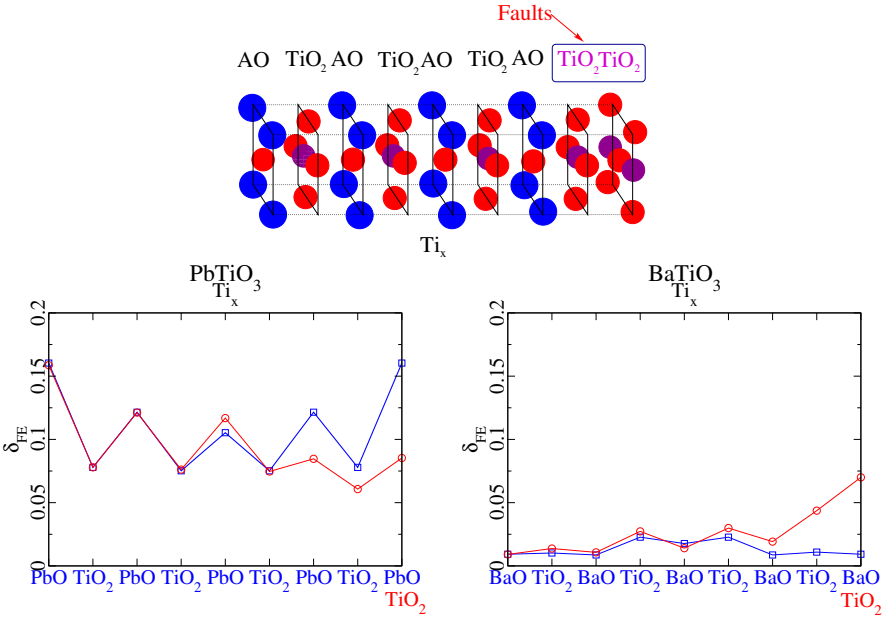

Figure 4.12: Calculated FE distortions, δ_{FE}, for a 9 layer thin films of $PbTiO_3$ (left) and $BaTiO_3$ (right) with (blue) and without (red) stacking faults on the TiO_2-terminated side of the film. In the last layer, Ti was put in x direction.

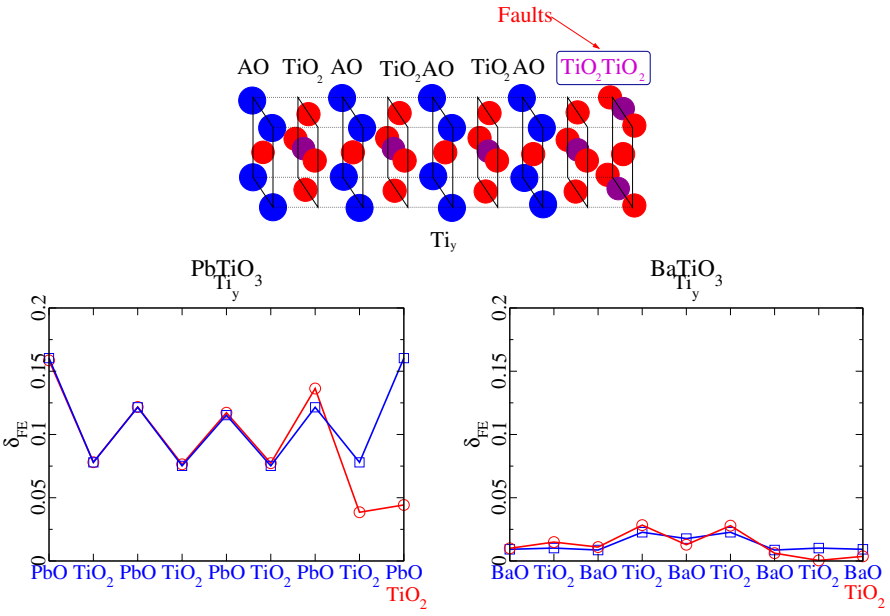

Figure 4.13: Calculated FE distortions, δ_{FE}, for a 9 layer thin films of $PbTiO_3$ (left) and $BaTiO_3$ (right) with (blue) and without (red) stacking faults on the TiO_2-terminated side of the film. In the last layer, Ti was put in y direction.

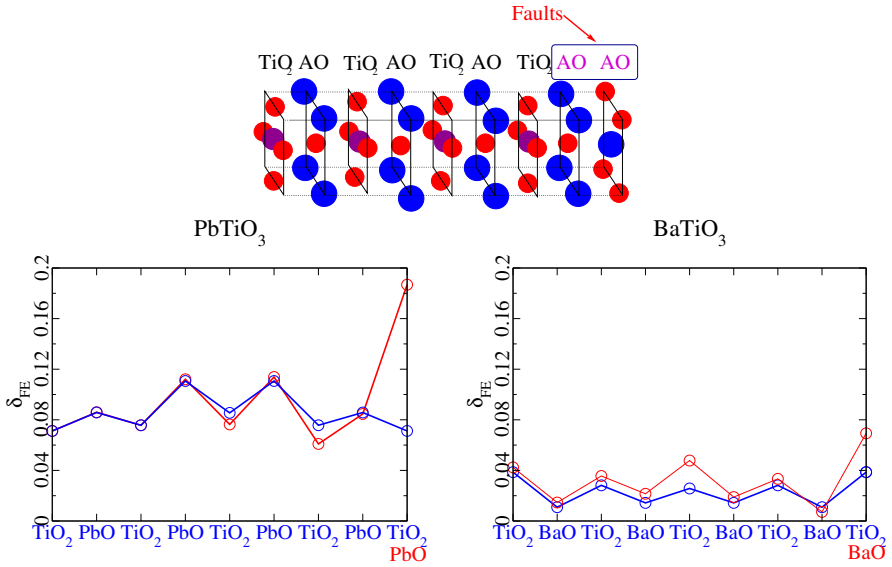

Figure 4.14: Calculated FE distortions, δ_{FE}, for a 9 layer thin films of $PbTiO_3$ (left) and $BaTiO_3$ (right) with (blue) and without(red) stacking faults in the *A*O-terminated side of the film.

5 Out-of-plane polarization of $BaTiO_3$ and $PbTiO_3$ thin films

One of the important fundamental questions for ferroelectric thin films is understanding the stability of a polarization perpendicular to the surface plane, the so-called out-of-plane polarization. An important factor determining the stability of this type of polarization is the compensation of polarization-induced charges on the boundary of sample. Incomplete screening of surface charges results in a depolarization field that opposes the bulk polarization, thereby suppressing ferroelectricity. There have been proposed some methods to screen surface charges: Surface charges can be screened by two metallic electrodes that sandwich the ferroelectric material [105–107] or the formation of equilibrium stripe domains with oppositely oriented polarization [108]. Recently a new mechanism for screening of surface charges by atomic and molecular adsorbates has been proposed [45, 109, 110]. Out-of-plane polarization has been stabilized for $BaTiO_3$ nanostructures by molecular hydroxyl(OH) and carboxylate (R-COO) adsorbates [45].

5.1 Basic electrostatics

Determining whether a thin film with an out-of-plane polarization is stable or not is a subtle problem, much more delicate than the situation of a polarization parallel to the surface described in Section 4.2.2. The first step to gain some insight into this problem was taken by simulating free-standing slabs with a polarization perpendicular to the surfaces. We choose the surface normal $\hat{n}$ to be parallel to the z axis, and we assume the charge density $\rho(r)$ of the slab to be periodic in the x and y directions.

$$m = \int_{-\infty}^{\infty} \bar{\rho}(z) z dz \tag{5.1}$$

The polarized slab exhibits an electric dipole moment parallel to the surface normal $\hat{n}$, where $\bar{\rho}(z)$ is the planar averaged charge density

$$\bar{\rho}(z) = \frac{1}{A} \iint_A \bar{\rho}(r) dx dy \tag{5.2}$$

and A is the area of the surface unit cell. The electrostatic potential $v(r)$ experienced by the electrons can be calculated by solving the Poisson equation

$$\nabla^2 v(r) = -4\pi\rho(r) \tag{5.3}$$

In addition to the microscopic quantities $\rho(r)$ and $\upsilon(r)$, we assume the slabs to be thick enough that macroscopic quantities like the macroscopic electric field E, the dielectric displacement field D, and the polarization P are also well defined inside the slab. In practice, these fields may be calculated, for example, from unit cell averages of the electrostatic potential and the charge density.

In the case of an applied external electric field E_{ext} perpendicular to the surfaces, the dielectric displacement field D inside the slab is oriented parallel to the z axis and is equal to E_{ext}. The boundary condition of a vanishing external electric field is therefore equivalent to a vanishing dielectric displacement field D inside the slab. fig. 5.1(a) shows a schematic picture of the planar-averaged potential $\bar{v}(r)$ for this situation. The potential is constant outside the slab, but due to the slab dipole moment m the potential drops by $4\pi em$ when going from one side of the slab to the other. At the same time, the polarization P leads to surface charges $\sigma = P \cdot \hat{n}$, which give rise to a huge depolarization field $E = D - 4\pi P = -4\pi P$ inside the slab. (Notice, that E does not depend on the thickness of the slab). The contribution of the depolarization field to the total energy is large enough to completely destabilize the bulk FE state. Therefore, relaxing a polarized slab under the boundary condition of a vanishing external electric field will inevitably result in a paraelectric cubic structure [111].

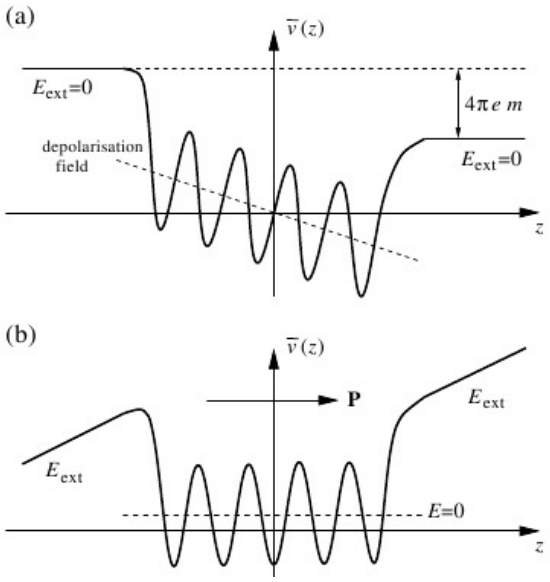

Figure 5.1: Schematic illustration of the planar-averaged potential $\bar{v}(z)$ for an isolated slab with a dipole moment m perpendicular to the surface. (a) Vanishing external electric field (equivalent to $D = 0$). (b) Vanishing internal electric field ($E = 0$). Taken from Ref [111].

A comparison with the situation in an infinitely extended crystal shows which boundary conditions have to be used instead. In DFT calculations for bulk systems, periodic boundary conditions for the electrostatic potential are usually applied. In this case, the internal electric field E vanishes, even in the presence of a spontaneous

polarization P_s^{bulk}, whereas the dielectric displacement field D will be nonzero. In analogy, a slab is in a FE state with spontaneous polarization P_s if a situation exists where the internal electric field E is zero, but the dielectric displacement field D is nonzero. However, an external electric field $E_{ext} = D = 4\pi P_s$ will then appear outside the slab, as shown in fig. 5.1 (b). In our calculations we are able to control only the external electric field E_{ext} but not the internal field E. So to study whether a slab shows a FE instability we have to apply external electric fields of different strength and search for the situation where $E = E_{ext} - 4\pi P$ is zero. A rough estimate of how large E_{ext} will be in this situation can be made if we assume that the polarization of the slabs is equal to the bulk spontaneous polarization P_s^{bulk} [111]. By using the Berry phase approach, we have calculated the bulk spontaneous polarization of $BaTiO_3$ and $PbTiO_3$ to be $4.64 \times 10^{-3}\ e/\mathrm{bohr}^2$ and $15.35 \times 10^{-3}\ e/\mathrm{bohr}^2$, respectively [112]. This translates to external electric fields of 0.0585 a.u. and 0.1949 a.u. (An electric field of 1 a.u. corresponds to $5.14 \times 10^9\ \mathrm{V/cm}$ and a polarization of $10^{-3}\ e/\mathrm{bohr}^2$ equals $5.72\mu C/\mathrm{cm}^2$.)

5.2 $BaTiO_3$ surfaces in external electric fields

In order to find polarization of slabs, an external field (E_{ext}) should be found for which the internal field (E_{int}) in the is zero. For calculating E_{int}, a natural way to compute E would be to determine the gradient of the macroscopically averaged electrostatic potential $v(r)$. Unfortunately, it turned out that 7-9 layers are not enough to give accurate macroscopic averages (the uncertainties in the gradients were much too large). Instead, we calculated the internal electric field by using the relation $E_{int} = E_{ext} - 4\pi P$. The polarization P can be deduced either from the surface charge σ or from the dipole moment m and the thickness d of the slabs:

$$P = \sigma, \quad P = m/d. \tag{5.4}$$

The dipole moment m is directly given by the charge distribution of the slabs via Eq.5.1. For the thickness d we took the distance between the centers of gravity z_0 of the screening charge distribution of the top and bottom surfaces of our slabs. (For a metal, z_0 is the position of the surface image plane from which the classical image potential is measured.) The screening charge distribution is given by the difference of the charge densities calculated with and without an external electric field, for the $\bar{\rho}^{scr}(z)$ we used the pseudo-charge explained in the section 3.5. A typical planar-averaged screening charge distribution $\bar{\rho}^{scr}(z)$ is shown in fig.5.2 a,b. As expected, a positively oriented electric field pushes the electrons into the slab at the top surface and pulls them out at the bottom (where it can be interpreted as a negatively oriented field). From fig.5.2 a, b, we see that the screening charge piles up directly at the surface and is mainly confined above the surface atoms. These surface charges are responsible for the screening of the external electric field. Inside the slab, fairly large oscillations are found that are associated with the remaining internal electric field or

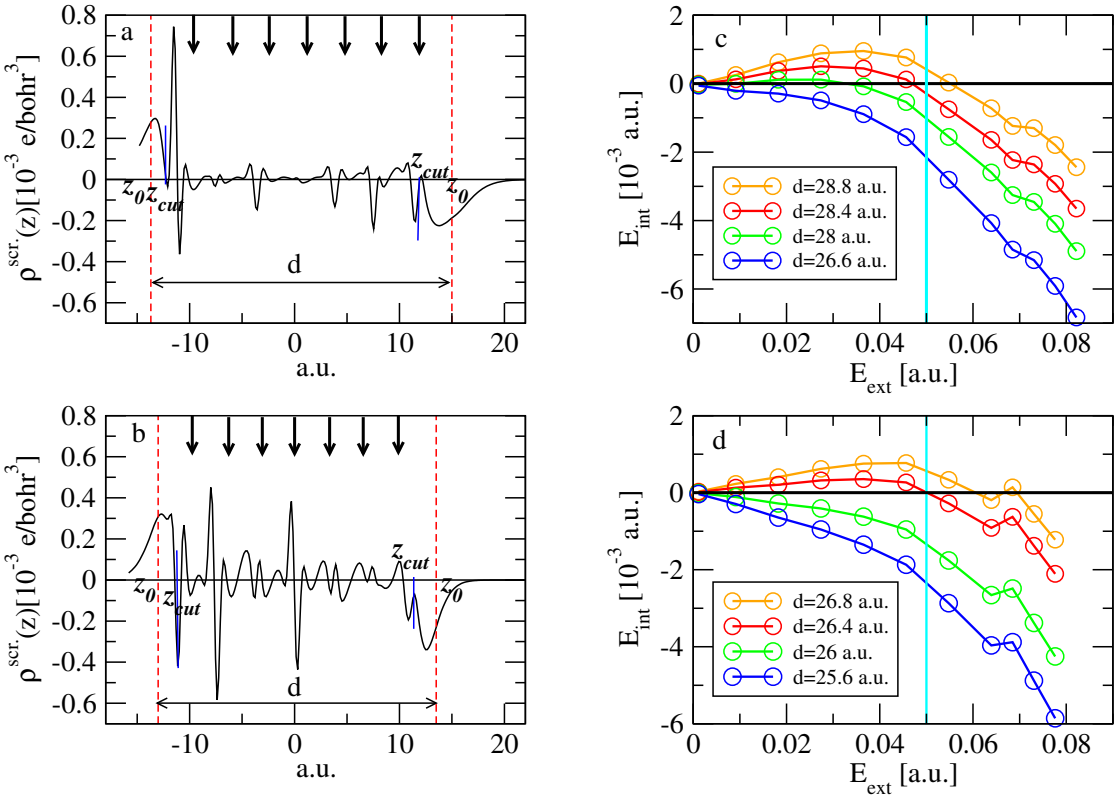

Figure 5.2: (a) and (b) show planar-averaged screening charge distribution of a BaO and TiO_2 terminated of $BaTiO_3$ films respectively, calculated from a seven-layer slab for an electric field of $E_{ext} = +0.018$ a.u. The arrows indicate the positions of the atomic planes. The z_{cut} is the position where the extrapolation of the first charge peak goes to zero. (c) and (d) present internal electric field E_{int} in the fully relaxed seven-layer slab as a function of the applied external electric field E_{ext} for a BaO and TiO_2 terminated film of $BaTiO_3$, respectively. The turquoise blue lines indicate the bulk polarization of the $BaTiO_3$.

come from the non-uniqueness of the pseudo-charge inside the muffin-tin region. The surface charge σ and the center of gravity of the screening charge distribution z_0 for the top surface of the slab are given by

$$\sigma = \int_{z_{cut}}^{c_0} \bar{\rho}^{scr}(z)dz, \quad z_0 = \frac{1}{\sigma}\int_{z_{cut}}^{c_0} \bar{\rho}^{scr}(z)dz. \tag{5.5}$$

For z_{cut} we have taken the position where the extrapolation of the first charge peak goes to zero (cf. fig.5.2 a,b) but the results are very sensitive to the choice of z_{cut}. The use of relation $E_{int} = E_{ext} - 4\pi P$ involves the difference of two relatively large numbers, so that the result for internal electric field very sensitively on details of the calculation. In particular, the determination of thickness d of slab is very critical. E_{int} as a function of E_{ext} for $BaTiO_3$ (BaO and TiO_2 terminated) with different d has been calculated (cf. fig.5.2 c,d). The spontaneous polarization of the slab is corresponds to a E_{ext}, so that $E_{int}(E_{ext}) = 0$. But the (nontrivial) zero point of E_{int} strongly depends on d. Since the calculation of the d values is not possible exactly, the polarization of the slab can not be estimated accurately with this method.

5.3 Out-of-plane polarization stabilized by external electric fields

In this section, the behavior of the ferroelectric distortion (δ_{FE}) at the different layers of thin films has been investigated. $BaTiO_3$ and $PbTiO_3$ (AO and TiO_2 terminated films) are considered. We construct a p(1×1) thin film with 9 layers thickness. For $BaTiO_3$ thin films, an external field of 0.055 a.u. has been applied. This field translates to spontaneous polarization of the slab of $P_s = 4.0 \times 10^{-3} e/\mathrm{bohr}^2$, which corresponds roughly to the bulk spontaneous P_s^{bulk} of $BaTiO_3$. With this external field, δ_{FE} in the central layers is the same as the bulk. The calculated values of ferroelectric distortion (δ_{FE}) for $BaTiO_3$ (BaO and TiO_2 terminated film) with and without applying the external field are shown in fig. 5.3. In the case of no external field, the depolarization field has destroyed the polarization and the ferroelectric distortion represents the relaxation effect. The relaxation for TiO_2-terminated is bigger than BaO_2-terminated. When the external field (0.055 a.u.) is applied the ferroelectric distortions at the central layers are as same as ferroelectric distortion in the bulk. The ferroelectric distortion of the surfaces layers depend on the direction of relaxation effect. According to the polarization and relaxation effect to be in the same or opposite directions, the ferroelectric distortions at the TiO_2-terminated surfaces are enhanced or suppressed respectively. For the BaO-terminated thin film, the relaxation has no influence on the ferroelectric distortions, when it has opposite direction to the polarization. This is not surprising because we have seen that there is no strong bonding between Ba and O (cf. section 1.1.1).

The case of $PbTiO_3$ is different to $BaTiO_3$. The bulk spontaneous polarization for $PbTiO_3$ is $P_s = 15.35 \times 10^{-3} e/\mathrm{bohr}^2$. In order to reach this polarization at the

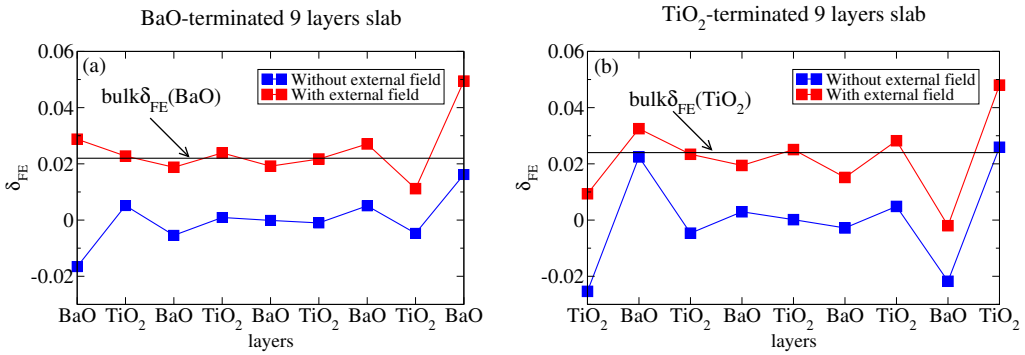

Figure 5.3: (a) Calculated ferroelectric distortion (δ_{FE}) for BaO terminated $BaTiO_3$ in an external electric field. Blue and red corresponded to zero and 0.055 a.u. external field, respectively.(b) Calculated ferroelectric distortion (δ_{FE}) for TiO_2 terminated BaTiO in 0.055 a.u. external field. The black line indicates the bulk ferroelectric distortions for BaO and TiO_2 layers respectively.

central layers of the $PbTiO_3$ thin films, an external electric field of 0.1949 a.u. is required. We have a limitation of 0.094 a.u. for applied external fields. If the external field would be bigger than this limitation, the charges in the slab penetrate to the vacuum region. The $PbTiO_3$ slabs with 0.065 a.u. external field are considered, which corresponds roughly to 1/3 of the bulk spontaneous polarization of $PbTiO_3$. The calculated values of ferroelectric distortion (δ_{FE}) for $PbTiO_3$ (PbO and TiO_2 terminated film) with and without applying the external field are shown in fig. 5.4. The behavior of the ferroelectric distortion for the TiO_2-terminated of $PbTiO_3$ is similar to the TiO_2-terminated of $BaTiO_3$. For the PbO-terminated thin film the relaxation has more influence on the ferroelectric distortions than for the BaO-terminated one, in case it has opposite direction to the polarization. The bonding between Pb and O is stronger than bonding between than Ba and O.

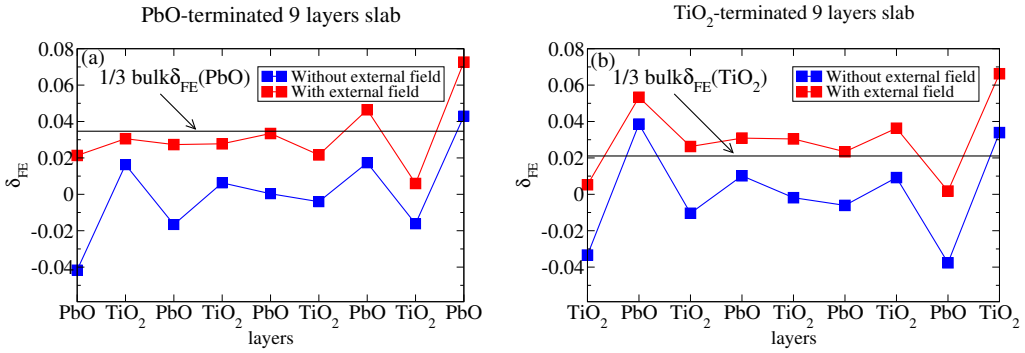

Figure 5.4: (a) Calculated ferroelectric distortion (δ_{FE}) for PbO terminated $PbTiO_3$ in an external electric field. Blue and red corresponded to zero and 0.065 a.u. external field, respectively.(b) Calculated ferroelectric distortion (δ_{FE}) for TiO_2 terminated BaTiO in 0.065 a.u. external field. The black line indicates the 1/3 bulk ferroelectric distortions for BaO and TiO_2 layers left and right.

5.3.1 Electronic structure

In this section the influence of different directions of out-of-plane polarizations, i.e. outward and inward (P^+ and P^-), at the surface on the partial densities of states is investigated. Figures 5.5 to 5.8 depict the partial densities of states (PDOS) of $PbTiO_3$ thin films, where both PbO and TiO_2 termination for both directions of out-of-plane polarizations (outward and inward) at the surfaces are considered. The PDOS for both valence and conduction band at the central layers are similar to the bulk, but at the surfaces we see a different behavior in the valence band region. All states of the O and Pb at the PbO-terminated surface with inward polarization are slightly shifted to higher energy. All states of the O and Pb at the PbO-terminated surface with outward polarizations are slightly shifted to lower energy. The densities of state in the inner layers of the PbO-terminated films for both polarizations are the same (cf. fig. 5.5 and fig. 5.6). The p_y state of O at the TiO_2-terminated surface with inward polarization is shifted toward the Fermi level(fig. 5.7). The p_z state of O at the TiO_2-terminated inner layer of outward polarizations is shifted to lower energy(cf. fig. 5.8).

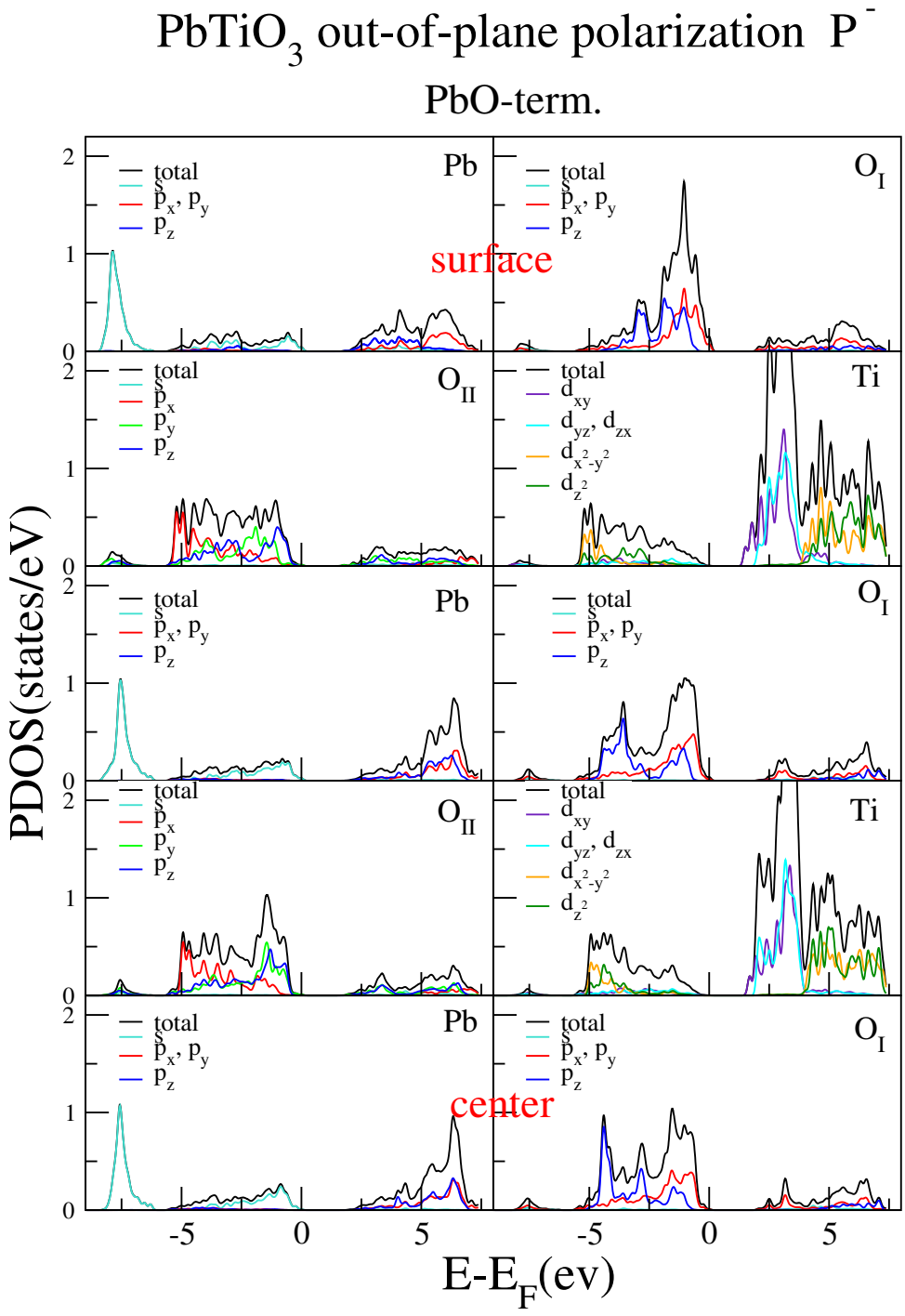

Figure 5.5: Partial densities of states (PDOS) of $PbTiO_3$ (PbO-termination) with out-of-plane polarization P^-. P^- means that in each surface layer anions are on top (larger z) of cations. The top set to the bottom set of panels show the partial densities from states of surface atoms to middle layer atoms.

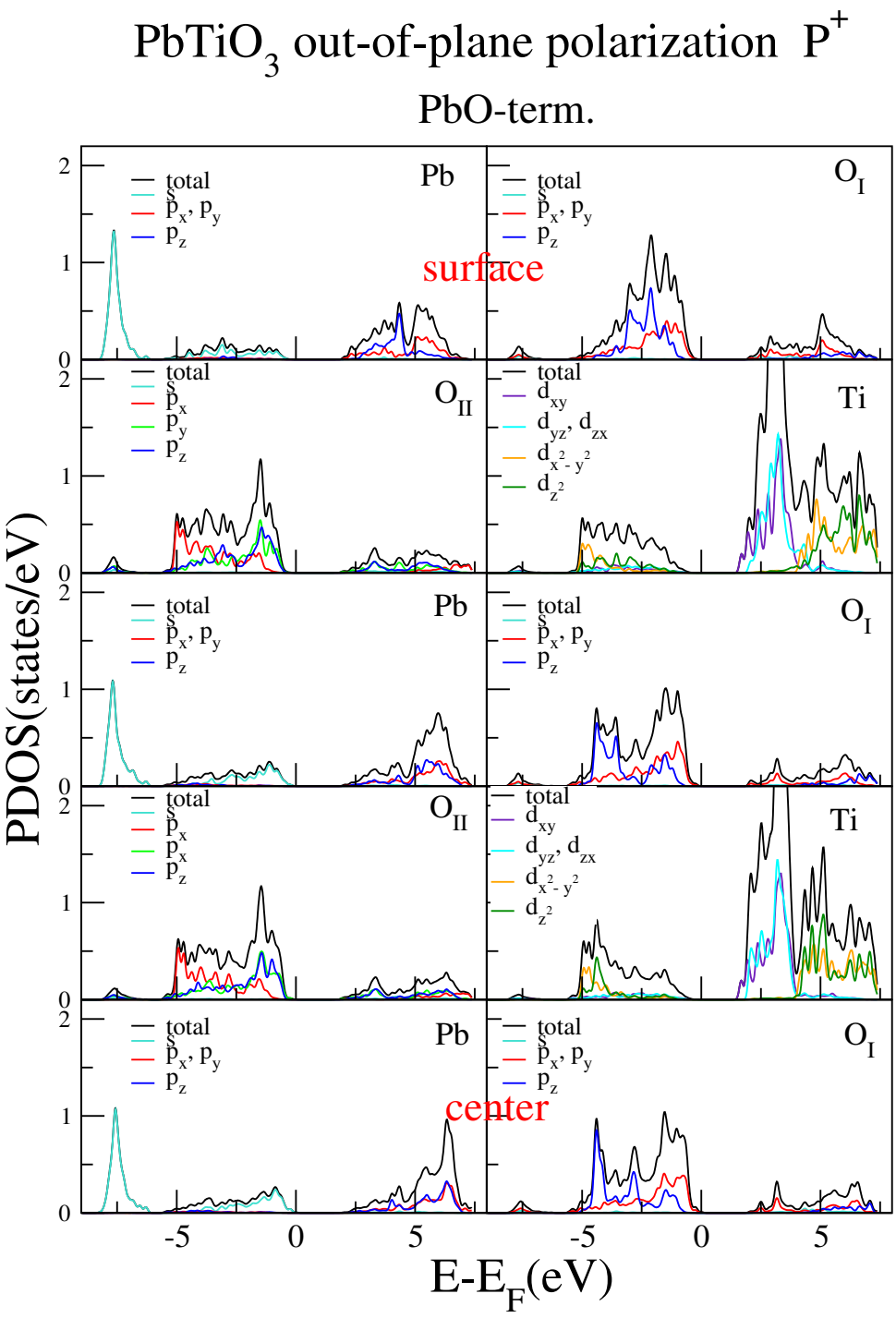

Figure 5.6: Partial densities of states (PDOS) of $PbTiO_3$ (PbO-termination) with out-of-plane polarization P^+. P^+ means that in each surface layer cations are on top (larger z) of anions. The top set to the bottom set of panels show the partial densities from states of surface atoms to middle layer atoms.

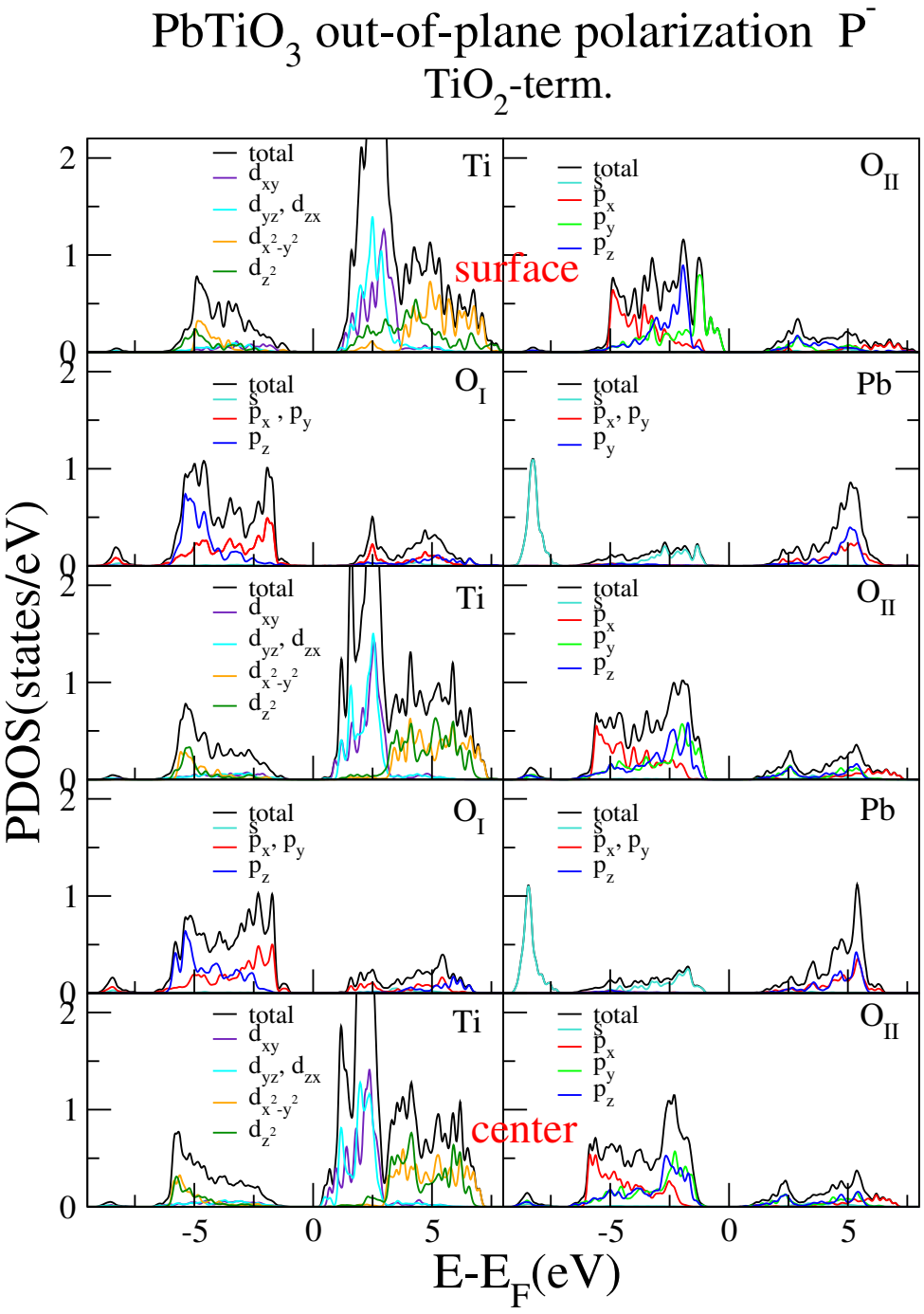

Figure 5.7: Partial densities of states (PDOS) of $PbTiO_3$ (TiO_2-termination) with out-of-plane polarization P^+. P^+ means that in each surface layer anions are on top (larger z) of cations. The top set to the bottom set of panels show the partial densities of states from surface atoms to middle layer atoms. p_y at the surface is shifted to higher energy.

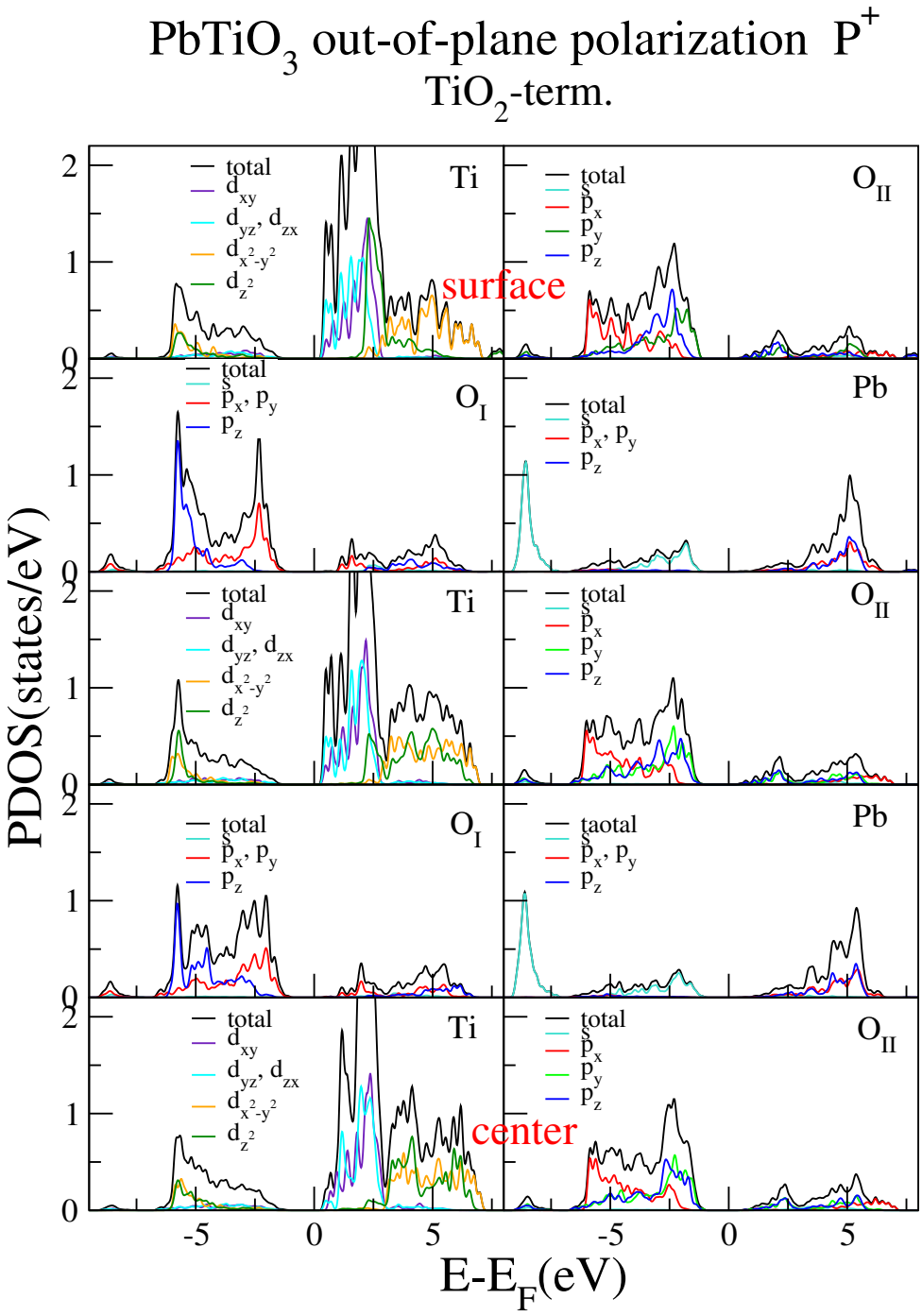

Figure 5.8: Partial densities of states (PDOS) of $PbTiO_3$ (TiO_2-terminated) with out-of-plane polarization P^+. P^+ means that in each surface layer cations are on top (larger z) of anions. The top set to the bottom set of panels show the partial densities of states from surface atoms to middle layer atoms.

5.4 Out-of-plane polarization stabilized by defects

Stabilization out-of-plane polarization is technologically very important for nanostructured perovskite-based oxides. One experimental study has shown that out-of-plane polarization can be stabilized for a $BaTiO_3$ nanostructure by molecular hydroxyl (OH) and carboxylate (R-COO) adsorbates [105]. Another one has shown that high or low oxygen partial pressure induces outward or inward polarization, respectively, in an ultrathin $PbTiO_3$ film [109].

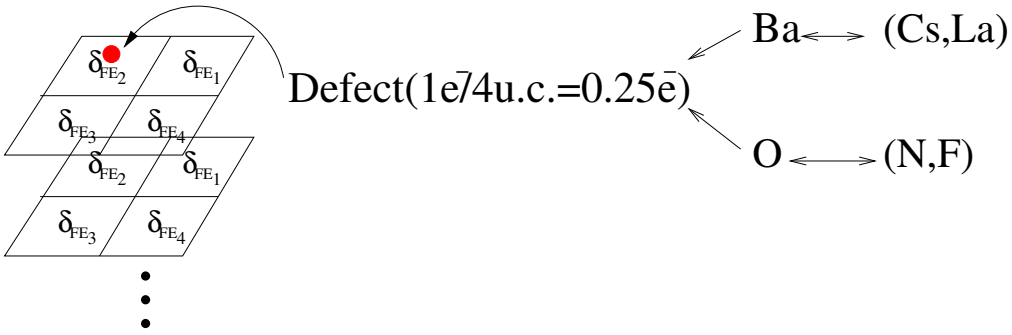

Figure 5.9: Schematic illustration of different types of defect on a p(2×2) surface of BaO terminated $BaTiO_3$. Different ferroelectric distortion can occur in the 4 unit-cells of the p(2×2) structure ($\delta_{FE_1} - \delta_{FE_4}$). Ba can be replaced by Cs or La, O by N or F.

We have done DFT calculations to investigate the how an out-of-plane polarization for $BaTiO_3$ and $PbTiO_3$ can be stabilized. A significant surface charges density of about 0.25 electronic charges per unit cell area is required to stabilized the bulk like out-of-plane polarization for $BaTiO_3$. The stabilization is simulated in a p(2×2) surface geometries. To compensate 0.25 electronic charges per unit cell area, for a p(2×2) surface $1e^-$ is needed. If each oxygen ion accept -2e and each barium cation donor +2e, in one side 1/2 oxygen and other side 1/2 barium vacancy are needed. To this end ' 1/2 oxygen vacancy' (O is replaced by F or Ba by Cs) and '1/2 Ba vacancy' (O is replaced by N or Ba by La) are created. An average ferroelectric distortion,

$$\delta_{FE}(Defect) = \frac{1}{4}\sum_{i=1}^{4}\delta_{FE_i}\ , \tag{5.6}$$

withδ_{FE} from each part of the layers was calculated. We have shown the average of δ_{FE} from each layer in fig. 5.9. We have figured out that with this type of defects stabilization of out-of-plane polarization is possible. Different types of defects have very similar influence on the polarization of the central layers (cf. fig. 5.10).

A significant surface charge density of about 0.81 electronic charges per unit cell area is required to stabilized the bulk like out-of-plane polarization for $PbTiO_3$. In this work out-of-plane polarizations for $PbTiO_3$ slabs are stabilized by 0.5 or 0.25

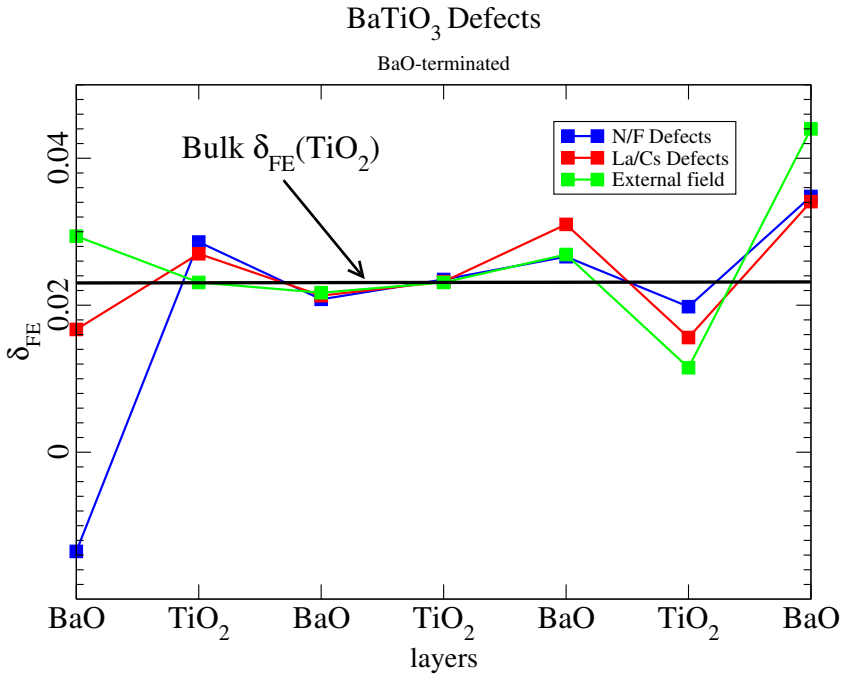

Figure 5.10: Calculated ferroelectric distortion (δ_{FE}) for a BaO terminated $BaTiO_3$ film with out-of-plane polarization and different types of defects on the surface and external electric fields (E_{ext}=0.0585 a.u.) . The black line indicates the bulk ferroelectric distortion for the TiO_2 layer.

electronic charges per unit cell area. The stabilized ferroelectric distortions in the central layers of the thin films, are nearly equal to 1/2 and 1/3 bulk ferroelectric distortions for 0.5 and 0.25 electronic charges per unit cell area respectively(cf. fig. 5.11). To compensate 0.50 electronic charges per unit cell area, 2e per p(2 $\times$ 2) surface or 1e per c(2 $\times$ 2) surface are needed. To this end an oxygen vacancy on one side and a Pb vacancy (or substitute O with C) on other side of a thin film with p(2 $\times$ 2) surface have to be put. Alternatively 1/2 oxygen vacancy (substitute O with F) on one side and 1/2 Pb vacancy (substitute O with N) on other side of a thin film with c(2 $\times$ 2) surface can be used. To compensate 0.25 electronic charges per unit cell area, for a p(2$\times$2) surface 1e is needed. To this end 1/2 oxygen vacancy (O is replaced by F) and 1/2 Pb vacancy (O is replaced by N) are created.

We conclude that with different types of defects the out-of-plane polarization for ferroelectric material, can been stabilized. The manipulating and switching of the polarization of ferroelectric thin films is possible by controlling the defect concentration on the surfaces.

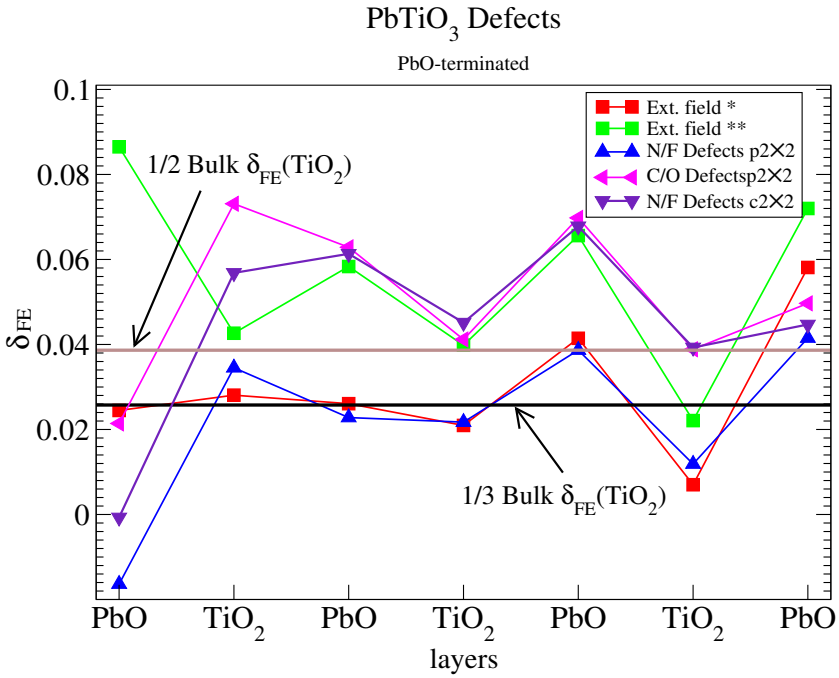

Figure 5.11: Calculated ferroelectric distortion (δ_{FE}) for $PbTiO_3$ PbO terminated with different type of defects on different surface and external electric fields.*E_{ext}=0.0583 a.u. corresponded to 1/3 bulk polarization. **E_{ext}=0.0934 a.u. corresponded to 1/3 bulk polarization. The black and brown line indicate the 1/3 and 1/2 bulk ferroelectric distortions of the TiO_2 layer respectively.

6 Domain walls

The performance of ferroelectric thin films devices depends strongly on the magnitude and stability of the switchable ferroelectric polarization of the ferroelectric layer. The polarization switching is realized by nucleation and growth of polarization domains under an external electrical field [113, 114]. To this end, the properties of the domain walls, in particular their structure, width and mobility, are important parameters. In the bulk ferroelectrics, the paraelectric to ferroelectric phase transition is accompanied by the formation of polarization domains to minimize the system energy with respect to the depolarization field and mechanical strain. If e.g. a domain wall forms in a (100) plane six equivalent cubic (100) directions that can be chosen as directions. For the polarization dipoles in the $PbTiO_3$, both 90° and 180° domain walls occur, where, on passing the wall from one domain to the other, the polarization vector changes direction by about 90° and 180°, respectively.

For ferroelectric domain walls in $BaTiO_3$, $PbTiO_3$ there are several experimental [108, 115, 116] and theoretical studies [41, 117–120]. Recently, it has been shown [121, 122] that using high-resolution transmission electron microscopy (HRTEM) atomic resolution even of oxygen atoms can be achieved by a novel technique called negative spherical-aberration (C_s) imaging in a C_s-corrected transmission electron microscope. This technique have been used to investigate the atomic details and dipole distortions on an atomic scale near 180° domain walls in thin epitactic films of $PbZr_{0.2}Ti_{0.8}O_3$ sandwiched between two $SrTiO_3$ layers and prepared by pulsed laser deposition [49]. These images showed two possible 180° domain walls (transversal and longitudinal) and enabled to investigate the atomic positions.

6.1 Transversal domain walls

Previous DFT studies on 180° traversal domain wall of $PbTiO_3$ considered mainly [100]-oriented 180° domain walls [41, 123]. Pöykkö and Chadi have shown that the [110]-oriented 180° domain wall of $PbTiO_3$ is slightly higher in energy than the [100]-oriented one [123]. But the [110]-oriented 180° domain is more favorable to observation HRTEM measurements [49].

We studied [110]-oriented 180° domain walls of $PbTiO_3$ by DFT calculations. For the simulation of this type of domain wall, we have used supercells consisting of $N \times 1 \times 1$ perovskite unit cells stacked in the [1-10] direction and containing one up and one down domain, each $N/2$ lattice constants wide, as shown in fig. 6.1(b). We take the domain wall to lie in the [110] plane and the polarization to point in the [001]

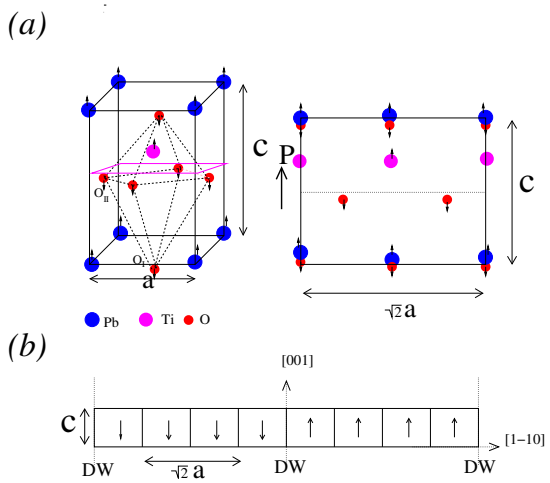

Figure 6.1: (a) Schematic perspective view of the unit cell of ferroelectric $PbTiO_3$ and (b) its projection along the $[\bar{1}10]$ direction; Arrows indicate atomic displacements, supercell geometries containing six unit cells 180° domain walls;In (b) atoms are omitted and only solid lines connecting the Pb atoms are drawn. Supercell boundaries are indicated by dotted lines.

investigate

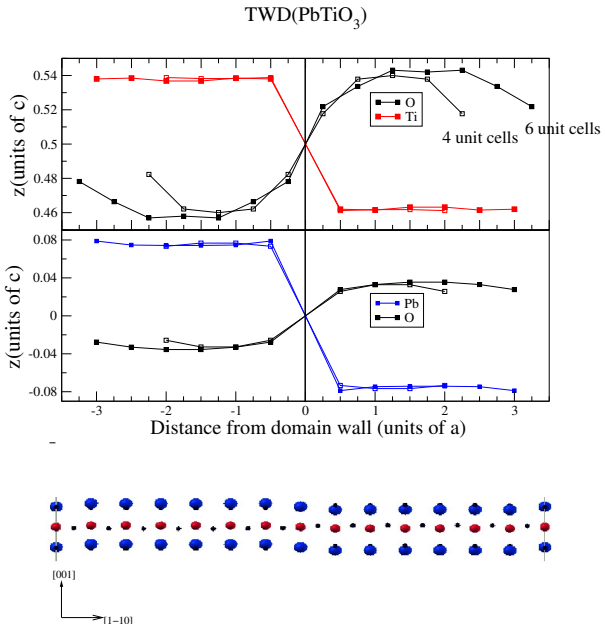

Figure 6.2: Displacements in z-direction of the atoms relative to the Pb atom in a Pb-centered 180 domain wall as a function of the distance to the wall, calculated using different supercell sizes.

(z) direction. Supercells with N, 4 and 6 were employed (cf. fig. 6.1), containing 50 and 70 atoms, respectively. The dimensions of the supercells were kept fixed at the theoretical equilibrium lattice constants computed for the bulk tetragonal phase (cf. 4.2).

Fig.6.2 shows the atomic displacements in z-direction relative to the Pb ion in the domain wall.

The results do not depend sensitively on the size of the suppercell (N). It can be seen that the domain wall is extremely narrow. The with of domain wall for Pb and Ti is $a\sqrt{2}/2$ and for O is $a\sqrt{2}$ (just one projected unit cell). The difference of the position of two Pb atoms in both sides of the domain walls is around 0.62Å this jump can also clearly be seen on the HRTEM image (cf. fig. 6.3) There is no qualitative difference between the our calculation and experimental results [49].

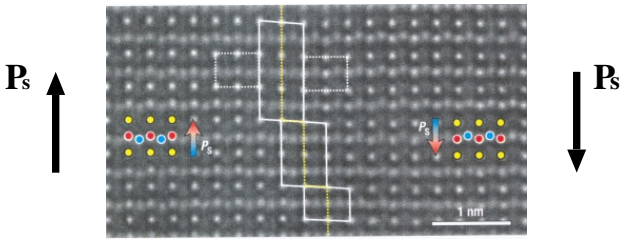

Figure 6.3: Images of $[\bar{1}10]$ domain-wall. A narrow domain wall seen edge-on. The arrow P_s indicate the opposite polarization directions across the domain wall. The parallelograms denote the segments of TDW. The yellow dotted line marks the central plane of the domain wall.The white dotted lines trace projected unit cells on either side of the domain wall. Taken from Ref. [49]

6.2 Longitudinal domain walls

We simulated longitudinal domain walls (LDW) normal to the [001] direction of $PbTiO_3$ by DFT calculations. For simulation of these types of domain walls, we construct a 60-atom supercell by arranging six c(2×2) unit cells of the bulk tetragonal $PbTiO_3$ in an $\sqrt{2}a \times \sqrt{2}a \times 6a$ supercell.

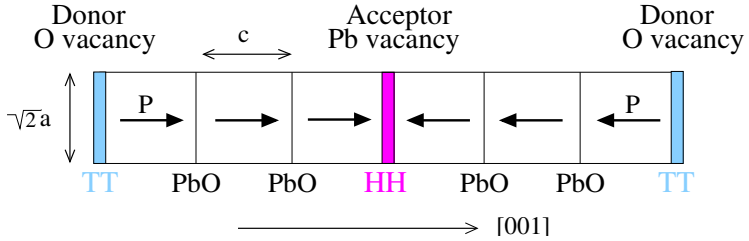

Figure 6.4: Schematic view of a $PbTiO_3$ ferroelectric supercell in which head-to-head (HH) and tail-to-tail (TT) 180° domain walls coincide with acceptor (Pb vacancy) and donor (O vacancy) defects layers, respectively.

The initial atomic coordinates are chosen to be those of the relaxed bulk ferroelectric structure with polarization in the [001] direction throughout the supercell(3 unit cells upward and 3 unit cells downward). The bulk polarization of the $PbTiO_3$ is $15.35 \times 10^{-3} e/\text{bohr}^2$. The polarization induces +1.65 e and -1.65e bound charges per unit-cell on the head-to-head(HH) and tail-to-tail(TT) domain walls, when we form a longitudinal domain wall with bulk polarization. The bound charges make domain walls metallic (cf. fig. 6.5) and also a unfavorable due to electrostatic energy. In this cases the domain wall is not stable and after relaxation the polarization of the domains is destroyed. To stabilize longitudinal domain walls, donor and acceptor charges on the HH and TT are required. For a c(2×2) longitudinal domain wall to stabilize bulk polarization -3.3e and +3.3e on the HH and TT are needed. We studied longitudinal domain walls with 3 and 2 electrons acceptor/donor charges at the HH/TT domain wall. The 3e and 2e correspond to the charges inducted by 91% and 60% of the bulk polarization in the c(2×2) unit cells at the HH/TT domain wall.

Each oxygen ion accepts -2e and each lead cation donates +2e. To create a 3e acceptor/donor, we have to create 3/2Pb and 3/2O vacancy on the HH and TT domain walls. A 3/2Pb vacancy can be created by one Pb vacancy and substituting O with N. In a similar way one O vacancy and substituting O with F creates a 3/2O vacancy. The supercell has been relaxed along the [001] direction, i.e. , we optimized the internal coordinates the c-axis lattice parameter keeping fixed. Fig. 6.6-a indicates the calculated c-axis lattice parameter for each unit cell, which corresponds to the distances between two PbO layers. Fig. 6.6-b shows the displacement from the center of unit cell $(c/2)$ for the O(δ_{O}) and Ti(δ_{Ti}) along the [001] direction for each unit cell. The displacement of the O and Ti, that have a 1.5 unit cell distance to the domain wall (i.e. , they are in the middle of the domain) have maximum value (corresponding to 91% of bulk displacements).

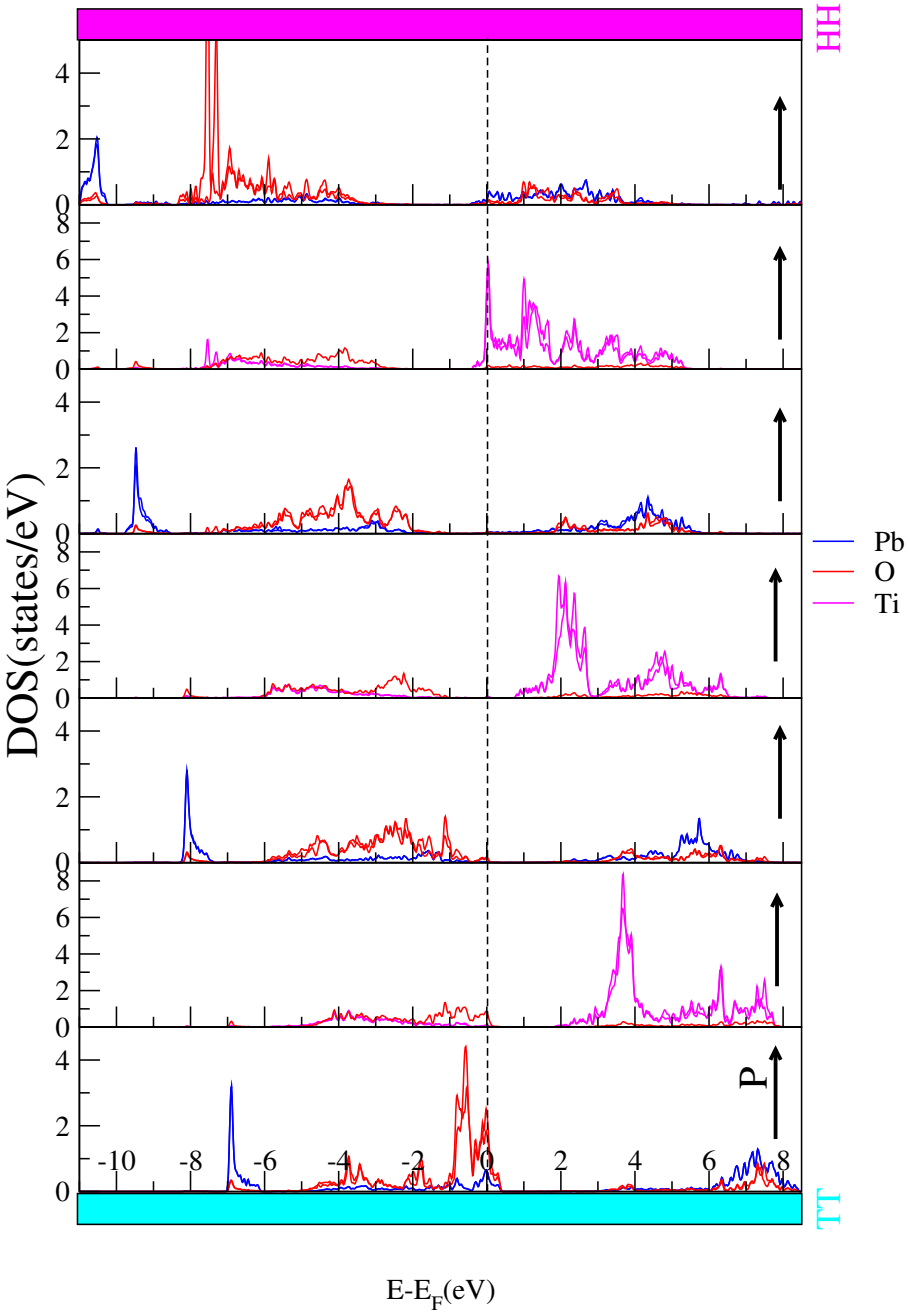

Figure 6.5: Densities of states (DOS) of $PbTiO_3$ longitudinal domain walls without any acceptor/donor in the domain walls. The magenta and cyan colour region indicate domain boundary for head-to-head and tail-to-tail domain walls, respectively.

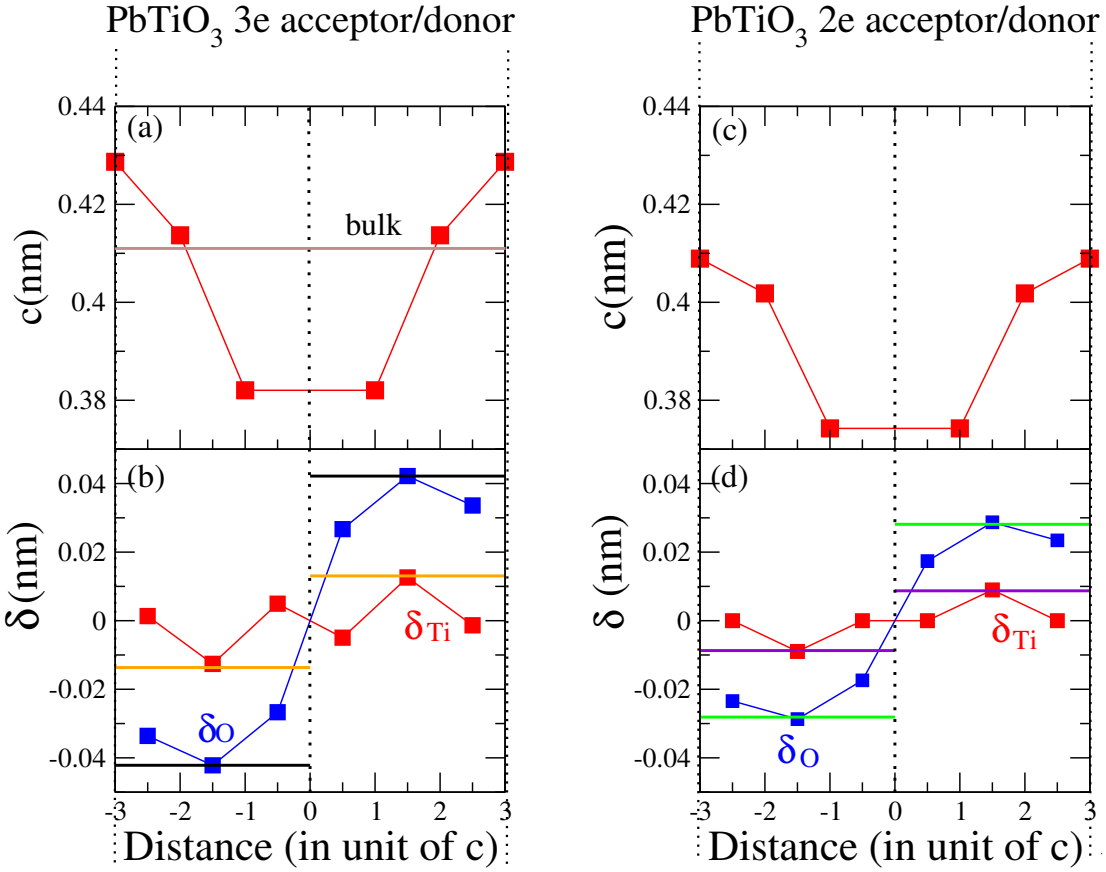

Figure 6.6: (a), (c): Calculated c-axis lattice parameter for each unite cell of $PbTiO_3$ longitudinal domain walls with 3e, 2e acceptor/donor in the domain walls, respectively. (a), (c): Calculated displacement of the Ti and O from the center of the unit cell of $PbTiO_3$ in longitudinal domain walls with 3e, 2e acceptor/donor in the domain walls, respectively. The dotted lines indicate the domain walls. The black and orange lines indicate 91% of the bulk displacements of O and Ti, respectively. The green and violet lines indicate 60% of the bulk displacements of O and Ti, respectively.

To analyze the electronic properties of the relaxed structure, we computed the electronic density of states (DOS). The results, shown in fig. 6.7, indicate that the compensation is successful and the entire supercell is insulating. The bandgap is 1.35 eV(calculated bandgap for the bulk is 1.6 eV). It is typical for DFT calculations to underestimate band gaps by factor of 2 with respect to experiment [124]. The total density of states in the valence band for the titaniums, that are located next to the acceptor and donor layer, move toward and outward to the Fermi level. The density of states for the titanium in the midway between two acceptor/donor layers is same as total density of states of titanium in the bulk (cf. fig. 6.7).

To create a 2e acceptor/donor, we have to create one Pb and one O vacancy in the HH and TT domain walls. The supercell has again been relaxed along the [001] direction, i.e. , we optimized the internal coordinates the c-axis lattice parameter keeping fixed. Fig. 6.6-c indicates the calculated c-axis lattice parameter for each unit cell, which corresponds to the distances between two PbO layers. Fig. 6.6-d shows displacement to the center of unit cell ($c/2$) for the O(δ_{O}) and Ti(δ_{Ti}) along the [001] direction for each unit cell. The displacement of the O and Ti, that have a 1.5 unit cell distance to the domain wall, have maximum value that correspond to the 60% of the bulk displacements.

The experimental investigation on longitudinal domain walls in Pb(Zr, Ti)O_3 (PZT) is shown, the transition of polarization is smooth (6 unit-cell)(cf. fig. 6.8). But our calculations indicate the longitudinal domain walls are narrow (2 unit-cell). This can be interpreted as indication that the defects are not all assembled in a single atomic layer, but rather spread over several layers. Electrostatic interactions might be the driving force for this delocalization.

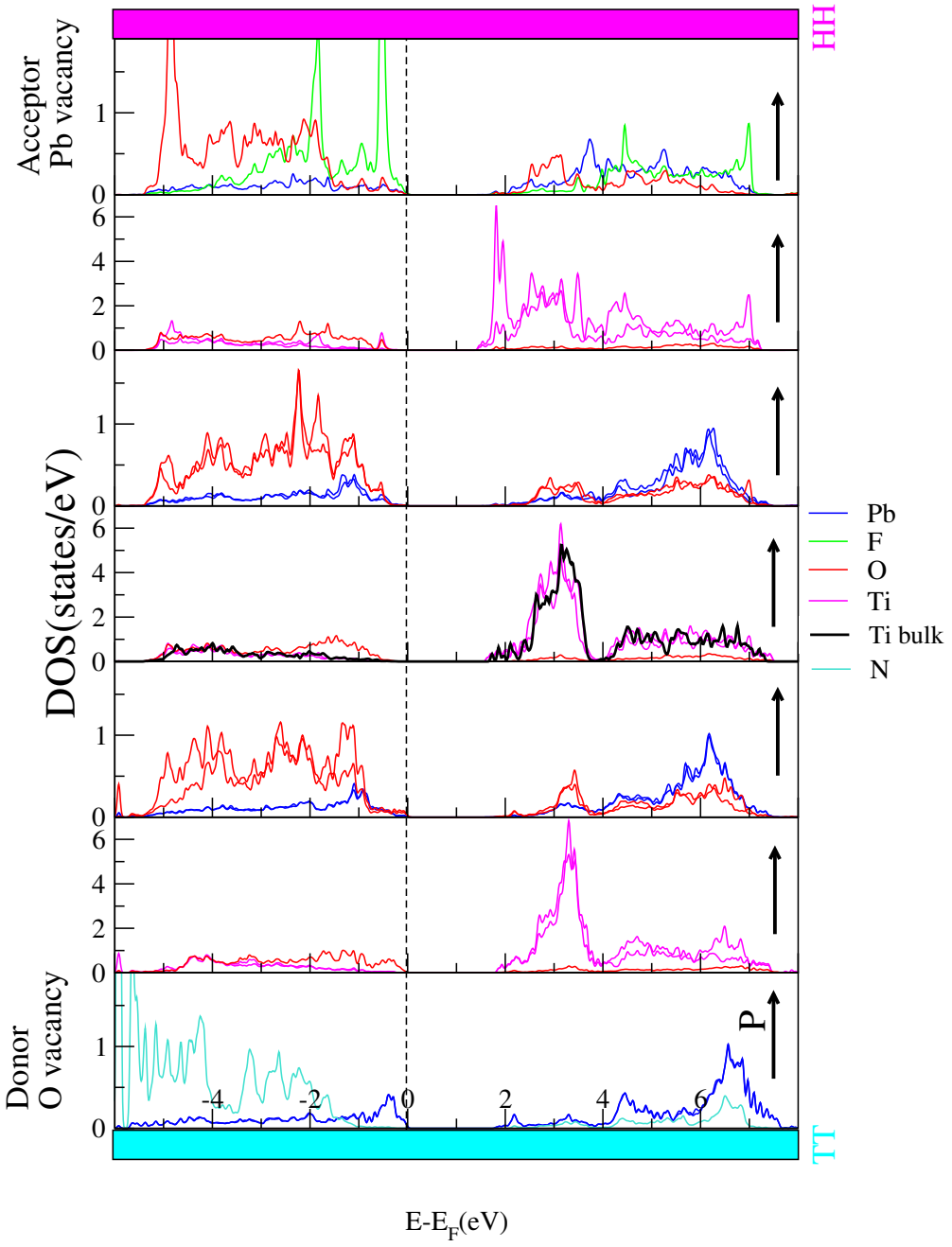

Figure 6.7: Densities of states (DOS) of $PbTiO_3$ longitudinal domain walls with 3e acceptor/donor in the domain walls. The magenta and cyan colour region indicate domain boundary for head-to-head and tail-to-tail domain walls, respectively. The black curve in the middle panel is the Ti DOS as found in the polarized bulk structure of $PbTiO_3$ (fig. 4.4).

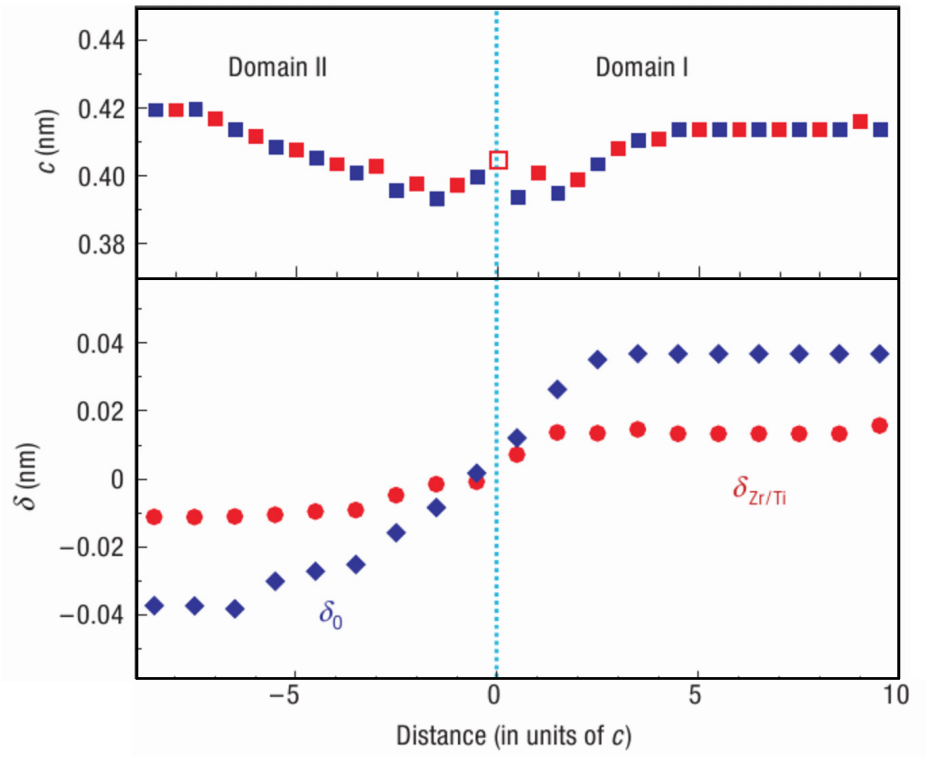

Figure 6.8: top: c-axis lattice parameter in a LDW in PZT. Blue and red squares show the values measured from Pb to Pb atom positions and from Zr/Ti to Zr/Ti, respectively. Bottom: displacements of the Zr/Ti atoms ($\delta_{\mathrm{Zr/Ti}}$) and the O atoms (δ_{O}) across the LDW. Positive values denote upward shifts and negative values downward shifts. Figure taken from Ref. [49]

7 Summary and conclusion

In this thesis, we used density-functional-theory (DFT) to simulate defective structures of the prototypical ferroelectric materials $BaTiO_3$ and $PbTiO_3$. The influence of surfaces, domain boundaries, defects and stacking faults on the ferroelectric behavior were investigated. The stabilization of a polarization perpendicular to the surface plane of $BaTiO_3$ and $PbTiO_3$, and longitudinal domain walls in $PbTiO_3$ have been studied.

As first step, we searched for find reliable exchange-correlation functionals, that can predict the experimental crystal structures and provid understanding of the origin of the difference of the ferroelectric behavior of $BaTiO_3$ and $PbTiO_3$. We calculated crystal structures with different exchange-correlation functionals for those ferroelectric materials. We found that for $BaTiO_3$ the Hedin-Lundqvist parametrization of LDA and, for $PbTiO_3$ the Wu-Cohen form of GGA give best agreement to experimental data.

The electronic structure of $BaTiO_3$ and $PbTiO_3$ were considered: We calculated the partial densities of states (PDOS) for those materials in their cubic and tetragonal geometry. For both materials, all valence states in the ferroelectric tetragonal structure shifted to lower energy in comparison to the paraelectric cubic one, due to the hybridization between O_{II} $2p$ and Ti $3d$. In tetragonal $PbTiO_3$ there is additionally a hybridization between the O_I $2p$ and Pb $6s$ states. This interaction leads indirectly to an increased hybridization between the Ti $3d$ and O $2p$ states, that further stabilizes the ferroelectric state in $PbTiO_3$ as compared to $BaTiO_3$.

As second step, we considered the influence of surface formation and stacking faults on the polarization parallel to the surface plane in $BaTiO_3$ and $PbTiO_3$. We calculated the values of the ferroelectric displacement, δ_{FE}, for both materials and surface terminations. For the PbO-terminated surface of $PbTiO_3$, one can see a clear increase in the average ferroelectric displacements, δ_{FE}, when going from the bulk-like regions to the surface layer. On the other hand, for the TiO_2-terminated surface, the average ferroelectric displacements are slightly decreased at the surface. Surprisingly, this is just the opposite of what is observed for $BaTiO_3$, where a reduction of the ferroelectric displacements for the BaO-terminated surface and a moderate enhancement for the TiO_2-terminated surface can be observed. (Of course, compared to $PbTiO_3$, the ferroelectric displacements are also much smaller for $BaTiO_3$ surfaces, as they are in the bulk.) These results tend to confirm that Pb is a much more active constituent in $PbTiO_3$ than is Ba in $BaTiO_3$.

To analyze the electronic origin of the enhancement/reduction of the polarization at the surface, the partial densities of states have been investigated for $BaTiO_3$ and

$PbTiO_3$ thin films, where both TiO_2 and *A*O terminated surfaces are considered. In the film geometry the PDOS at the central layers are similar to the bulk, but at the surfaces a different behavior can be seen: All states of O at the BaO-terminated surface are shifted to high energy which indicates a decrease in hybridization. Therefore, the ferroelectric (FE) displacement, δ_{FE}, at the BaO-terminated surface layer has been reduced. In contrast to $BaTiO_3$, there is a strong hybridization between O $2p$ and Pb s states at the PbO terminated surface. Thus, the FE displacement at the PbO-terminated surface layer is enhanced. The O p_y state at the TiO_2 terminated surface of $BaTiO_3$ is shifted towards the Fermi level. The PDOS at the TiO_2 terminated surface are not so different to the one of the central layers in the $PbTiO_3$.

Two models of stacking faults for $BaTiO_3$ and $PbTiO_3$ thin films are considered. In the first model, double layers of TiO_2 on one side of the films are formed, while in the second one, we study double layers of *A*O on one side of the films. For the (TiO_2)-double layers model, the positions of atoms at the inner TiO_2 layer are the same as in the unfaulted structure. In the surface layer the positions of O are $(00z)$ and $(\frac{1}{2}\frac{1}{2}z)$ which leave two possibilities for the position of Ti: The first possibility is $(\frac{1}{2}0z)$ (i.e. it lies on the axis of polarization (x)) and the second is $(0\frac{1}{2}z)$ (i.e. it lies on the y axis). The former possibility will be denoted as Ti_x, the latter one as Ti_y. For the (*A*O)-double layers model, positions of atoms at the inner layer are the same as the perovskite positions. In the surface layer the *A*O plane is shifted by $(\frac{1}{2}\frac{1}{2}0)$.

Ti_x stacking faults have a big influence on the $BaTiO_3$ polarization, which can be seen to increase at the stacking fault region. Unlike the $BaTiO_3$, Ti_x stacking faults suppressed the polarization at stacking fault region of $PbTiO_3$. Ti_y stacking faults suppress the polarization for both $BaTiO_3$ and $PbTiO_3$, where the decrease in polarization for $PbTiO_3$ is stronger than in $BaTiO_3$. *A*O stacking faults enhance the polarization for $BaTiO_3$ and $PbTiO_3$, where the enhancement of polarization for $PbTiO_3$ is stronger than in $BaTiO_3$.

As third step, we studied the polarization perpendicular to the surface plane, the so-called out-of-plane polarization in $BaTiO_3$ and $PbTiO_3$. An important factor determining the stability of this type of polarization is the compensation of polarization-induced charges on the boundary of the sample. Incomplete screening of surface charges results in a depolarization field that opposes the bulk polarization, thereby suppressing ferroelectricity. When the slabs have bulk-like polarizations the polarization induces 0.25 and 0.81 electron per unit-cell on the $BaTiO_3$ and $PbTiO_3$ surfaces, respectively. The electric charges accumulated at the interface $0.25e$ and $0.81e$ per unit-cell correspond to the calculated bulk spontaneous polarization by using a Berry phase approach, $4.64 \times 10^{-3}\ e/\mathrm{bohr}^2$ and $15.35 \times 10^{-3}\ e/\mathrm{bohr}^2$ for $BaTiO_3$ and $PbTiO_3$, respectively. We used an external electric field or defects on the surfaces for screening the polarization-induced charges in $BaTiO_3$ and $PbTiO_3$.

We stabilized out-of-plane polarization in $BaTiO_3$ by applying an external field of 0.055 atomic units. For the stabilization with defects, we used a p(2×2) supercell on the surface. To compensate 0.25 electronic charges per unit-cell area in a p(2× 2) cell, $1e^-$ is needed. If each oxygen ion accepts two electrons and each barium cation

donates two electrons, on one side half an oxygen and on other the side half a barium vacancy are needed. To this end O, is replaced by F or Ba by Cs while for the half Ba vacancy, O is replaced by N or Ba by La. The polarization in the central layers for both scenarios of stabilization (external electric field or defects) is the same as for the bulk, but on the surfaces it depends on the types of defects and external electric field.

For the stabilization of a bulk-like out-of-plane polarization in $PbTiO_3$ thin films an external electric field of 1.00×10^9 V/cm is required. Since this tremendous electric field would lead to field-emission, slabs with an external field of 0.33×10^9 V/cm are considered, which corresponds roughly to 1/3 of the bulk spontaneous polarization of $PbTiO_3$. A significant surface-charge density of about 0.81 electronic charges per unit cell area is required to stabilize the bulk like out-of-plane polarization for $PbTiO_3$. This corresponds to an unfavorably high defect concentration in the surface layers, so out-of-plane polarizations for $PbTiO_3$ slabs are stabilized by 0.5 or 0.25 electronic charges per unit cell area. The stabilized ferroelectric displacements in the central layers of the thin films are nearly equal to 1/2 and 1/3 bulk ferroelectric displacements for 0.5 and 0.25 electronic charges per unit cell area, respectively. To compensate 0.50 electronic charges per unit cell area, two electrons per p(2×2) surface corresponding to one O or to one Pb vacancy are needed.

As fourth step, we studied different types of domain walls, i.e. transversal (TDW) and longitudinal (LDW) in $PbTiO_3$. We simulated [110]-oriented 180° transversal domain walls of $PbTiO_3$ by using a supercells consisting of $N \times 1 \times 1$ perovskite unit cells stacked in the [1-10] direction and containing one up and one down domain, in a region with a width of $N/2$ lattice spacing wide region. We take the domain wall to lie in the [110] plane and the polarization to point in the [001] (z) direction. Supercells with N=4 and 6 were employed. We found that the results are insensitive to the size of the supercells. The width of the domain wall is narrow, extending over an area of just one unit cell, which is in good agreement to the experiment.

We also simulated longitudinal domain walls normal to the [001] direction of $PbTiO_3$. We constructed a 60-atom supercell arranged of six c(2×2) unit cells of the bulk tetragonal $PbTiO_3$ stacked in the direction of polarization. The longitudinal domain walls are not stable in a stoichiometric material. When such domain walls with bulk polarization are formed, the electric charges accumulated at the interface (+1.65 e per unit-cell) make the domain walls metallic and unfavorable due to electrostatic energy. For a c(2×2) longitudinal domain wall, to stabilize the bulk polarization, charges of -3.3e and +3.3e on the head-to-head (HH) and tail-to-tail (TT) domain wall are needed. We stabilized a longitudinal domain wall with 3 and 2 electrons as acceptor or donor charge at the HH or TT domain wall. Our calculations indicate the longitudinal domain walls are narrow in size extending area 2 unit-cells. This result is different from the experimental observation of longitudinal domain walls, which show that the transition of polarization in longitudinal domain walls is smooth (6 unit-cells). This can be interpreted as indication that the defects are not all assembled in a single atomic layer, but rather spread over several layers. Electrostatic interactions might be the driving force for this delocalization.

In the films and supercells, we considered only the ionic part of the polarization. The electronic part of polarization can be expected to follow the ionic part and can be calculated by using a Berry phase approach, for each layer.

In summary, our calculations show a strong, but local influence of the structural imperfection on the polarization of prototypical ferroelectric materials as long as the polarization is parallel to the (extended) defect. In contrast to these transversal polarizations, in the longitudinal case (i.e. when the polarization is perpendicular to the surface or domain wall) defects are actually needed for the stabilization of the polarization and have a long-ranged influence on the structure. Conversely, strong polarization fields accompany defect structures even in non-ferroelectric materials, as found experimentally in some interface structures [125].

Bibliography

[1] J. M. Gaugain. *C. R. Acad. Sc. Paris*, 42:1264, 1856.

[2] E. Schrödinger. *Sitzungsberichte Akad. Wiss. Wien Bd.*, 121:27, 1912.

[3] Yoshihiro Ishibashi. The pedigree of ferroic domains investigations in japan. *Materials Science and Engineering B*, 120(1-3):2 – 5, 2005. The 8th International Symposium on Ferroic Domains (ISFD-8, 2004).

[4] J. Valasek. Piezo-Electric and allied phenomena in Rochelle salt. *Phys. Rev.*, 17(4):475–481, Apr 1921.

[5] P. Busch, G. und Scherrer. *Naturwiss*, 23:737, 1935.

[6] R. G. von Hippel, A. andBreckenridge, F. G. Chesley, and Laszlo Tisza. High dielectric constant ceramics. *Industrial and Engineering Chemistry*, 38:1097–1109, 1946.

[7] A. von Hippel. Ferroelectricity, domain structure, and phase transitions of barium titanate. *Rev. Mod. Phys.*, 22(3):221–237, Jul 1950.

[8] B. T. Matthias and J. P. Remeika. Dielectric properties of sodium and potassium niobates. *Phys. Rev.*, 82(5):727–729, Jun 1951.

[9] Gen Shirane. Ferroelectricity and antiferroelectricity in ceramic $PbZrO_3$ containing Ba or Sr. *Phys. Rev.*, 86(2):219–227, Apr 1952.

[10] Edwin T. Jaynes. Displacement of oxygen in $BaTiO_3$. *Phys. Rev.*, 79(6):1008–1009, Sep 1950.

[11] J. C. Slater. The Lorentz correction in Barium Titanate. *Phys. Rev.*, 78(6):748–761, Jun 1950.

[12] Hans Mueller. Properties of rochelle salt. *Phys. Rev.*, 57(9):829–839, May 1940.

[13] Hans Mueller. Properties of rochelle salt. iii. *Phys. Rev.*, 58(6):565–573, Sep 1940.

[14] Hans Mueller. Properties of rochelle salt. iv. *Phys. Rev.*, 58(9):805–811, Nov 1940.

[15] V. L. Ginzburg. *Zh. Eksp. Teor. Fiz*, 15:739, 1945.

[16] V. L. Ginzburg. *Zh. Eksp. Teor. Fiz*, 19:36–41, 1949.

[17] A. F. Devonshire. *Phil. Mag.*, 40:1040, 1949.

[18] A. F. Devonshire. *Phil. Mag.*, 42:1065, 1951.

[19] A. F. Devonshire. *Phil. Mag. Quart. Suppl*, 3:85, 1954.

[20] H. G. Baerwald. Thermodynamic theory of ferroelectric ceramics. *Phys. Rev.*, 105(2):480–486, Jan 1957.

[21] W. Cochran. *Adv. Phys.*, 9:387, 1960.

[22] James F. Scott and Carlos A. Paz de Araujo. Ferroelectric memories. *Science*, 246(4936):1400–1405, 1989.

[23] J. F. Scott. Applications of Modern Ferroelectrics. *Science*, 315(5814):954–959, 2007.

[24] K. H. Weyrich and R. Siems. *Z. Phys.*, 61:63, 1985.

[25] R.E. Cohen. *Nature*, 358:136, 1992.

[26] R. D. King-Smith and David Vanderbilt. First-principles investigation of ferroelectricity in perovskite compounds. *Phys. Rev. B*, 49(9):5828–5844, Mar 1994.

[27] Raffaele Resta. Macroscopic polarization in crystalline dielectrics: the geometric phase approach. *Rev. Mod. Phys.*, 66:899–915, Jul 1994.

[28] R. D. King-Smith and David Vanderbilt. Theory of polarization of crystalline solids. *Phys. Rev. B*, 47(3):1651–1654, Jan 1993.

[29] David Vanderbilt and R. D. King-Smith. Electric polarization as a bulk quantity and its relation to surface charge. *Phys. Rev. B*, 48(7):4442–4455, Aug 1993.

[30] J. Padilla and David Vanderbilt. Ab initio study of $BaTiO_3$ surfaces. *Phys. Rev. B*, 56(3):1625–1631, Jul 1997.

[31] Claudia Bungaro and K. M. Rabe. Coexistence of antiferrodistortive and ferroelectric distortions at the $PbTiO_3$ (001) surface. *Phys. Rev. B*, 71(3):035420, Jan 2005.

[32] M. Krčmar and C.L. Fu. Structural and electronic properties of $BaTiO_3$ slabs: Mechanism for surface conduction. *Phys. Rev. B*, 68(11):115404, Sep 2003.

[33] E. Heifets, R. I. Eglitis, E. A. Kotomin, J. Maier, and G. Borstel. Ab initio modeling of surface structure for $SrTiO_3$ perovskite crystals. *Phys. Rev. B*, 64(23):235417, Nov 2001.

[34] First-principles calculations for $SrTiO_3$(100) surface structure. *Surface Science*, 513(1):211 – 220, 2002.

[35] R. I. Eglitis and David Vanderbilt. Ab initio calculations of $BaTiO_3$ and $PbTiO_3$ (001) and (011) surface structures. *Physical Review B (Condensed Matter and Materials Physics)*, 76(15):155439, 2007.

[36] Céline Lichtensteiger, Jean-Marc Triscone, Javier Junquera, and Philippe Ghosez. Ferroelectricity and tetragonality in ultrathin $PbTiO_3$ films. *Phys. Rev. Lett.*, 94(4):047603, Feb 2005.

[37] Javier Junquera, Magali Zimmer, Pablo Ordejón, and Philippe Ghosez. First-principles calculation of the band offset at $BaO/BaTiO_3$ and $SrO/SrTiO_3$ interfaces. *Phys. Rev. B*, 67(15):155327, Apr 2003.

[38] Javier Junquera and Philippe Ghosez. Critical thickness for ferroelectricity in perovskite ultrathin films. *Nature*, 422:506, 2003.

[39] H Donnerberg and A Birkholz. Ab initio study of oxygen vacancies in $BaTiO_3$. *Journal of Physics: Condensed Matter*, 12(38):8239–8247, 2000.

[40] H., R.-A. Eichel, T. Kloss, K.-P. Dinse, So. Laubach, St. Laubach, P. C. Schmidt, K. A. Schönau, M. Knapp, and H. Ehrenberg. Iron-oxygen vacancy defect centers in $PbTiO_3$: Newman superposition model analysis and density functional calculations. *Phys. Rev. B*, 71(13):134109, Apr 2005.

[41] B. Meyer and David Vanderbilt. Ab initio study of ferroelectric domain walls in $PbTiO_3$. *Phys. Rev. B*, 65(10):104111, Mar 2002.

[42] Xifan Wu and David Vanderbilt. Theory of hypothetical ferroelectric superlattices incorporating head-to-head and tail-to-tail 180 ° domain walls. *Physical Review B (Condensed Matter and Materials Physics)*, 73(2):020103, 2006.

[43] M. Dawber, C. Lichtensteiger, M. Cantoni, M. Veithen, P. Ghosez, K. Johnston, K. M. Rabe, and J.-M. Triscone. Unusual behavior of the ferroelectric polarization in $PbTiO_3/SrTiO_3$ superlattices. *Phys. Rev. Lett.*, 95(17):177601, Oct 2005.

[44] Yong Wang, Manish K. Niranjan, S. S. Jaswal, and Evgeny Y. Tsymbal. First-principles studies of a two-dimensional electron gas at the interface in ferroelectric oxide heterostructures. *Physical Review B (Condensed Matter and Materials Physics)*, 80(16):165130, 2009.

[45] Jonathan E. Spanier, Alexie M. Kolpak, Jeffrey J. Urban, Ilya Grinberg, Lian Ouyang, Wan Soo Yun, Andrew M. Rappe, and Hongkun Park. Ferroelectric phase transition in individual single-crystalline $BaTiO_3$ nanowires. *Nano Letters*, 6(4):735–739, 2006.

[46] Ivan Naumov and Alexander M. Bratkovsky. Unusual polarization patterns in flat epitaxial ferroelectric nanoparticles. *Physical Review Letters*, 101(10):107601, 2008.

[47] Takahiro Shimada, Shogo Tomoda, and Takayuki Kitamura. Ab initio study of ferroelectricity in edged $PbTiO_3$ nanowires under axial tension. *Physical Review B (Condensed Matter and Materials Physics)*, 79(2):024102, 2009.

[48] G. Pilania, S. P. Alpay, and R. Ramprasad. Ab initio study of ferroelectricity in $BaTiO_3$ nanowires. *Physical Review B (Condensed Matter and Materials Physics)*, 80(1):014113, 2009.

[49] Chun-Lin Jia, Shao-Bo Mi, Knut Urban, Ionela Vrejoiu, Marin Alexe, and Dietrich Hesse. Atomic-scale study of electric dipoles near charged and uncharged domain walls in ferroelectric films. *Nat Mater*, 7:57–61, 2008.

[50] P. Hohenberg and W. Kohn. Inhomogeneous electron gas. *Phys. Rev.*, 136(3B):B864–B871, Nov 1964.

[51] W. Kohn and L. J. Sham. Self-consistent equations including exchange and correlation effects. *Phys. Rev.*, 140(4A):A1133–A1138, Nov 1965.

[52] R. O. Jones and O. Gunnarsson. The density functional formalism, its applications and prospects. *Rev. Mod. Phys.*, 61(3):689–746, Jul 1989.

[53] R.M. Dreizeler and E.K.U. Gross. *Density Functional Theory: An Approach to Quantum Many-Body Problem.* Springer-Verlag, Berlin, 1990.

[54] Paul W. Ayers. Density per particle as a descriptor of coulombic systems. *Proceedings of the National Academy of Sciences of the United States of America*, 97(5):1959–1964, 2000.

[55] J. C. Slater. Wave functions in a periodic potential. *Phys. Rev.*, 51(10):846–851, May 1937.

[56] T.Loucks. *Augmented Plane Wave Method.* Benjamin, New York, 1967.

[57] O. Krogh Andersen. Linear methods in band theory. *Phys. Rev. B*, 12(8):3060–3083, Oct 1975.

[58] D. Singh. *Planewaves, Pseudopotentials and the LAPW Method.* Academic Publishers, Boston/Dordecht/London, 1994.

[59] D. R. Hamann. Semiconductor charge densities with hard-core and soft-core pseudopotentials. *Phys. Rev. Lett.*, 42(10):662–665, Mar 1979.

[60] E. Wimmer, H. Krakauer, M. Weinert, and A. J. Freeman. Full-potential self-consistent linearized-augmented-plane-wave method for calculating the electronic structure of molecules and surfaces: O_2 molecule. *Phys. Rev. B*, 24(2):864–875, Jul 1981.

[61] J. Stoer. *Numerische Mathematik.* Springer-Verlag, Berlin, 1994.

[62] Wang Ning, Chen Kailai, and Wang Dingsheng. Work function of transition-metal surface with submonolayer alkali-metal coverage. *Phys. Rev. Lett.*, 56(25):2759–2762, Jun 1986.

[63] H. Krakauer, M. Posternak, and A. J. Freeman. Linearized augmented plane-wave method for the electronic band structure of thin films. *Phys. Rev. B*, 19(4):1706–1719, Feb 1979.

[64] M. Weinert. Solution of poisson's equation: Beyond ewald-type methods. *Journal of Mathematical Physics*, 22(11):2433–2439, 1981.

[65] J.D. Jackson. *Classical Electrodynamics.* Wiley and Sons , New York, 1975.

[66] H. Erschbaumer, R. Podloucky, and A. Neckel. First-principles simulation of a charged electrode: the electronic structure of a ag(001) surface under the influence of an external electrostatic field. *Surface Science*, 237(1-3):291–304, 1990.

[67] S. Heinze, X. Nie, S. Blügel, and M. Weinert. Electric-field-induced changes in scanning tunneling microscopy images of metal surfaces. *Chemical Physics Letters*, 315(3-4):167 – 172, 1999.

[68] M. Weinert, G Schneider, R. Podloucky, and J. Redinger. Flapw: applications and implementations. *Journal of Physics: Condensed Matter*, 21(8):084201 (14pp), 2009.

[69] E. Sjöstedt, L. Nordström, and D. J. Singh. An alternative way of linearizing the augmented plane-wave method. *Solid State Communications*, 114(1):15–20, 2000.

[70] S. Goedecker. Treatment of semicore states in the linearized augmented-plane-wave method and other linearized electronic-structure methods. *Phys. Rev. B*, 47(15):9881–9883, Apr 1993.

[71] Jaejun Yu, A. J. Freeman, R. Podloucky, P. Herzig, and P. Weinberger. Origin of electric-field gradients in high-temperature superconductors: $YBa_2Cu_3O_7$. *Phys. Rev. B*, 43(1):532–541, Jan 1991.

[72] S. Blügel. First principles calculations of the electronic structures of magnetic overlayers on transition metal surface. Report 2197, Forschungszentrum Jülich, July 1988.

[73] R. Pentcheva. Ab-initio rechnungen zum zusammenhang zwischen magnetismus und struktur ultradünner film. Diplomarbeit, Universität Köln, 1996.

[74] J. Padilla B. Meyer and David Vanderbilt. Theory of $PbTiO_3$, $BaTiO_3$, and $SrTiO_3$ Surfaces. *The Surface Science of Metal Oxides*, Faraday Discussions 114:395.

[75] John P. Perdew, Kieron Burke, and Matthias Ernzerhof. Generalized gradient approximation made simple. *Phys. Rev. Lett.*, 77(18):3865–3868, Oct 1996.

[76] Zhigang Wu and R. E. Cohen. More accurate generalized gradient approximation for solids. *Physical Review B (Condensed Matter and Materials Physics)*, 73(23):235116, 2006.

[77] L. Hedin and B. I. Lundqvist. Explicit local exchange-correlation potentials. *Journal of Physics C: Solid State Physics*, 4(14):2064–2083, 1971.

[78] T.Mitsui et al. *Ferroelectrics and Related Substances. Oxides*, volume 16. Springer-Verlag, Berlin, thirteenth edition, 1981.

[79] G. Shirane, R. Pepinsky, and B. C. Frazer. X-ray and neutron diffraction study of ferroelectric $PbTiO_3$. *Acta Crystallographica*, 9(2):131–140, Feb 1956.

[80] G. Trinquier and R. Hoffmann. *J. Phys. Chem.*, 88:6696, 1984.

[81] G. W. Watson and S. C. Parker. *J. Phys. Chem. B*, 103:1258, 1999.

[82] G. W. Watson, S. C. Parker, and G. Kresse. Ab initio calculation of the origin of the distortion of α-PbO. *Phys. Rev. B*, 59(13):8481–8486, Apr 1999.

[83] M. Atanasov and D. Reinen. *J. Phys. Chem. A*, 105:5450, 2001.

[84] Rainer Waser Claus M.Schneider Stefan Blügel, Thomas Brückel, editor. *Electronic Oxides - Correlation Phenomena, Exotic Phases, and Novel Functionalities; lecture manuscripts of the 41th Spring School 2010 / ed.* Forschungszentrum Jülich GmbH, 2010.

[85] J.F.Scott. *Ferroelectrics*, 183:51, 1996.

[86] Feng Tsai and J. M. Cowley. Thickness dependence of ferroelectric domains in thin crystalline films. *Applied Physics Letters*, 65(15):1906–1908, 1994.

[87] Kenji Ishikawa, Kazutoshi Yoshikawa, and Nagaya Okada. Size effect on the ferroelectric phase transition in $PbTiO_3$ ultrafine. *Phys. Rev. B*, 37(10):5852–5855, Apr 1988.

[88] Nagaya Okada Kenji Ishikawa, Takashi Nomura and Kazumasa Takada. Size effect on the phase transition in $PbTiO_3$ fine particles. *Japanese Journal of Applied Physics*, 35(Part 1, No. 9B):5196–5198, 1996.

[89] W. L. Zhong, B. Jiang, P. L. Zhang, J. M. Ma, H. M. Cheng, and Z. H. Yang. Phase transition in $PbTiO_3$ ultrafine particles of different sizes. *Journal of Physics: Condensed Matter*, 5(16):2619–2624, 1993.

[90] Th. Michael, S. Trimper, and J. M. Wesselinowa. Size effects on static and dynamic properties of ferroelectric nanoparticles. *Physical Review B (Condensed Matter and Materials Physics)*, 76(9):094107, 2007.

[91] Alexie M. Kolpak, Dongbo Li, Rui Shao, Andrew M. Rappe, and Dawn A. Bonnell. Evolution of the structure and thermodynamic stability of the $BaTiO_3$(001) surface. *Physical Review Letters*, 101(3):036102, 2008.

[92] R. I. Eglitis, S. Piskunov, E. Heifets, E. A. Kotomin, and G. Borstel. Ab initio study of the $SrTiO_3$, $BaTiO_3$ and $PbTiO_3$(0 0 1) surfaces. *Ceramics International*, 30(7):1989 – 1992, 2004. 3rd Asian Meeting on Electroceramics.

[93] Fabio Bottin and Claudine Noguera. Stability and electronic structure of the (1×1) $SrTiO_3$(110) polar. *Phys. Rev. B*, 68(3):035418, 2003.

[94] R. E. Cohen. Periodic slab lapw computations for ferroelectric batio3. *Journal of Physics and Chemistry of Solids*, 57(10):1393 – 1396, 1996. Proceeding of the 3rd Williamsburg Workshop on Fundamental Experiments on Ferroelectrics.

[95] Aravind Asthagiri, Christoph Niederberger, Andrew J. Francis, Lisa M. Porter, Paul A. Salvador, and David S. Sholl. Thin Pt films on the polar $SrTiO_3$(1 1 1) surface: an experimental and theoretical study. *Surface Science*, 537(1-3):134 – 152, 2003.

[96] Aravind Asthagiri and David S. Sholl. DFT study of Pt adsorption on low index $SrTiO_3$ surfaces: $SrTiO_3$ (1 0 0), $SrTiO_3$ (1 1 1) and $SrTiO_3$ (1 1 0). *Surface Science*, 581(1):66–87, 2005.

[97] N. Mukunoki . Y.and Nakagawa, T. Susaki, and H. Y. Hwang. Atomically flat (110) $SrTiO_3$ and heteroepitaxy. *Applied Physics Letters*, 86(17):171908, 2005.

[98] A. Munkholm, S. K. Streiffer, M. V. Ramana Murty, J. A. Eastman, Carol Thompson, O. Auciello, L. Thompson, J. F. Moore, and G. B. Stephenson. Antiferrodistortive Reconstruction of the $PbTiO_3$(001) Surface. *Phys. Rev. Lett.*, 88(1):016101, Dec 2001.

[99] S. Stemmer and M. Streiffer, S. K.and Ruhle. *Phys, Stat. sol(a)*, 47:135, 1995.

[100] I. Vrejoiu, G.Le. Rhun, D. Zakharov, N. D.and Hesse, L. Pintilie, and M. Alexe. Threading dislocations in epitaxial ferroelectric $PbZr_{0.2}Ti_{0.8}O_3$ films and their effect on polarization backswitching. *Applied Physics Letters*, 86(28):4477–4486, 2006.

[101] J. Chen, L.A. Wills, B.W. Wessels, D.L. Schulz, and T.J. Marks. *J.electron. Matter*, 22:701, 1993.

[102] Z.R. Dai, Z.L. Wang, and Jiming Zhang. Link-up of 90° domain boundaries with interface dislocations in $BaTiO_3$/$LaAlO_3$. *Applied Physics Letters*, 68(22):3093–3095, 1996.

[103] Y. Suzuki, T.and Nishi and M. Fujimoto. Analysis of misfit relaxation in heteroepitaxial batio3 thin films. *Philosophical Magazine A*, 79:2461–2483, 1999.

[104] E. A. Fitzgerald. *Mater. Sci. Rep.*, 7:871995, 1991.

[105] T. M. Shaw, S. Trolier-McKinstry, and P. C. McIntyre. The properties of ferroelectric films at small dimensions. *Annual Review of Materials Science*, 30(1):263–298, 2000.

[106] Paul Jaita, Nishimatsu Takeshi, Kawazoe Yoshiyuki, and V. Waghmare Umesh. Ferroelectric phase transitions in ultrathin films of $BaTiO_3$. *Physical Review Letters*, 99(7):077601, 2007.

[107] J. Junquera and Philippe Ghosez. Critical thickness for ferroelectricity in perovskite ultrathin films. *Nature*, 422:506, 2003.

[108] Dillon D. Fong, G. Brian Stephenson, Stephen K. Streiffer, Jeffrey A. Eastman, Orlando Auciello, Paul H. Fuoss, and Carol Thompson. Ferroelectricity in Ultrathin Perovskite Films. *Science*, 304(5677):1650–1653, 2004.

[109] R. V. Wang, D. D. Fong, F. Jiang, M. J. Highland, P. H. Fuoss, Carol Thompson, A. M. Kolpak, J. A. Eastman, S. K. Streiffer, A. M. Rappe, and G. B. Stephenson. Reversible Chemical Switching of a Ferroelectric Film. *Physical Review Letters*, 102(4):047601, 2009.

[110] D. D. Fong, A. M. Kolpak, J. A. Eastman, S. K. Streiffer, P. H. Fuoss, G. B. Stephenson, Carol Thompson, D. M. Kim, K. J. Choi, C. B. Eom, I. Grinberg, and A. M. Rappe. Stabilization of Monodomain Polarization in Ultrathin $PbTiO_3$ films. *Physical Review Letters*, f96(12):127601, 2006.

[111] B. Meyer and David Vanderbilt. Ab initio study of $BaTiO_3$ and $PbTiO_3$ surfaces in external electric fields. *Phys. Rev. B*, 63(20):205426, May 2001.

[112] F. Freimuth, Y. Mokrousov, D. Wortmann, S. Heinze, and S. Blügel. Maximally localized wannier functions within the FLAPW formalism. *Physical Review B (Condensed Matter and Materials Physics)*, 78(3):035120, 2008.

[113] A. Roelofs, N. A. Pertsev, R. Waser, F. Schlaphof, L. M. Eng, C. Ganpule, V. Nagarajan, and R. Ramesh. Depolarizing-field-mediated 180° switching in ferroelectric thin films with 90° domains. *Applied Physics Letters*, 80(8):1424–1426, 2002.

[114] Roman Gysel, Alexander K. Tagantsev, Igor Stolichnov, Nava Setter, and Michaël Pavius. Ferroelectric film switching via oblique domain growth observed by cross-sectional nanoscale imaging. *Applied Physics Letters*, 89(8):082906, 2006.

[115] C. M. Foster, G.-R. Bai, R. Csencsits, J. Vetrone, R. Jammy, L. A. Wills, E. Carr, and Jun Amano. Single-crystal Pb(Zr_xTi_{1-x})O_3thin films prepared by metal-organic chemical vapor deposition systematic compositional variation of electronic and optical properties. *Journal of Applied Physics*, 81(5):2349–2357, 1997.

[116] K. S. Lee, J. H. Choi, J. Y. Lee, and S. Baik. Domain formation in epitaxial Pb(Zr, Ti)O_3 thin films. *Journal of Applied Physics*, 90(8):4095–4102, 2001.

[117] S. Pöykkö and D.J. Chadi. Ab initio study of dipolar defects and 180° domain walls in $PbTiO_3$. *Journal of Physics and Chemistry of Solids*, 61(2):291 – 294, 2000.

[118] Lixin He and David Vanderbilt. First-principles study of oxygen-vacancy pinning of domain walls in $PbTiO_3$. *Phys. Rev. B*, 68(13):134103, Oct 2003.

[119] Pablo Aguado-Puente and Javier Junquera. Ferromagneticlike closure domains in ferroelectric ultrathin films: First-principles simulations. *Physical Review Letters*, 100(17):177601, 2008.

[120] T Shimada, K Wakahara, Y Umeno, and T Kitamura. Shell model potential for $PbTiO_3$ and its applicability to surfaces and domain walls. *Journal of Physics: Condensed Matter*, 20(32):325225, 2008.

[121] C. L. Jia, M. Lentzen, and K. Urban. Atomic-Resolution Imaging of Oxygen in Perovskite Ceramics. *Science*, 299(5608):870–873, 2003.

[122] C. L. Jia and K. Urban. Atomic-resolution measurement of oxygen concentration in oxide materials. *Science*, 303(5666):2001–2004, 2004.

[123] S. Pöykkö and D.J. Chadi. Ab initio study of 180° domain wall energy and structure in $PbTiO_3$. *Applied Physics Letters*, 75(18):2830–2832, 1999.

[124] J. Robertson and C. W. Chen. Schottky barrier heights of tantalum oxide, barium strontium titanate, lead titanate, and strontium bismuth tantalate. *Applied Physics Letters*, 74(8):1168–1170, 1999.

[125] K. Rahmanizadeh, G. Bihlmayer, and S. Blügel. Mixed interface relaxation and charge neutrality in the oxide heterostructure $DyScO_3/SrTiO_3$. *(unpublished)*.

Acknowledgments

I am thankful to Prof. Dr. Müller-Krumbhaar, who accepted me as a graduate student and supported me throughout my thesis.

I gratefully acknowledge the stimulating atmosphere of the institute “IFF-Theory I”, which is directed by Prof. Dr. Stefan Blügel, who also is my PhD father.

Prof. Dr. Uwe Klemradt is thanked for his willingness to be the second referee for this work.

The person with whom I had most contact and very intensive exchange was Dr. Gustav Bihlmayer from whom I learned about density functional theory, ferroelectrics properties, and much more. He always had an open door and an open ear for me and supported my work with interest and readiness for discussions. I was fortunate in working in this fascinating field of physics and benefiting from the intensive care which never felt like a control. I also thank for his patient correction of this thesis.

I thank the whole group of “IFF-Theory I and III” in research center Jülich for help and companionship.

I also profited from discussions about ferroelectrics with Dr. Daniel Wortmann, who was always interested in the results of my work.

I would like to thank Frank Freimuth for introducing me to the modern theory of polarization .

I would like to thank Ionut Tranca for helping me to edit my thises text.

Finally, I would like to thank my wife Dr. Fatemeh Tabatabei for supporting me and also for interesting scientific discussions about my PhD projects. Without her support and sympathy I would not have been able to successfully complete my thesis.